

**ENERGY HARVESTING FROM AN ELASTICALLY SUPPORTED
CRUCIFORM STRUCTURE**

AHMAD ADZLAN FADZLI BIN KHAIRI

UNIVERSITI TEKNOLOGI MALAYSIA

**DECLARATION OF THESIS / UNDERGRADUATE PROJECT REPORT
AND COPYRIGHT**

Author's full name : _____

Date of Birth : _____

Title : _____

Academic Session : _____

I declare that this thesis is classified as:



CONFIDENTIAL

(Contains confidential information under the Official Secret Act 1972)*



RESTRICTED

(Contains restricted information as specified by the organization where research was done)*



OPEN ACCESS

I agree that my thesis to be published as online open access (full text)

1. I acknowledged that Universiti Teknologi Malaysia reserves the right as follows:
2. The thesis is the property of Universiti Teknologi Malaysia
3. The Library of Universiti Teknologi Malaysia has the right to make copies for the purpose of research only.
4. The Library has the right to make copies of the thesis for academic exchange.

Certified by:

SIGNATURE OF STUDENT

SIGNATURE OF SUPERVISOR

MATRIC NUMBER

NAME OF SUPERVISOR

Date:

Date:

NOTES : If the thesis is CONFIDENTIAL or RESTRICTED, please attach with the letter from the organization with period and reasons for confidentiality or restriction

“I hereby declare that I have read this thesis and in my opinion this thesis is sufficient in terms of scope and quality for the award of the degree of Doctor of Philosophy in Mechanical Engineering”

Signature : _____
Name of Supervisor : Mohamed Sukri Bin Mat Ali
Date : December 22, 2020

*Replace this page with the Cooperation Declaration form, which can be obtained from SPS or your faculty. This page is **OPTIONAL** when your research is done in collaboration with other institutions that requires their consent to publish the finding in this document.*

ENERGY HARVESTING FROM AN ELASTICALLY SUPPORTED
CRUCIFORM STRUCTURE

AHMAD ADZLAN FADZLI BIN KHAIRI

A thesis submitted in fulfilment of the
requirements for the award of the degree of
Doctor of Philosophy

Malaysia-Japan International Institute of Technology
Universiti Teknologi Malaysia

DECEMBER 2020

DECLARATION

I declare that this thesis entitled "*Energy Harvesting from an Elastically Supported Cruciform Structure*" is the result of my own research except as cited in the references. The thesis has not been accepted for any degree and is not concurrently submitted in candidature of any other degree.

Signature	:	_____
Name	:	Ahmad Adzlan Fadzli Bin Khairi
Date	:	December 22, 2020

DEDICATION

My dearest wife and children. Respected supervisor and colleagues at the WEE
iKohza. This is for all of you.

ACKNOWLEDGEMENT

I would like to first express my highest sense of gratitude to my supervisor Dr. Mohamed Sukri Mat Ali. His knowledge and proficiency in computational fluid dynamics have made my entry into this field of study a little bit more bearable and has since been an excellent tool in making novel discoveries and conclusions. His open stance in receiving ideas and suggestions to strengthen the foundations of this research has been fundamental to the preservation of the originality and timeliness of this work. I have learned a lot from him about the value of logical continuity and how to achieve it throughout the course of completing this work. The relentless effort for logical continuity throughout the thesis has been, in my opinion, crucial towards a manuscript that not only is easily accessible but helps target audiences to build upon this work in the future, hence advancing the field as a whole.

As for my beloved family, especially my wife and two babies, I really cannot think of any way to repay your hardships and understanding throughout the years of my study. Even a lifetime of unconditional love and devotion towards all of you squares only but a small fraction of what you have given up making my studies a reality. To that end I can only trust the Most Merciful to fully even the debt and make all of you among those who are most beloved by the Most Gracious. I pray to the Almighty to accept the fruit of our jihad in finding knowledge and may all the trials and tribulations we have encountered together, physically, psychologically and financially, will stand witness in the hereafter that we have answered His call towards submission, and His call towards success. Aamin ya Rabbal 'alamin.

ABSTRACT

From off-grid charging of electronic devices to energising independent wireless sensor networks, the demand for stand-alone, low-power generators from renewable energy sources is becoming ever more prevalent. This study aims to address this need, by numerically investigating a cruciform energy harvester that comprises of an elastically supported circular cylinder, and a downstream strip plate at right angles in the Reynolds number range $1.1 \times 10^3 \leq \text{Re} \leq 14.6 \times 10^3$ and Scruton number 9.94. The continuity and three dimensional, unsteady Reynolds-averaged Navier-Stokes equations are solved on the numerical domain using a free and open-source C++ library called OpenFOAM. The Spalart-Allmaras turbulence model is used to provide closure to the governing equations. Previous studies on the power output from a 10 mm diameter cylinder show that meaningful power generation only begins when the reduced velocity U^* , exceeds 15 and produces a consistent output in the order of 1 mW over the whole observation window. To improve upon this, a more fundamental understanding of why this observation takes place is indispensable. This is done by investigating the temporal evolution of the lift and displacement signals using the Hilbert-Huang transform, leading to the discovery of a route through which a significant quantity of energy is lost during energy harvesting. To eliminate said route, this work examines energy harvesting of a generalised cruciform structure, with varying cruciform angles, and discovered the following. For steep-angled cruciforms ($45^\circ \leq \alpha(\circ) \leq 67.5^\circ$) this study found asymmetries in the vortical structures that prevents lock-in and thus high-amplitude vibrations from taking place. However, for shallow-angled cruciforms ($0^\circ \leq \alpha(\circ) \leq 22.5^\circ$), this work discovered a high degree of symmetry in the distribution of vortical structures, leading to the onset of meaningful power generation as early as $U^* = 9.1$ up to the upper limit of observation, with a maximum mechanical power that is one order of magnitude larger than the highest reported by similar studies in the literature. Finally, the mechanical power and efficiency of the generalised cruciform energy harvester are presented as a map in cruciform angle-reduced velocity ($\alpha(\circ) - U^*$) parameter space, thus making it possible for future engineers to tailor the design of their cruciform energy harvester to their specific power and efficiency needs.

ABSTRAK

Daripada pengecasan peranti elektronik di luar grid sehingga pentenagaan rangkaian sensor tanpa wayar, permintaan untuk sistem penjana berkuasa rendah dari sumber tenaga boleh diperbaharui adalah semakin meningkat. Kajian ini bertujuan untuk memenuhi keperluan tersebut, dengan cara menyelidik sebuah sistem pemungut tenaga jenis krusiform yang terdiri daripada sebuah silinder bulat yang disokong secara elastik, dan sekeping plat jalur yang diletakkan pada sudut tegak di hilirnya dalam julat nombor Reynolds $1.1 \times 10^3 \leq Re \leq 14.6 \times 10^3$ dan nombor Scruton 9.94. Persamaan keselanjaran dan Navier-Stokes purata Reynolds tidak stabil tiga dimensi diselesaikan dalam domain numerikal menggunakan OpenFOAM, sebuah pustaka C++ yang percuma dan bersumber terbuka. Model gelora Spalart-Allmaras digunakan untuk melengkapkan persamaan tersebut. Kajian terdahulu tentang kuasa dari silinder berdiameter 10 mm menunjukkan penjanaan kuasa yang signifikan bermula apabila halaju terturun U^* melebihi 15, seraya menghasilkan kuasa dalam julat 1 mW secara konsisten. Kefahaman yang lebih mendalam tentang pencetus respon mekanikal tersebut adalah diperlukan untuk membolehkan penambahbaikan terhadap keputusan ini. Ini dilakukan dengan mengkaji evolusi temporal bagi daya angkat dan sesaran menggunakan penjelmaan Hilbert-Huang, yang membawa kepada penemuan proses yang membazirkan jumlah tenaga yang signifikan dalam aktiviti penjanaan kuasa. Bagi merencat proses tersebut, tinjauan dilakukan terhadap pemungut tenaga daripada bentuk krusiform yang lebih umum, sekaligus membawa kepada penemuan-penemuan berikut. Bagi krusiform bersudut tinggi ($45^\circ \leq \alpha(\circ) \leq 67.5$), kajian ini mendapatasi asimetri dalam struktur vorteks yang menghalang kejadian frekuensi terkunci, serta penghasilan amplitud getaran yang tinggi, daripada berlaku. Di sudut yang lain, bagi krusiform bersudut rendah ($0^\circ \leq \alpha(\circ) \leq 22.5$), kajian ini mendapatari darjah kesimetrian yang tinggi dalam taburan struktur vorteks di sekeliling krusiform tersebut, yang memberarkan pemungutan tenaga yang signifikan bermula seawal $U^* = 9.1$ sehingga batasan tertinggi pemerhatian dalam penyelidikan ini, dengan penghasilan kuasa maksimum satu peringkat magnitud lebih tinggi daripada yang tertinggi pernah dilaporkan dalam kajian yang setara. Akhir sekali, tulisan ini memetakan kuasa dan kecekapan mekanikal bagi krusiform terubahsuai tersebut dalam ruang parameter sudut krusiform-halaju terturun ($\alpha(\circ) - U^*$), sekaligus membolehkan penyesuaian rekabentuk pemungut tenaga mengikut perincian kuasa dan kecekapan yang diperlukan.

TABLE OF CONTENTS

	TITLE	PAGE
DECLARATION		ii
DEDICATION		iii
ACKNOWLEDGEMENT		iv
ABSTRACT		v
ABSTRAK		vi
TABLE OF CONTENTS		vii
LIST OF TABLES		x
LIST OF FIGURES		xi
LIST OF ABBREVIATIONS		xviii
LIST OF SYMBOLS		xix
LIST OF APPENDICES		xx
CHAPTER 1 INTRODUCTION	1	
1.1 Background	1	
1.2 Problem Statement	4	
1.3 Research Questions	4	
1.4 Thesis Objectives	5	
1.5 Significance of Study	6	
1.6 Thesis Scope	7	
1.7 Thesis Organisation	9	
CHAPTER 2 LITERATURE REVIEW	11	
2.1 Vortex Shedding from a Cylinder	11	
2.1.1 Karman Vortex Shedding	12	
2.1.2 Streamwise Vortex-induced Vibration	13	
2.2 Energy Harvesting from a Vibrating Cylinder	16	
2.2.1 Two-dimensionally Reducible Harvester	16	
2.2.2 Three-dimensional Irreducible Harvester	16	

CHAPTER 3	METHODOLOGY	19
3.1	Problem geometry	19
3.2	Numerical method	20
3.3	Dynamic mesh motion	23
3.4	Open flow channel experiment	24
CHAPTER 4	NUMERICAL SETUP VALIDATION	28
4.1	Richardson extrapolation and the grid convergence index (GCI)	28
CHAPTER 5	STREAMWISE VORTEX-DRIVEN VIBRATION	33
5.1	The amplitude and frequency response	33
5.2	Main vibration-driving vortical structure	36
5.3	Phase lag between Cl and normalised cylinder displacement	39
CHAPTER 6	TEMPORAL EVOLUTION OF THE LIFT COEFFICIENT	41
6.1	Ensemble empirical mode decomposition and Hilbert transform	41
6.2	The KVIV regime (reduced velocity below 13.6)	43
6.3	Transition to SVIV (reduced velocity between 15.9 and 18.2)	46
6.4	The stable SVIV regime (reduced velocity greater than 20.5)	48
CHAPTER 7	ESTIMATION OF HARNESSABLE POWER FROM A PURE CRUCIFORM	51
7.1	Mathematical model for power estimation	51
7.2	Possibility for increasing fluid power	54

CHAPTER 8	TRANSITION TO KARMAN VORTEX-DRIVEN VIBRATION	57
8.1	The amplitude and frequency response	57
8.2	Main vibration-driving vortical structure	59
8.3	Phase lag between Cl and normalised cylinder displacement	60
CHAPTER 9	KARMAN VORTEX-DRIVEN VIBRATION	63
9.1	The amplitude and frequency response	63
9.2	Main vibration-driving vortical structure	65
9.3	Phase lag between Cl and normalised cylinder displacement	68
CHAPTER 10	POWER CHARACTERISTIC IN CRUCIFORM ANGLE - REDUCED VELOCITY PARAMETER SPACE	70
CHAPTER 11	CONCLUSION	74
REFERENCES		76
LIST OF PUBLICATIONS		90

LIST OF TABLES

TABLE NO.	TITLE	PAGE
Table 3.1	Empirical constants used in the Spalart-Allmaras turbulence model.	22
Table 3.2	Summary of experimental parameters in contrast to those used in the experimental work of Koide <i>et al.</i> (2013).	26
Table 4.1	Summary of grid independency study.	32

LIST OF FIGURES

FIGURE NO.	TITLE	PAGE
Figure 1.1	Number of publications with keywords ["vortex induced vibration" energy]. Retrieved from SCOPUS.	2
Figure 1.2	Apparent power P_a (W) versus reduced velocity U^* for cases of KVIV and SVIV. Adapted from Koide <i>et al.</i> (2013).	3
Figure 2.1	Schematic of the base configuration of the oscillator system used in this study, i.e. the pure cruciform. In this configuration, the axis of the cylinder and the strip plate are perpendicular to each other.	14
Figure 3.1	Figure 3.1a shows the cross-chapteral layout of the computational domain, along with key dimensions, when viewed from the side. Figure 3.1b visualises the cross-chapter of the computational domain as viewed from the top. The arbitrarily coupled mesh interface (ACMI) used to connect the domain containing the cylinder with the domain containing the strip plate is placed halfway through the gap, i.e. $0.08D$ downstream the cylinder.	20
Figure 3.2	Variation of cruciforms studied in this work. We vary the cruciform angle from the case of a pure cruciform (90°) to the case of cylinder - plate in tandem (0°), in increments of 22.5° .	21
Figure 3.3	Our experimental system used to validate our numerical study. Figure 3.3a presents a 3D schematic of the open channel test chapter with a pure cruciform oscillator setup, while Fig. 3.3b shows a magnified schematic of the damping system.	25
Figure 3.4	The side view of our test chapter. For a more valid benchmarking of our open channel flow with a similar system in Koide <i>et al.</i> (2013), we keep the water level to 100 mm.	26

Figure 3.5	The normalised cylinder displacement measured as a function of time at $U^* = 22.7$. The experiment was repeated several times to estimate the uncertainty of the measured quantities y^* and f^* .	27
Figure 4.1	Three meshes used in the grid convergence study. Figures 4.1a, 4.1b and 4.1c show the coarse, medium and fine meshes viewed perpendicular to three main viewing positions: from the inlet, the top and the front, which is looking directly at the cylinder end.	29
Figure 4.2	The convergence diagram for y_{RMS}^* . Figure 4.2a shows how y_{RMS}^* converges close to the Richardson extrapolation value while Fig. 4.2b shows how the error (difference between the value obtained from a particular mesh and the Richardson extrapolation) decreases with decreasing grid spacing.	31
Figure 4.3	The convergence diagram for f^* . Figure 4.3a shows how f^* converges close to the Richardson extrapolation value while Fig. 4.3b shows how the error (difference between the value obtained from a particular mesh and the Richardson extrapolation) decreases with decreasing grid spacing.	31
Figure 4.4	The convergence diagram for C_{RMS} . Figure 4.4a shows how C_{RMS} converges close to the Richardson extrapolation value while Fig. 4.4b shows how the error (difference between the value obtained from a particular mesh and the Richardson extrapolation) decreases with decreasing grid spacing.	31
Figure 5.1	Evolution of the normalised root-mean-square amplitude of cylinder displacement y_{RMS}^* , with respect to reduced velocity U^* , in the streamwise vortex-driven vibration regime.	33
Figure 5.2	Comparison between the evolution of y_{RMS}^* with respect to U^* of a pure cruciform system from our numerical and experimental work. The filled square represents the numerical, while the filled circle represents the experimental results.	34

Figure 5.3	Evolution of the normalised cylinder displacement frequency, f^* , with respect to reduced velocity U^* , for the pure cruciform case.	35
Figure 5.4	Evolution of the lift coefficient root-mean-square amplitude ($C_{l,RMS}$) and normalised frequency of lift coefficient (f_{Cl}^*), with respect to reduced velocity U^* , for the pure cruciform case. The dashed line in Fig. 5.4b visualises the shedding frequency of Karman vortex computed from Eq. 5.1.	37
Figure 5.5	Distribution of normalised frequency of vortex shedding, along the span of the cylinder of the pure cruciform at $U^* = 22.7$.	37
Figure 5.6	Dominant vortical structures at $U^* = 22.7$ observed in the pure cruciform case. The vorticity slices shown are the x and y -component vorticities at $x/D = 1.96D$ (1D downstream the trailing edge of strip plate) plane, viewed orthogonal to that plane from downstream. The vorticities have a unit of s^{-1} .	39
Figure 5.7	Phase lag θ_{y-Cl} ($^\circ$) between Cl and y^* when 90° .	40
Figure 6.1	Temporal analysis of the lift coefficient and normalised cylinder displacement signal at $U^* = 4.5$. We show C_{Cl,y^*} and C_{Cl,y^*} side by side in Fig. 6.1a, present the temporal evolution of the phase lag ϕ in Fig. 6.1b and show the temporal evolution of the instantaneous frequency of the lift coefficient signal in Fig. 6.1c.	43
Figure 6.2	Temporal analysis of the lift coefficient and normalised cylinder displacement signal at $U^* = 6.8$. We show C_{Cl,y^*} and C_{y^*,y^*} side by side in Fig. 6.2a, present the temporal evolution of the phase lag ϕ in Fig. 6.2b and show the temporal evolution of the instantaneous frequency of the lift coefficient signal in Fig. 6.2c.	44

- Figure 6.3 Temporal analysis of the lift coefficient and normalised cylinder displacement signal at $U^* = 13.6$. We show C_{Cl,y^*} and C_{y^*,y^*} side by side in Fig. 6.3a, present the temporal evolution of the phase lag ϕ in Fig. 6.3b and show the temporal evolution of the instantaneous frequency of the lift coefficient signal in Fig. 6.3c. 45
- Figure 6.4 Temporal evolution of y^* and Cl at $U^* = 15.9$. Figure 6.4b shows an enlarged view of Fig. 6.4a. We can barely spot semblance of two signals with different amplitudes superimposed in the Cl signal in Fig. 6.4b. 46
- Figure 6.5 Temporal analysis of the lift coefficient and normalised cylinder displacement signal at $U^* = 15.9$. We show C_{Cl,y^*} and C_{y^*,y^*} side by side in Fig. 6.5a, present the temporal evolution of the phase lag ϕ in Fig. 6.5b and show the temporal evolution of the instantaneous frequency of Cl in Fig. 6.5c. 47
- Figure 6.6 Temporal analysis of the lift coefficient and normalised cylinder displacement signal at $U^* = 18.2$. We show C_{Cl,y^*} and C_{y^*,y^*} side by side in Fig. 6.6a, present the temporal evolution of the phase lag ϕ in Fig. 6.6b and show the temporal evolution of the instantaneous frequency of Cl in Fig. 6.6c. 49
- Figure 6.7 The instantaneous phase lag ϕ of C_{Cl,y^*} in the range $20.5 \leq U^* \leq 29.5$. We can observe ϕ slipping through 360 deg. between $20.5 \leq U^* \leq 27.3$, before disappearing at $U^* = 29.5$; an indication of improved stability and resilience of the vortical structure driving the vibration. 50
- Figure 6.8 Vibration regimes identified during analysis of ϕ . To capture the evolution of ϕ with respect to U^* , a representative value for ϕ at each U^* must be selected. We chose to use the time-averaged ϕ , ϕ_{mean} , as the representative value. 50

Figure 7.1	Estimated root-mean-square of mechanical power $P_{\text{Mech.,RMS}}$, fluid power $P_{\text{Fluid,RMS}}$, or both, of our experimental and numerical results, compared with results of similar studies in the literature. The fluid power $P_{\text{Fluid,RMS}}$ is calculated only from the results of our numerical study as the others did not measure lift.	52
Figure 7.2	The instantaneous frequency of the lift signal between $20.5 \leq U^* \leq 29.5$. The white, solid boxes enclose the IMF component of Cl due to the shedding of the streamwise vortex, while the dashed, white boxes enclose the IMF component due to the shedding of Karman vortex. Through visual inspection, we can see how the degree of dispersion (i.e., height of the box) in the instantaneous frequency of the “Karman component” of lift is about twice that of the “streamwise component” of lift.	53
Figure 7.3	Evolution of the root-mean-square amplitude of two dominant lift components due to Karman ($C_{F_L,\text{Karman,RMS}}$) and streamwise ($C_{F_L,\text{streamwise,RMS}}$) vortices with respect to U^* . The region $18.2 \leq U^* \leq 22.7$ exhibits similar magnitude for both the Karman and streamwise components of lift. On the other hand, the magnitude of amplitude for the Karman component while the region $25.0 \leq U^* \leq 29.5$ is almost always twice that of the streamwise component.	55
Figure 8.1	Evolution of the normalised root-mean-square amplitude of cylinder displacement y^*_{RMS} , with respect to reduced velocity U^* , for the 67.5° and 45° cruciform.	57
Figure 8.2	Evolution of the normalised cylinder displacement frequency, f^* , with respect to reduced velocity U^* , for the 67.5° and 45° cruciforms.	58
Figure 8.3	Evolution of the normalised Cl root-mean-square amplitude, Cl_{RMS} , with respect to reduced velocity U^* , for the 67.5° and 45° cruciforms.	58

Figure 8.4	Evolution of the normalised Cl frequency, f_{Cl}^* , with respect to reduced velocity U^* , for the 67.5° and 45° cruciforms. The dashed lines outline $f_{v,\text{Karman}}$ from Eq. 5.1.	59
Figure 8.5	Distribution of normalised frequency of vortex shedding, along the span of the cylinder of the 67.5° and 45° cruciforms at $U^* = 22.7$.	61
Figure 8.6	Dominant vortical structures at $U^* = 22.7$ observed in the 67.5° and 45° cases. The vorticity slices shown are the x and y -component vorticities (s^{-1}) at the $x/D = 1.96D$ plane, viewed orthogonal to that plane from downstream.	61
Figure 8.7	Phase lag $\theta_{y-\text{Cl}}$ ($^\circ$) between Cl and y^* when 67.5° and 45° .	62
Figure 9.1	Evolution of the normalised root-mean-square amplitude of cylinder displacement y_{RMS}^* , with respect to reduced velocity U^* , for the 22.5° and 0° cruciform.	64
Figure 9.2	Evolution of the normalised cylinder displacement frequency, f^* , with respect to reduced velocity U^* , for the 22.5° and 0° cruciforms.	64
Figure 9.3	Evolution of the normalised Cl root-mean-square amplitude, Cl_{RMS} , with respect to reduced velocity U^* , for the 22.5° and 0° cruciforms.	65
Figure 9.4	Evolution of the normalised Cl frequency, f_{Cl}^* , with respect to reduced velocity U^* , for the 22.5° and 0° cruciforms. The dashed lines outline $f_{v,\text{Karman}}$ from Eq. 5.1.	65
Figure 9.5	Distribution of normalised frequency of vortex shedding, along the span of the cylinder of the 22.5° and 0° cruciforms at $U^* = 22.7$.	66
Figure 9.6	Dominant vortical structures at $U^* = 22.7$ observed in the 22.5° and 0° cases. The vorticity slices shown are the x and y -component vorticities (s^{-1}) at the $x/D = 1.96D$ plane, viewed orthogonal to that plane from downstream.	67
Figure 9.7	Phase lag $\theta_{y-\text{Cl}}$ ($^\circ$) between Cl and y^* when 22.5° and 0° .	69
Figure 10.1	Isocontours describing the map of the normalised RMS amplitude of cylinder displacement, y_{RMS}^* in the cruciform angle - reduced velocity ($\alpha-U^*$) parameter space.	71

Figure 10.2	Isocontours describing the map of the estimated mechanical power in the cruciform angle - reduced velocity ($\alpha-U^*$) parameter space.	71
Figure 10.3	Isocontours describing the map of the estimated mechanical power in the cruciform angle - reduced velocity ($\alpha-U^*$) parameter space.	73

LIST OF ABBREVIATIONS

ANN	-	Artificial Neural Network
PC	-	Personal Computer
SVM	-	Support Vector Machine
UTM	-	Universiti Teknologi Malaysia
XML	-	Extensible Markup Language

LIST OF SYMBOLS

Re	-	Reynolds number
St	-	Strouhal number
U^*	-	Reduced velocity
Cl	-	Lift coefficient

LIST OF APPENDICES

APPENDIX	TITLE	PAGE
-----------------	--------------	-------------

CHAPTER 1

INTRODUCTION

Vortex-induced vibration (VIV) is a type of vibration that grows from instabilities in fluid flows moving past a solid object, i.e. bluff body. When the flow exceeds a critical velocity, the flow develops vortices that are shed alternately downstream the bluff body. This triggers the onset of unsteady lift and drag forces that initiate and sustain its vibration (Bukka *et al.*, 2020). Numerous occurrences of VIV are readily observable in the field of engineering. In the ocean, marine currents give rise to the vibration of risers and offshore drilling platforms (Liu *et al.*, 2020; Zhang *et al.*, 2020; Meng *et al.*, 2020). Up in the sky, aeroplane wings vibrate, and high-rise buildings experience sway as strong gusts blow around the mighty structures (Arul *et al.*, 2020; Hao and Yang, 2020; Gao *et al.*, 2020). Closer to the ground, power transmission lines vibrate as the result of wind blowing over them (Wang *et al.*, 2019; Gómez-Ortega *et al.*, 2019).

The common denominator for all these examples is the potential damage to the engineering construct experiencing it. Thus, methods are devised and implemented to mitigate the effects of the vibrations by dissipating the vibrational energy or delaying/aborting its onset in the first place.

However, the past decade has seen efforts to do exactly the opposite: purposely maximising the vibration induced by the vortices, with the aim to generate electrical power. The simplicity of design and scalability attracts many to contribute to this multidisciplinary field of study, along with the prospect of successful development and subsequent commercialization of a new generation of energy harvester.

1.1 Background

The term “flow-induced vibration” refers to a wide range of phenomena: flutter (Doare and Michelin, 2011; Xia *et al.*, 2015a,b), galloping (Kluger *et al.*, 2013;



Figure 1.1: Number of publications with keywords ["vortex induced vibration" energy]. Retrieved from SCOPUS.

Barrero-Gil *et al.*, 2010; Luo *et al.*, 2003; Chen *et al.*, 2012), turbulence-induced vibration (Nakamura *et al.*, 2013), wake-induced vibration (Ogink and Metrikine, 2010; Bearman, 2011; Derakhshandeh *et al.*, 2014), and VIV of various kinds, which are the main object of study in this proposal. The study of VIV is traditionally motivated by the potential failure of engineering structures resulting from the fluid moving around them (Shiraishi *et al.*, 1988; Nakamura and Nakashima, 1986; Larsen and Halse, 1997; Khalak and Williamson, 1999). Nevertheless, technical publications since the 2000s saw a surge in contributions toward the subject from the perspective of energy harvesting. A simple search in SCOPUS shown in Fig. 1.1 reveals this trend for keywords ["vortex induced vibration" energy] for the last 4 decades.

At the cutting edge of this field of research is a group at The University of Michigan, that has already built prototypes of the energy harvester, named VIVACE. They compared the cost of power production in USD/kWh between VIVACE and a wide selection of common (pulverised coal, integrated gasification combined cycle, natural gas combined cycle, etc.) and new power generation technologies (anaerobic digester, landfill gas, solar, etc.). The result of this comparison demonstrated how VIVACE is on par in terms of power production cost with most of the technologies it was contrasted to Bernitsas *et al.* (2008).

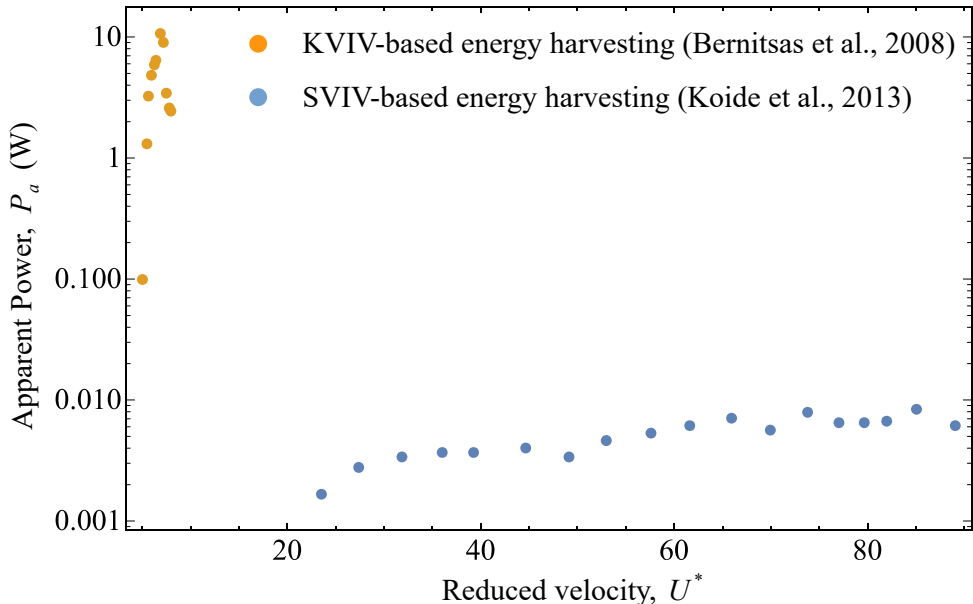


Figure 1.2: Apparent power P_a (W) versus reduced velocity U^* for cases of KVIV and SVIV. Adapted from Koide *et al.* (2013).

The VIV phenomenon utilised by the team at the University of Michigan is of the Karman VIV type (KVIV), capable of producing power in the order of MW when installed as a large-scale energy farm (Raghavan, 2007). However, as pointed out by Koide *et al.* (2013) the reduced velocity (U^*) range within which KVIV can be relied upon for power generation is about one order of magnitude smaller than what can be expected from another form of VIV namely the streamwise VIV (SVIV). Reduced velocity U^* is a nondimensional form of characteristic velocity that allows comparison of results between similar systems of differing dimensions. Since SVIV power generation is possible for a large range of U^* , it is better suited for deployment in flows with large velocity changes.

Despite this, the main shortcoming of SVIV is its maximum power output which is demonstrated at this stage of development to cap at a mW scale for a single-cylinder setup. An isolated cylinder setup for KVIV produces a maximum power in the order of 10 W (Bernitsas *et al.*, 2009). The apparent power P_a (W) for both KVIV and SVIV is shown in Koide *et al.* (2013). Following this present limitation of the unoptimized SVIV energy harvesters, their application is currently limited to mW electronics e.g., sensors and signal transmitters.

1.2 Problem Statement

The preceding section has established the viability of harnessing energy from a flow by exploiting the VIV phenomenon. Multiple modes of VIV have been observed, and SVIV stands out as better oriented for deployment in fluid flows that vary greatly in terms of free-stream velocity. Even with very rudimentary optimisations, SVIV has demonstrated its ability to generate power in the order of mW consistently over a large range of free-stream velocities. This can be harnessed to develop a self-contained power source for off-grid electronics charging, or to power independent sensor networks.

To achieve this, the problems outlined below must be addressed to close relevant gaps in the current body of knowledge.

1. A lack of understanding on the transition mechanism from Karman to streamwise vortex-induced vibration.
2. A paucity in the knowledge on what contributes to the magnitude of the alternating lift force acting on the cylinder, and its vibrational frequency components.
3. A deficiency of new methods to control the flow perturbation which gives rise to a strong, stable and periodic forcing of the cylinder vibration, sustainable over the desired operating range of U^* .

Addressing the above problems will provide a better understanding on the origins of the streamwise vortex pairs, uncover new perspectives on variables that affect the alternating lift force in the context of streamwise vortex pairs, and generate novel insight on new flow regimes, which can enlighten us to a better configuration of the energy harvester, i.e. producing more power than ever before.

1.3 Research Questions

The answer to several questions is sought in this proposed study. These questions are meant to drive the study towards its objectives.

1. How does the lift signal evolve as the flow transitions from being driven primarily by Karman vortex to streamwise vortex?

2. How does the ratio of energy transferred from the flow to the lift components evolve with respect to U^* ?
3. What deviations do the modified cruciform configuration impose on the vortical structure, against the vortical structure observed around a pure cruciform?
4. How do the deviations mentioned in 3 affect the lift magnitude, and by extension the frequency-amplitude response?
5. Where in the power envelope can we obtain maximum (minimum) power with the largest (narrowest) operability range, and how does this translate into a new mode of flow control to suit the operating conditions of the cruciform energy harvester?

1.4 Thesis Objectives

Following the problems outlined in the previous section, the objectives that define the scope of work in this proposal are listed below.

1. To investigate what takes place when the dominant vortical structure forcing the vibration changes from Karman to streamwise vortex-induced vibration (SVIV) in terms of lift and vibration signals.
2. To characterise the lift signal in terms of its components and how the components interact to modify the frequency-amplitude response of the cylinder.
3. To propose a new passive control method for an SVIV-oriented energy harvester that modifies the vortical structures and their distribution around the oscillator to control its region of operability.

The aim of objective item 1 is to get a better understanding of how the advent of streamwise vortical structures perturb the lift acting on the cylinder, which directly modifies the vibration signal of the cylinder. Objective 2 is an attempt to identify the footprint of dominant vortical structures in the flow in the lift signal and relate those to the resulting vibration signal. Finally, objective 3 seeks to recommend and evaluate a modified version of the cruciform structure that alters the vortical structure in the flow, thus modulating the lift signal acting on the cylinder and its frequency-amplitude response. The power envelope will give us a more generalised operability condition

for the energy harvester, and how we can vary the cruciform configuration to cater to a particular flow environment.

1.5 Significance of Study

Structural efforts to put flash floods in check are almost always very costly - RM443 million allocated in the 2020 Malaysia Budget alone (Kementerian Kewangan Malaysia, 2019). However, the rationale for structural solutions to the floods becomes increasingly suspect considering the worsening climate change in recent decades. However, the allocation for non-structural methods of reducing flood damages such as flood forecasting and warning protocols, was not highlighted in this budget, despite them being part of the 2016-2020 Civil Service ICT Strategic Plan (Unit Pemodenan Tadbiran dan Perancangan Pengurusan Malaysia, 2016) and 2016-2020 Department of Irrigation and Drainage Strategic Plan (Department of Irrigation and Drainage Malaysia, 2016). This fact, along with the decreasing effectiveness of structural efforts highlights the need to develop an inexpensive, simple, yet reliable non-structural system to tackle the flood problem.

Against this background, this study is able contribute significantly towards the development of an in-situ device to power water level and flow velocity/discharge sensors for a given river/drainage system using vibration energy harnessed from the flow itself. The minimalist and self-powered feature of the device allows installation of as many of the devices as necessary along the river/drainage system for adequate monitoring.

Off-grid charging of electronics is also another area to which the results of this study is able to improve. Both civilian and military activities in remote areas can benefit from the power generated to charge essential electronic devices necessary for a successful operation in said area. Improvement in terms of power output means that usage of more complex and resource intensive electronic equipments will gradually be possible in off-grid locations. This gives the deployed personnel an added advantage over their peers in performing his or her civilian or military duties in such locations.

The most significant contribution is however, to facilitate the widespread adoption of independent, wireless sensor networks. Sensor networks have wide-ranging applications in the field of monitoring; from wildlife (Gazis and Katsiri, 2020; Pathak, 2020) to forests (Kadir *et al.*, 2019; Zellweger *et al.*, 2019) to civil structures (Ni *et al.*, 2020; Sadeghi Eshkevari *et al.*, 2020; Mao *et al.*, 2020), these networks are low-power by design and is expected to operate around the clock. To increase the coverage and resolution of the monitoring task, the obvious solution is to increase the overall quantity and concentration of sensors in a particular area of interest. Nevertheless, the impracticality of connecting such a network to the national grid thrusts them in a unique position to benefit from VIV-based energy harvesters that this study seeks to improve upon.

1.6 Thesis Scope

This work is mainly a computational fluid dynamics (CFD) study of a particular version of VIV-based energy harvester that comprise of an elastically supported, horizontally constrained smooth circular cylinder of diameter 1 cm and a passive flow control mechanism that is a strip of rectangular plate at a right angle downstream the cylinder, forming a cruciform. The range of Reynolds number investigated in this thesis is between $1.1 \times 10^3 \leq Re \leq 14.6 \times 10^3$ and the mass-damping parameter, expressed by the nondimensional Scruton number Sc , is 9.94. This work limits itself to examining a cruciform where the width of the strip plate is equal to the diameter of the cylinder D , and the primary data collected from the simulation runs are the time evolution of the cylinder displacement and the corresponding lift coefficient C_l .

The baseline numerical results, i.e. results from a pure cruciform (a cruciform where the cylinder and strip plate are 90° to each other) are validated against experimental results of a similar system in a custom-made recirculating open flow channel. Although analogous systems have been studied experimentally in the past (Koide *et al.*, 2017; Zhao and Lu, 2018), in the author's opinion it is best to test the extent of reproducibility of the results in these studies first before attempting any sort of comparison with the numerical results of this work. Furthermore, having a system similar to the numerical model studied in this thesis physically available allows for

rapid consistency checks to be made between the two, thus increasing the credibility of the results.

The first part of this study looks to elucidate the relationship between the vortical structures present in the flow, especially when the ambient fluid power is high (high flow velocity region), and how they modulate the resulting lift acting on the cylinder. This is done by conducting a time-series analysis of both cylinder displacement and lift coefficient signals using the Hilbert-Huang transform (HHT). The motivation behind this is to understand why the amplitude of cylinder displacement is limited to the order of magnitude observed not only by the author, but also in numerous studies within the last ten years. This part of the study concludes with the discovery of a particular route through which a significant amount of energy from the freestream is lost during the energy harvesting process, and the amount by which the power output can be improved if this loss is eliminated.

The second part of this thesis is the author's attempt to eliminate the loss mentioned previously. This is done by generalising the cruciform system, through the variation of the relative angle between the cylinder and the strip plate. The study then proceeds to investigate the generalised cruciform system by examining the vortical structures present in the flow, how they affect the resulting lift acting on the cylinder, the amplitude of cylinder displacement itself, and ultimately the power output. The dynamics between the lift and cylinder displacement are explained through the computation of instantaneous phase lag between the two, which in turn is made possible by HHT.

The thesis concludes with the unveiling of a mechanical power and efficiency map, within a parameter space consisting of the cruciform angle and flow velocity. Useful recommendations can be deduced from the map, which highlights regions of high and low power output, and also regions of high and low efficiency, in order to obtain the desired power output and efficiency for any given power consumption requirement.

1.7 Thesis Organisation

This thesis is organised into eight chapters. The author introduces the study and gives a general overview of the research in Chapter 1. In Chapter 1, gaps in the research are identified and thesis objectives are formulated based on those gaps. Chapter 1 also outlines the questions the author seeks to address, details the scope of this study and provide concrete examples as to the significance and merit of this work. Chapter 2 reviews relevant literature that gives an overview of the progress made up to the present day, on the subject of VIV energy harvesting, by exploiting an isolated circular cylinder as the oscillator. The chapter then introduces the cruciform oscillator and the studies on the vibration characteristics of a number of variations of the cruciform oscillator.

Chapter 3 discusses the methodology taken by the author to attain the objectives listed in Chapter 1. In Chapter 3, the author details the numerical model implemented in the CFD undertaking and this includes the domain size, critical dimensions of the cruciform, boundary conditions and solution method to the unsteady, three-dimensional (3D) Reynolds-averaged Navier-Stokes equation governing the flow. Apart from that, the author also discusses the turbulence modelling adhered to in the numerical studies. The author also introduces the Hilbert-Huang transform (HHT) and explains the ensemble empirical mode decomposition (EEMD) algorithm that drives the decomposition of a time series signal into a finite number of orthogonal components. Finally, the author explains the Hilbert transform and how the transform is able to compute instantaneous phase or frequencies of a decomposed component of the signal.

Chapter 4 takes into account the validation of the numerical setup in two ways: by way of a grid independency study, and by way of experimental comparison. The grid independency study utilises the Richardson extrapolation and grid convergence index (GCI) as the primary tool to ensure spatial convergence of the numerical results. In the experimental validation, this work showcases a simple contactless method of measuring the cylinder displacement using a camera and an open-source image tracking software. After the processing of the experimental data to compute the uncertainty and present them as error bars, the author concluded that the numerical results of the pure cruciform

(90° cruciform) is in fair agreement with the experimentally obtained values, providing an added layer of confidence in the numerical results.

Chapter 5 deals with the vibration characteristics of a pure cruciform. In this chapter, the author studies in detail the lift-displacement dynamics that results from the kind of vortical structures that appear in this setup. This chapter concludes with the discovery of a path to energy loss that has never been considered before in the literature and estimated the amount of improvement possible for the power output if said loss is eliminated. Chapter 6 discourses about the vortical structures and lift-displacement dynamics of a steep-angled cruciform ($45^\circ \leq \alpha(\circ) \leq 67.5^\circ$), while Chapter 7 covers the vortical structures and lift-displacement dynamics of a shallow-angled cruciform ($0^\circ \leq \alpha(\circ) \leq 22.5^\circ$). Here, the study found out that for shallow-angled cruciforms, the onset of meaningful power generation is brought down significantly to from $U^* = 18.2$ in the pure cruciform, to $U^* = 9.1$ when the cruciform angle is 0° . At $\alpha = 0^\circ$, the maximum power also improves by approximately a power of two.

Finally, in Chapter 8, the author computes the mechanical power and efficiency of each of the cruciform variants for all flow velocities studied. From it, this work is able to produce a mechanical power and efficiency map, in essentially a cruciform angle-flow velocity parameter space.

CHAPTER 2

LITERATURE REVIEW

The alternate shedding of vortices from opposing sides of a cylinder introduces an alternating lift and drag which, unless constrained, will induce the vibration of the cylinder. This vibration energy can be converted into electrical power via the piezoelectric effect or electromagnetic induction. This is the basis of vortex-induced vibration (VIV) energy harvesting, and in this chapter, the author goes through the body of work done on the subject of vortex shedding, vortex-induced vibration and finally energy harvesting from the many variants of cylindrical oscillators, to determine the limits of our current knowledge and pinpoint where this work resides within the web of research done by the community.

2.1 Vortex Shedding from a Cylinder

In this work, a cylinder is defined as an elongated three-dimensional (3D) object with a well-defined axis, and whose cross-sectional shapes are the same at any arbitrary location along the axis. Flow around a cylinder is one of the phenomenon that, although abundantly occurring in nature and in man-made settings, remains impervious to rigorous and analytical description of the phenomenon. Key to this elusiveness is the fact that for a flow pattern to manifest itself in the physical world, the solution to the governing equations of fluid mechanics must not only exist, but must also be stable to ambient random excitations for it to be sustainable. Thus far, the Navier-Stokes equation remains unsolved on the list of Millennium Problems by the Clay Mathematics Institute, prompting researchers to rely heavily on experimental and numerical techniques in the push for breakthroughs in this field of study. Vortex shedding from a cylinder is one such interest in this field - and as the reader will see in the following subsections - whose advances are greatly driven by experimental and numerical research.

2.1.1 Karman Vortex Shedding

In the study of Karman vortex shedding, seldom is the case where one does not find reference being made to a chart on lift and drag coefficients for a stationary circular cylinder between $10^0 < \text{Re} < 10^8$ in Zdravkovich (1997). The observation that both lift and drag coefficients (C_l and C_d) have their high and low regions within $10^0 < \text{Re} < 10^8$ is of extreme utility to engineers. From the preservation of risers to the improvement of power output for VIV-based energy harvesters, the chart gives a rough outline to the range of Reynolds number suitable for a particular engineering operation. That being said, the chart remains silent on why C_l and C_d evolve the way they do with respect to Re , leaving the gap to be filled by later researchers.

For example, Desai *et al.* (2020) tackled the question why is there a reduction in C_l and C_d as the cylinder goes through the upper boundary of subcritical flow ($1.49 \times 10^5 < \text{Re} < 3.55 \times 10^5$). Their study is experimental, using tools such as particle image velocimetry (PIV) for a quantitative visualisation of the two-dimensional (2D) flow field, and proper orthogonal decomposition (POD) for identification of dominant flow structures. In doing so, they have identified two modes of shedding - the antisymmetric and symmetric modes - which takes place one after another, albeit in no well-defined cycle. The antisymmetric mode corresponds to the “normal” shedding of Karman vortices while the symmetric mode a weaker form of shedding with a higher energy level in its low-frequency components. The symmetric mode gains strength with increasing Re , which entails a weaker form of shedding taking over the flow. This ultimately reduces the magnitude of C_l and C_d of the cylinder. Depending on which side of the divide one is, an engineer may opt to amplify the symmetric mode to protect the integrity of a structure, or augment the antisymmetric mode to improve the conversion efficiency of energy from the freestream into cylinder vibration. In other words, a deeper understanding into the mechanics of Karman vortex shedding invariably leads to better strategies in cylinder motion control.

Expanding on the topic of flow control, Durhasan *et al.* (2019) conducted and experimental study of the shedding process under the following setup: the circular cylinder is placed in a larger hollow cylinder with varying pore spacing - quantified by their porosity - β - and submerged in a water flow at Reynolds number $\text{Re} = 5000$.

What they found out is the stunting of the wake from the inner cylinder when $\beta \leq 0.5$, while for porosities $\beta \geq 0.6$, a reduction of 21% to 87% in drag is observed.

Instead of making an even more detailed measurement of variables surrounding a circular cylinder or bringing in new analytical techniques to tease out novel insights that can be used to modify the system to fulfil a particular need, Yokoi (2016) simply starts with a hypothesis, and the hypothesis is a splitter plate can be used to meaningfully alter the flow pattern around a circular cylinder. Since C_l and C_d are both products of a particular flow pattern around the cylinder - namely the alternating pattern of Karman vortex shedding - it follows that the ability to control the flow pattern is essentially the ability to control these variables. To be clear, the splitter plate hypothesis is not particularly new; splitter plates have been studied in the past under a similar setup (Mat Ali *et al.*, 2011; Mat Ali *et al.*, 2012), although under completely different flow conditions and cylinder geometry. In any case, Yokoi (2016) discovered a rich collection of flow patterns that one can achieve simply by varying the splitter plate length, cylinder forcing amplitude and cylinder forcing frequency. So prominent is the role played by the splitter plate, one can even achieve a symmetric shedding of Karman vortices from the top and bottom surfaces of the cylinder. However, this requires fine-tuning of the forcing amplitude and frequency, making these results inapplicable towards cylinder motions which are flow-induced.

2.1.2 Streamwise Vortex-induced Vibration

Streamwise vortex-induced vibration (SVIV) is a type of vortex-induced vibration (VIV) driven by vortical structures whose vorticity vector points in the direction of the free stream. In its early days, the cruciform oscillator is nothing but two circular cylinders perpendicular to each other, overlapping at their midpoints (Zdravkovich, 1981, 1983, 1985). The elastically supported upstream cylinder is arranged parallel to the direction of freestream, while the downstream cylinder is fixed perpendicular to the upstream cylinder. Investigators observed the upstream cylinder acquiring significant vibrations in the scale of $O(10^{-1}D)$, as the reduced velocity of the flow U^* exceeds 14. Here D denotes the diameter of the upstream cylinder and the reduced velocity is defined in Eq. 2.1 as

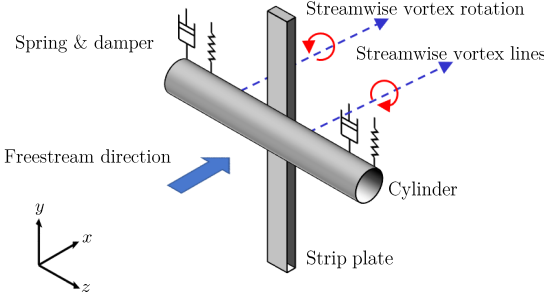


Figure 2.1: Schematic of the base configuration of the oscillator system used in this study, i.e. the pure cruciform. In this configuration, the axis of the cylinder and the strip plate are perpendicular to each other.

$$U^* = \frac{U_\infty f_n}{D}, \quad (2.1)$$

where U_∞ and f_n refers to the freestream velocity and the natural frequency of the system, respectively. More recent iterations of the system employs a thin, rectangular plate of width $w = D$ in place of the fixed downstream cylinder, and studies have shown that it retains most of the amplitude/frequency response of a two-circular cylinder cruciform.

However, at a gap g of $0.16D$, or $G = g/D = 0.16$, researchers have found that the circular cylinder-strip plate oscillator managed to sustain its vibration over a very large range of U^* . In relative terms, the vibration of this variant of the cruciform is sustained over a range of U^* 15 times the width observed in an isolated, smooth circular cylinder oscillator of similar diameter (Koide *et al.*, 2009, 2013). The reason behind this is the vortical structure driving the vibrations: vibration of the cruciform is driven by a pair of counter-rotating streamwise vortex shed a short distance from the cruciform juncture (refer Fig. 2.1), while vibration of the isolated, smooth circular cylinder is driven by Karman vortices shed alternately from the top and bottom surface of the cylinder. The upside of this discovery is the fact that this wide synchronisation range is due to vortex shedding i.e., vortex-induced vibration (VIV) instead of galloping, as in Sun *et al.* (2019), Xu *et al.* (2019) and Ding *et al.* (2019), as VIV-based energy harvesters of similar scale operate at higher efficiencies compared to galloping-based ones (Sun *et al.*, 2016; Ma *et al.*, 2016).

In their study, Deng *et al.* (2007) examined the flow field of a twin circular cylinder cruciform using computational fluid dynamics (CFD). Their domain stretches $28D$ in the streamwise direction, $16D$ in the transverse direction and $12D$ in the spanwise direction. They studied an Re range yet another order of magnitude smaller than that studied by Koide *et al.* (2017), possibly to get an even clearer visualisation of the vortical structures with less turbulence, and to ease computational requisites. At a fixed $Re = 150$, streamwise vortices form even at a gap ratio of 2. This result differs quite strikingly from Koide *et al.* (2006, 2007), conducted at an Re twice the order of magnitude of Deng *et al.* (2007), an indication that the minimum gap ratio needed for the onset of streamwise varies with respect to Re .

They also observed that when the gap ratio G , which they denote as L/D in their paper, increases from 3 to 4, the maximum amplitude of the lift coefficient increases by almost threefold. This can be attributed quite easily to the current vortex pair shed by the upstream cylinder. The downstream cylinder immediately disturbs the pair shed from the upstream cylinder when $G = 3$. The lift coefficient increases by about a factor of 3 when this immediate disturbance diminishes at $G = 4$. The visualisation of three-dimensional (3D) vorticity isocontours enables us to quickly establish this link vis-à-vis the lift coefficient signal. The authors use of CFD made this possible.

A similar study in the order of magnitude $Re \sim O(10^2)$ by Zhao and Lu (2018) particularly highlighted the immense utility of CFD as a tool to research SVIV or flow around a cruciform in general. They computed the sectional lift coefficient along the upstream cylinder, and the time history of this sectional lift coefficient revealed two different modes of vortex shedding, namely, parallel and K-shaped. They also paid attention to the local flow patterns that vary along the length of the upstream cylinder such as the trailing vortex flow, necklace vortex flow and flow in the small gap (denoted as SG flow). The discontinuities in the phase angle of the sectional lift coefficient along the upstream cylinder seems to suggest the inadequateness of attributing the lift coefficient to streamwise vortex shedding alone, particularly when Karman vortex streamlines were also observed some distance away from the junction of the cruciform. Shirakashi *et al.* (1989) also made a similar observation in their experimental work. This leads us to hypothesise that the lift signal is more appropriately viewed as the

streamwise-Karman vortex-induced composite lift signal. However, we could not find studies that took this viewpoint and worked out its implication on power generation in their investigation of SVIV.

2.2 Energy Harvesting from a Vibrating Cylinder

2.2.1 Two-dimensionally Reducible Harvester

The past two decades have witnessed an explosive growth in research concerning the field of energy harvesting from alternating lift mechanisms (Ding *et al.*, 2019; Xu *et al.*, 2017; Sun *et al.*, 2019). Contributors to this field focus mainly on the isolated circular cylinder oscillator, where previously unapplied ideas such as (1) operating the oscillator at high Reynolds number (Re) (Bernitsas *et al.*, 2008, 2009), (2) imposing high mass-damping (Lee *et al.*, 2011; Lee and Bernitsas, 2011; Sun *et al.*, 2016) and (3) calculated breaking of oscillator symmetry (Ding *et al.*, 2015a,b, 2017) lead to discoveries in the field that are directly related to improving the power output, operability range and efficiency of the energy harvester. A host techniques were introduced into the field to facilitate new understanding and uncover perspectives previously unnoticed in the study of the isolated circular cylinder oscillator. For example, two-dimensional versions of the problem were investigated using computational fluid dynamics (CFD) (Wu *et al.*, 2011; Zhang *et al.*, 2018b), implementation of virtual spring and damper in experimental works (Garcia and Bernitsas, 2018; Sun *et al.*, 2018) and reliance on machine learning methods to explore the system response within a large parameter space (Wu *et al.*, 2018; Ren *et al.*, 2019; Raissi *et al.*, 2019; Hu and Kwok, 2020) and also for active system control.

2.2.2 Three-dimensional Irreducible Harvester

In recent decades, there have been efforts to exploit the SVIV phenomenon from cruciform structures for energy harvesting, an example of which is given in Fig. 2.1. The literature on this subject can be broadly categorised into two groups: how the mechanical properties of the oscillator (e.g., mass ratio, damping, etc.) affects the amplitude/frequency response of SVIV (Koide *et al.*, 2009, 2013; Nguyen *et al.*, 2012) and how the minutiae of the flow field affect the force driving the vibration of the cylinder, i.e. the fluid mechanical aspect of the system (Deng *et al.*, 2007; Koide *et al.*, 2017; Zhao and Lu, 2018).

In the first focus area, researchers studied some permutation of the following method to convert the vibration into electrical power. The method consists of a coil and magnet. The coil, which moves with the vibrating cylinder, creates relative motion against the magnet, which is placed in the hollow of the coil (Koide *et al.*, 2009). While investigating the system at a Reynolds number in the order of $\text{Re} \sim O(10^4)$, Koide *et al.* (2009) showed that increased damping due to energy harvesting reduces the maximum vibration amplitude close to a factor of 4. Amplitude reduction due to increased total damping was also mentioned in Bernitsas *et al.* (2008); Bernitsas and Raghavan (2008); Bernitsas *et al.* (2009). Further investigation in Nguyen *et al.* (2012) revealed that damping not only affects the amplitude response of the cylinder but also narrows the synchronisation region between vortex shedding and cylinder vibration. Moreover, Nguyen *et al.* (2012) demonstrated a strong coupling between mass ratio and damping in determining both the width of the synchronisation region and the maximum amplitude response of the cylinder.

In the second focus area, investigators turned their attention to the details of the flow where streamwise vortex shedding occurs. One such study carefully shot motion pictures of the dye-injected flow (Koide *et al.*, 2017) at Reynolds number in the order of $\text{Re} \sim O(10^3)$. A lower Reynolds number (Re) reduces the amount of turbulence in the flow, allowing a clearer shot of the vortex structures. Their study also highlights the higher level of turbulence produced by the circular cylinder-strip plate cruciform in contrast to the twin circular cylinder cruciform, which diminishes the periodicity of vortex shedding. Although visually enlightening, this and other more qualitative studies contribute little towards improving our understanding of the relationship between vortex shedding and the resulting lift. Deng *et al.* (2007) demonstrated a way to overcome such a shortcoming.

Despite this discovery, there is a paucity in efforts to test new streamwise vortex-based oscillators, especially those focusing on the passive control potential of the strip plate. The past three years saw a new direction taken in the study of cruciform systems, where investigators generalised the cruciform to an upstream circular cylinder and a downstream ring plate (Hemsuwan *et al.*, 2018a,d,b,c). The result of this setup is a steady lift energy harvester that is essentially a new type of turbine. We are not aware

other attempts to generalise the cruciform structure for the purpose of improving its power output and efficiency as an alternating lift energy harvester.

CHAPTER 3

METHODOLOGY

3.1 Problem geometry

This study bases itself on the work done by Maruai *et al.* (2017), Maruai *et al.* (2018), and Koide *et al.* (2013). In these works, the investigators conducted both experimental and computational investigations of passive control of FSI of cylinders using a strip plate located at the cylinder downstream. Here, the term “strip plate” is used as a shorthand for the long, rectangular plate used to control the vibration of the cylinder – since the plate resembles a strip due to its large aspect ratio. These studies demonstrated the feasibility of energy harvesting using the oscillator system described, in the Reynolds number range $3.6 \times 10^3 < \text{Re} < 12.5 \times 10^3$. Following this observation, we performed our numerical investigations within a similar Re range, albeit slightly widened, to check for variations in the cylinder response in as wide an Re range as possible, computational resources permitting.

Our oscillator system derives its geometry from the works of Nguyen *et al.* (2012), Koide *et al.* (2013), and Koide *et al.* (2017). The basic layout of our oscillator system is the pure cruciform: an arrangement where the circular cylinder and the strip plate located downstream have their axes perpendicular to each other. We fixed the gap between the cylinder and the strip plate, G , to 0.16. This value of G was chosen because the cylinder response most suitable for energy harvesting is sustained over the largest range of reduced velocity U^* when $G = 0.16$ (Koide *et al.*, 2013).

Figure 3.1a visualises our computational domain from its side. We chose these dimensions based on analogous works such as (Maruai *et al.*, 2017) and (Maruai *et al.*, 2018) which had produced results that agree well with experiments of their own and with Kawabata *et al.* (2013). The streamwise coordinates of this domain extends from $-10.5D$ to $10.5D$, and the lateral coordinates from $-10.5D$ to $10.5D$. The coordinate origin $(0, 0, 0)$, is at the centre of the cylinder and the strip plate is $D/3$ thick.

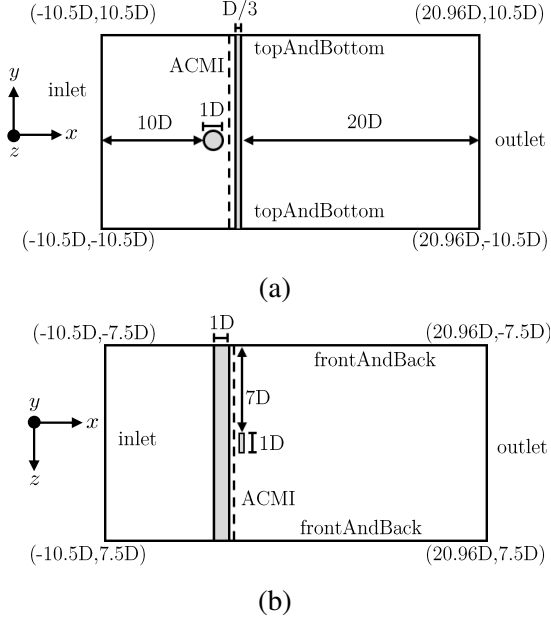


Figure 3.1: Figure 3.1a shows the cross-chapteral layout of the computational domain, along with key dimensions, when viewed from the side. Figure 3.1b visualises the cross-chapter of the computational domain as viewed from the top. The arbitrarily coupled mesh interface (ACMI) used to connect the domain containing the cylinder with the domain containing the strip plate is placed halfway through the gap, i.e. $0.08D$ downstream the cylinder.

In Fig. 3.1b, the circular cylinder extends from $z/D = 7.5$ to $z/D = -7.5$, giving the computational domain an overall spanwise length of $15D$. The computational domain of a similar study by Deng *et al.* (2007) has a length of $12D$, upon which the dimension of our domain is based upon. The extra $1.5D$ of spanwise length on either side of our domain is allocated to ensure the full expression of the three-dimensionality of flow structures that appear during the course of our numerical study.

We then produce variants of the pure cruciform configuration by rotating the strip plate from 90° to 0° in 22.5° increments. In total, we constructed five different cruciforms shown in Fig. 3.2. The dimensions of the computational domain remain fixed for all cruciforms, including the gap between the cylinder and the strip plate.

3.2 Numerical method

Our numerical study utilises OpenFOAM, an open-source computational fluid dynamics (CFD) platform written in C++. With OpenFOAM, we solved the 3D

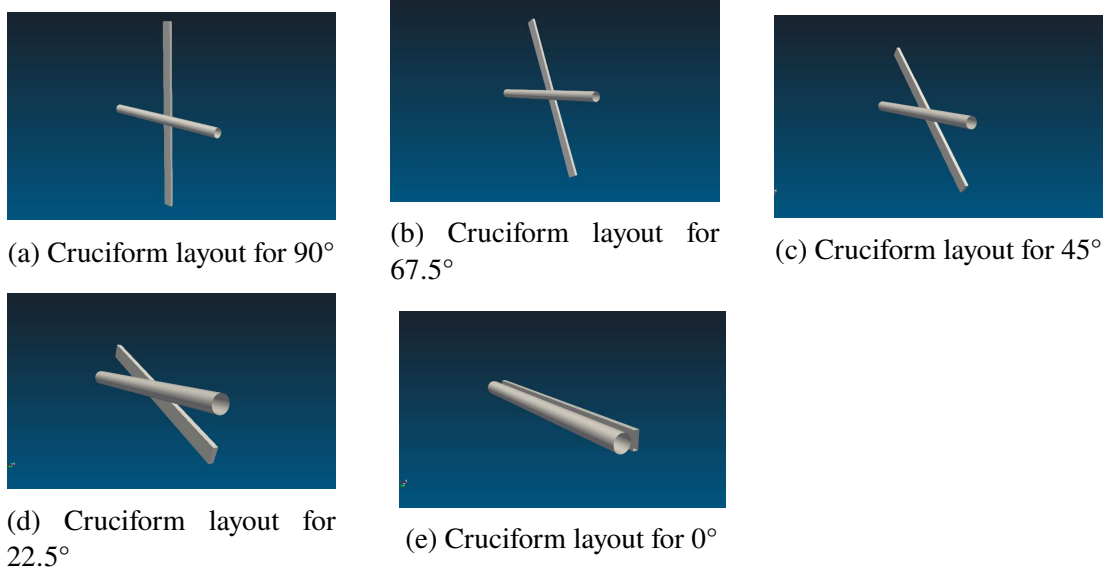


Figure 3.2: Variation of cruciforms studied in this work. We vary the cruciform angle from the case of a pure cruciform (90°) to the case of cylinder - plate in tandem (0°), in increments of 22.5° .

unsteady Reynolds averaged Navier-Stokes (3D URANS) equations that are the following.

$$\frac{\partial U_i}{\partial x_i} = 0, \quad (3.1)$$

$$\frac{\partial U_i}{\partial t} + U_j \frac{\partial U_i}{\partial x_j} = -\frac{1}{\rho} \frac{\partial P}{\partial x_i} + \frac{\partial}{\partial x_j} \left(2\nu S_{ij} - \overline{u'_j u'_i} \right). \quad (3.2)$$

The symbols U , x , t , ρ , P , ν , S , and u' denote the mean component of velocity, spatial component, time, density, pressure, kinematic viscosity, mean strain rate and the fluctuating component of velocity, respectively. Equation 3.3 gives the mean strain rate S_{ij} .

$$S_{ij} = \frac{1}{2} \left(\frac{\partial U_i}{\partial x_j} + \frac{\partial U_j}{\partial x_i} \right). \quad (3.3)$$

The turbulence model employed to approximate the Reynolds stress tensor is the Spalart-Allmaras turbulence model. Previous numerical studies on energy harvesting from FIM of circular cylinders have shown reasonable agreement with experiments in the literature through the use of this turbulence model, and thus becomes the basis for the implementation of the same turbulence model in our study (Ding *et al.*, 2015a,b). The Boussinesq approximation relates the Reynolds stress tensor $\tau_{ij} = \overline{u'_j u'^i}$ to the mean velocity gradient, exemplified by Eq. 3.4.

$$\tau_{ij} = 2\nu_T S_{ij}, \quad (3.4)$$

where ν_T represents the kinetic eddy viscosity. This kinetic eddy viscosity is ultimately expressed as a function whose arguments consist of the molecular viscosity ν , and an intermediate variable $\tilde{\nu}$ that is the solution of Eq. 3.5. Equation 3.5 incorporates empirically obtained constants to provide closure to the equations governing our numerical investigation. We list the empirical constants that make up Eq. 3.5 in Table 3.1.

$$\frac{\partial \tilde{\nu}}{\partial t} + U_j \frac{\partial \tilde{\nu}}{\partial x_j} = c_{b1} \tilde{S} \tilde{\nu} - c_{w1} f_w \left(\frac{\tilde{\nu}}{D} \right)^2 + \frac{1}{\sigma} \left\{ \frac{\partial}{\partial x_j} \left[(\nu + \tilde{\nu}) \frac{\partial \tilde{\nu}}{\partial x_j} \right] c_{b2} \frac{\partial \tilde{\nu}}{\partial x_i} \frac{\partial \tilde{\nu}}{\partial x_i} \right\} \quad (3.5)$$

Table 3.1: Empirical constants used in the Spalart-Allmaras turbulence model.

Empirical constants	Value
c_{b1}	0.01
c_{b2}	0.09
c_{w1}	0.01
κ	0.1
σ	0.162
$c_{\omega3}$	0.178

We refer the interested reader to the original paper by Spalart and Allmaras (1992) and more recent applications of the turbulence model in Ding *et al.* (2019) and Sun *et al.* (2019). With the turbulence model properly defined, we are finally able to solve Eqs. 3.1 and 3.2 using the SIMPLE-stabilised PISO algorithm native to OpenFOAM, known as the PIMPLE algorithm.

3.3 Dynamic mesh motion

Cylinder motion in the computational domain due to FIV introduces distortion to the mesh immediately surrounding the cylinder. The simplest way to keep the mesh distortion in check, thus keeping mesh quality within an acceptable level, is by diffusing the amount of warping to the surrounding space. In practice, the surrounding space is the rest of the mesh nodes, and Eq. 3.6 governs the diffusion.

$$\nabla \cdot (\gamma \nabla u) = 0. \quad (3.6)$$

In Eq. 3.6, u and γ represents the mesh deformation velocity and displacement diffusion, respectively. In this work, we set the displacement to be diffused according to the inverse quadratic rule $\gamma = 1/l^2$. Here, l denotes the distance from the cell centre to the nearest cylinder edge. Then, we solve Eq. 3.6 using the GAMG algorithm and the Gauss-Seidel smoother. Solution of Eq. 3.6 returns an updated value of u , and this updated value of u is used to update the position of the mesh nodes according to Eq. 3.7. The PIMPLE solver resumes the solution of the 3D URANS equations after we update the mesh node positions.

$$x_{\text{new}} = x_{\text{old}} + u \Delta t \quad (3.7)$$

For most numerical studies of FSI, the mesh warp diffusion method governed by Eq. 3.6 serves as an adequate workaround to conserve mesh quality. However, this requires ample number of ambient mesh nodes acting as the receiving end of the diffusion algorithm. In our case, the small gap between the cylinder and strip plate

($G = 0.16$) pose a serious limitation to our ability to diffuse the amount of warp introduced by the displacement of the cylinder, since a small space means that we can only allocate a proportionate number of mesh nodes in said gap. Sole reliance on the warp diffusion algorithm will hamper our effort to preserve mesh quality as a high concentration of warp remains within the gap. To overcome this problem, we implement the arbitrarily coupled mesh interface (ACMI) halfway through the gap (see Fig. 3.1). This technique allows adjacent cells to slide over each other precisely at the $x = 0.13$ plane, ridding us of the requirement for mesh warp diffusion. In the literature, ACMI is also known as the generalised grid interface, or GGI (Zhang *et al.*, 2018a; Sun *et al.*, 2019).

3.4 Open flow channel experiment

As part of the validation process for our numerical setup, we constructed a closed loop open flow channel, with a test chapter 100 mm wide, 200 mm high and 1500 mm long. The design of this open flow channel is heavily inspired by the water tunnel of Nguyen *et al.* (2012) and Koide *et al.* (2013). Considering the application of this research in the far future is in open flows such as natural drainage systems or the ocean - and not within pipes - prompts us to make this distinction.

We benchmark the open flow channel by setting up a pure cruciform oscillator (90°) experiment, whose data from similar studies are readily available in published works. Following this, we dimensioned the rig to follow the parameters used in Koide *et al.* (2013). A summary of our parameters and those used in Koide *et al.* (2013) are provided in Table 3.2. We tune the parameters governing the amplitude/frequency response of the oscillator using simple length-based mechanism as follows (see Fig. 3.3a). To tune the spring coefficient k , we simply adjust the active length of the twin spring plate. In practice, we obtained the calibration curve of the twin spring plate by performing a weight - displacement measurement (Sun *et al.*, 2016) at several active lengths of the plate. Once the spring coefficient versus spring plate active length calibration curve is obtained, we can just adjust the length of the spring plate to achieve the desired value of k .

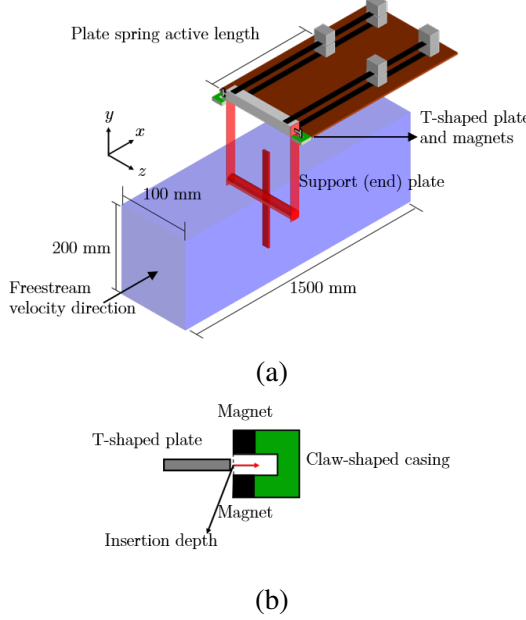


Figure 3.3: Our experimental system used to validate our numerical study. Figure 3.3a presents a 3D schematic of the open channel test chapter with a pure cruciform oscillator setup, while Fig. 3.3b shows a magnified schematic of the damping system.

Tuning the total damping of the system and consequently the multiple expressions of damping such as the logarithmic damping δ , Scruton number Sc , or the damping coefficient is done by attaching, as shown in Fig. 3.3a, a T-shaped plate made from aluminium into a claw-shaped casing that houses neodymium magnets at its ends. As presented in Fig. 3.3b, the method we use to control the strength of the magnetic field exposed to the T-shaped plate is by fixing the insertion depth of the T-shaped plate into the casing. The magnetic field serves to dissipate the kinetic energy of the T-shaped plate that moves with the cylinder during FIM, providing system damping.

A voltage controller regulates the power driving the 3.728 kW (5 hp) centrifugal pump. To set the freestream velocity in the open flow channel, we placed an acoustic Doppler velocimeter (ADV) sampling at in an empty test chapter, filled with plain tap water to a height of 100 mm, on the centreline of the channel, as pictured in Fig. 3.4. The height of 100 mm is also the water level we conduct our experiments in. We keep the water level at this height of 100 mm during all data collections to achieve a flow ambience analogous to our benchmark study of Koide *et al.* (2013), facilitating comparison between the two. Then, we sampled the velocity of the flow at different

Table 3.2: Summary of experimental parameters in contrast to those used in the experimental work of Koide *et al.* (2013).

	Current study	Koide <i>et al.</i> (2013)
Cylinder diameter, D (m)	0.01	0.01
Cylinder length, l_{cylinder} (m)	0.09	0.098
Strip-plate width (m)	0.01	0.01
Strip-plate length (m)	0.1	0.1
Effective mass, $m_{\text{eff.}}$ (kg)	0.162	0.174
Logarithmic damping, δ	0.178	0.24
Scruton number, Sc	9.94	7.74
System natural frequency, f_n (Hz)	4.42	4.4 to 4.79

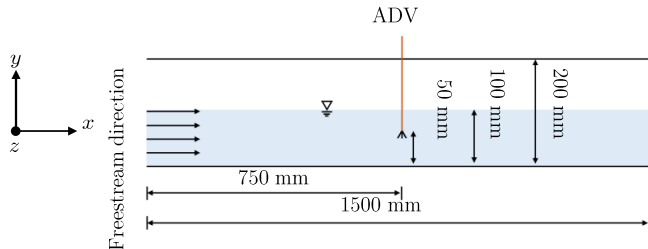


Figure 3.4: The side view of our test chapter. For a more valid benchmarking of our open channel flow with a similar system in Koide *et al.* (2013), we keep the water level to 100 mm.

input voltages by the voltage controller, the final product being an input voltage V_{in} (V) versus centreline velocity U_{cent} . calibration curve. This calibration curve allows us to set the freestream velocity of the open flow channel by specifying the input voltage to the pump. The finished product gave an operability range between 0.3 m/s and 1.1 m/s, which translates to $6.8 \leq U^* \leq 25.0$ for an circular cylinder of diameter 10 mm. The turbulence level ranges between 5% to 8% when the freestream velocity $U_{\infty} \geq 0.8$ m/s.

We measured the cylinder displacement y as a function of time by placing a visual marker on the support plate of the cylinder (see Fig. 3.3a) and capturing the motion of the marker using a video camera positioned perpendicular to the support plate. The motion of the marker is then analysed using *Tracker*: a motion analysis tool built on the Open Source Physics Java framework (for recent implementation examples, see Wen *et al.* (2020) or Krishnendu and Ramakrishnan (2020)).

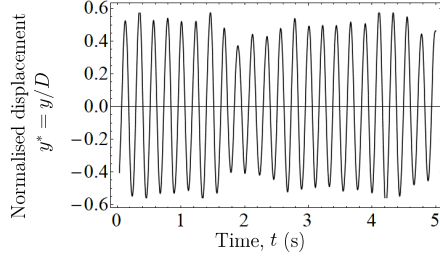


Figure 3.5: The normalised cylinder displacement measured as a function of time at $U^* = 22.7$. The experiment was repeated several times to estimate the uncertainty of the measured quantities y^* and f^* .

For the benchmarking, we chose the reduced velocity $U^* = 22.7$, as the cylinder at that U^* produces a large and stable displacement that simplifies on our part, the measurement and comparison process between our experimental system and Koide *et al.* (2013). A sample of the normalised displacement – $y^* = y/D$ – measured as a function of time is illustrated in Fig. 3.5. This time series allows us to also compute the normalised cylinder vibration frequency, $f^* = f_{\text{cyl.}}/f_n$ ($f_{\text{cyl.}}$ being the vibration frequency of the cylinder). The y^* data presented in Fig. 3.5 returns $y^* = 0.33 \pm 0.03$ and $f^* = 1.03 \pm 0.04$, after computing the uncertainty from multiple experimental runs. In their work, Koide *et al.* (2013) obtained $y^* = 0.32$ and $f^* = 1.09$ at a similar U^* – values that are well within the measurement uncertainty of our experiment. This provides a basis for our reliance on results obtained from the experimental system later in the study.

CHAPTER 4

NUMERICAL SETUP VALIDATION

4.1 Richardson extrapolation and the grid convergence index (GCI)

In this work, we establish the grid independency of the solution using the Richardson extrapolation and the grid convergence index (GCI) (Richardson and Gaunt, 1927; Stern *et al.*, 2001). The Richardson extrapolation and GCI provides us with a procedure to quantitatively measure on the degree of convergence for the quantities of interest in a numerical study. This method also forces us to pay attention to the trend of convergence of the quantities of interest, requiring a monotonic convergence before proceeding to data collection (Stern *et al.*, 2001; Mat Ali *et al.*, 2011; ?; Maruai *et al.*, 2018).

Let $f_1, f_2, f_3, \dots, f_k$ be the quantity of interest obtained from several grid resolutions. We assign a larger subscript for a coarser grid, thus ascribing f_1 to the finest and f_k to the coarsest grid. Let the difference between successive solutions be $\epsilon_{2,1}, \epsilon_{3,2}, \epsilon_{4,3}, \dots, \epsilon_{n,n-1}$, where $\epsilon_{2,1} = f_2 - f_1$, $\epsilon_{3,2} = f_3 - f_2$ and so on. Then, the GCI is defined as

$$\text{GCI}_{i+1,i} = F_s \frac{|\epsilon_{i+1,i}|}{f_i (r^p - 1)} \times 100\%, \quad (4.1)$$

where F_s , f_i and r^p denotes the safety factor ($= 1.25$), quantity of interest and the refinement ratio, r , between successive grids raised to the order of accuracy of the series of solution, p . We refer the reader to Stern *et al.* (2001); Langley Research Centre (2018) for a more detailed discussion on r^p .

We can estimate the limit of the solution as the spacing between grid points approach zero via the p^{th} method. In essence, we compute the generalised Richardson extrapolation of the quantity of interest as follows.

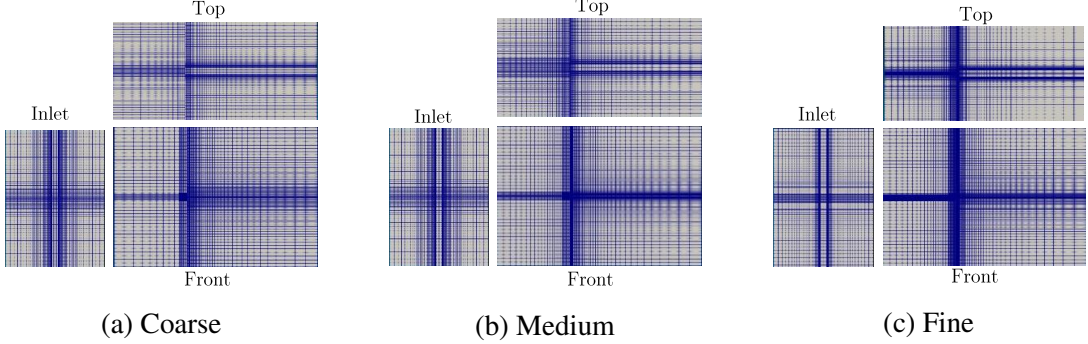


Figure 4.1: Three meshes used in the grid convergence study. Figures 4.1a, 4.1b and 4.1c show the coarse, medium and fine meshes viewed perpendicular to three main viewing positions: from the inlet, the top and the front, which is looking directly at the cylinder end.

$$f_{\text{RE}} = f_1 + \frac{f_1 - f_2}{r^p - 1}, \quad (4.2)$$

where f_{RE} is the Richardson extrapolation of the quantity of interest. Using f_{RE} to estimate the limit of the monotonically convergent series of f_i , we can determine the percentage difference of our solution on our finest grid from this limit as

$$E_i = \frac{f_i - f_{\text{RE}}}{f_{\text{RE}}} \times 100\%. \quad (4.3)$$

Table 4.1 summarises the result of our grid independency study for the SVIV reduced velocity of $U^* = 22.7$. The flow global quantities we check for convergence are the vibration amplitude, vibration frequency and lift coefficient of the cylinder. To simplify our grid independency study, we chose the pure cruciform configuration (the 90° cruciform) as the representative, and collected data at $U^* = 22.7$ on three sets of grid numbered 1 for the finest, 2 for the medium and 3 for the coarsest, shown in Fig. 4.1. With v_i as the volume of the i^{th} cell in the grid, and N the total number of cells in our domain, the average cell size becomes

$$h = \frac{1}{N} \left[\sum_{i=1}^N v_i \right]^{1/3}, \quad (4.4)$$

and the normalised average cell size is hence

$$h/D = \frac{1}{ND} \left[\sum_{i=1}^N v_i \right]^{1/3}. \quad (4.5)$$

Both y_{RMS}^* and Cl_{RMS} (see Figs. 4.2 and 4.4) have initial values smaller than their Richardson extrapolations, f_{RE} , before approaching f_{RE} , with decreasing h . The vibration frequency, on the other hand, starts at a value larger than its f_{RE} before approaching f_{RE} , as one can see in Fig. 4.3.

The most significant drop in GCI is experienced by Cl_{RMS} , with increasing refinement of the grid. Refinement from the coarse to medium grid returns a GCI of 30.92%, using a refinement ratio of 1.376. We compute the refinement ratio by dividing the number of cells in one grid with the grid one stage refined. Generalising this to i number of grids returns

$$r_{i+1,i} = \frac{S_{\text{grid},i+1}}{S_{\text{grid},i}}, \quad (4.6)$$

where $S_{\text{grid},i}$ denotes the total number of cells in the i^{th} grid. The GCI of Cl_{RMS} decreases further to 1.63% with further refinement of the grid. On the other hand, GCI for f^* , shrinks to about one-sixth of its former value.

Inspecting Figs. 4.2, 4.3 and 4.4, we find the quantities of interest to be very close to its Richardson extrapolation at the fine grid (grid 1) for all Cl_{RMS} , y_{RMS}^* and f^* . We take this as an indication of sufficient spatial discretisation. At this point, we find the trade-off between a solution even closer to the Richardson extrapolation and the increased computational effort no longer appealing, compounded by our observation that values of y_{RMS}^* and f^* at the fine grid already fall within experimental uncertainty as evidenced by our measurement in §3.4 and the work by Koide *et al.* (2013). We use the fine grid in all simulations of the pure cruciform case, and implemented a similar mesh resolution to all cruciform variants studied in this work.

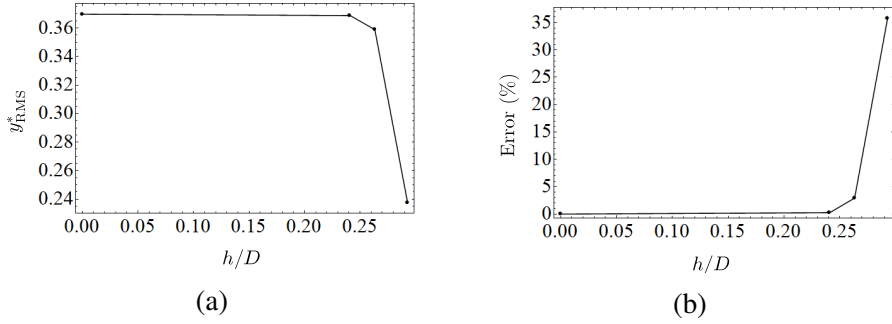


Figure 4.2: The convergence diagram for y^*_{RMS} . Figure 4.2a shows how y^*_{RMS} converges close to the Richardson extrapolation value while Fig. 4.2b shows how the error (difference between the value obtained from a particular mesh and the Richardson extrapolation) decreases with decreasing grid spacing.

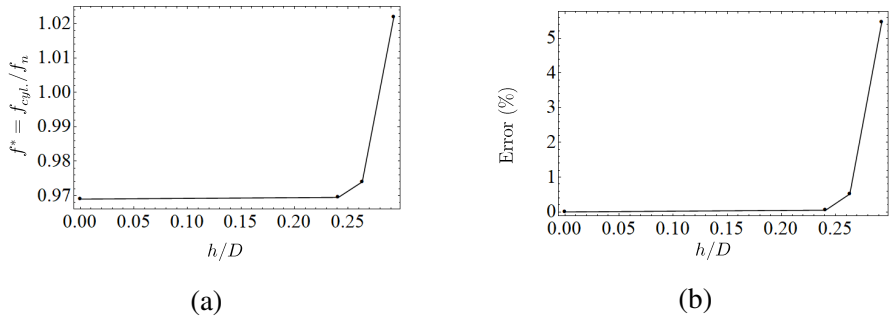


Figure 4.3: The convergence diagram for f^* . Figure 4.3a shows how f^* converges close to the Richardson extrapolation value while Fig. 4.3b shows how the error (difference between the value obtained from a particular mesh and the Richardson extrapolation) decreases with decreasing grid spacing.

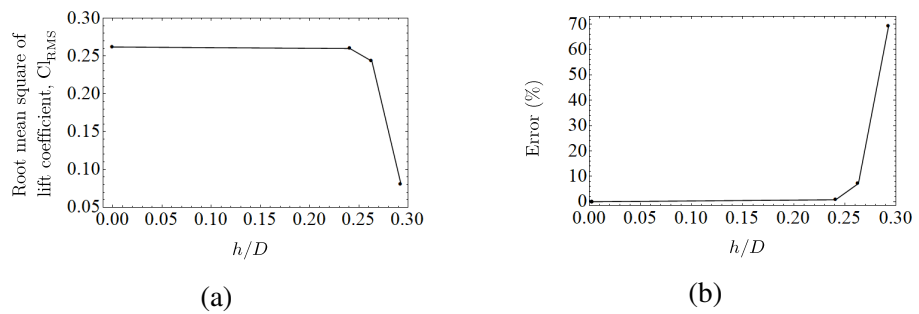


Figure 4.4: The convergence diagram for Cl_{RMS} . Figure 4.4a shows how Cl_{RMS} converges close to the Richardson extrapolation value while Fig. 4.4b shows how the error (difference between the value obtained from a particular mesh and the Richardson extrapolation) decreases with decreasing grid spacing.

Table 4.1: Summary of grid independency study.

Parameter/ metric	Cl_{RMS}	$y_{RMS}^* = y^*/D$	$f^* = f_{cyl.}/f_n$
f_{RE}	0.262	0.369	0.969
f_1	0.2598	0.3687	0.9695
f_2	0.2430	0.3588	0.9740
f_3	0.0805	0.2374	1.0220
$ \epsilon_{2,1} $	0.02	0.01	0.004
$ \epsilon_{2,1} $	0.16	0.12	0.48
$R = \epsilon_{2,1} / \epsilon_{2,1} $	0.10	0.08	0.094
$GCI_{3,2}$	30.92	6.00	0.64
$GCI_{3,2}$	1.63	0.52	0.10

CHAPTER 5

STREAMWISE VORTEX-DRIVEN VIBRATION

5.1 The amplitude and frequency response

The pure cruciform case, i.e. 90° , demonstrated a normalised root-mean-square amplitude of cylinder displacement, y_{RMS}^* that starts quite expectedly with a low amplitude at reduced velocities 2.3 and 4.5, before reaching a value close to $y_{\text{RMS}}^* = 0.1$ at $U^* = 6.8$, as presented in Fig. 5.1. Following the local maximum at $U^* = 6.8$, y_{RMS}^* tapers off to less than $y_{\text{RMS}}^* = 0.05$ between $9.1 \leq y_{\text{RMS}}^* \leq 13.6$. This whole y_{RMS}^* trend of hitting a local maximum before tapering off bears a striking resemblance to the amplitude response of an isolated circular cylinder in KVIV at mass ratios of order $O(10^1)$ (Feng, 1963; Khalak and Williamson, 1999). This resemblance can be seen as an indication that the vibration of a pure cruciform between $U^* \leq 15.9$ is driven primarily through the shedding cycle of Karman vortices.

Then at $U^* = 15.9$, y_{RMS}^* experiences a very weak increase followed by a sudden jump close to 0.4 at $U^* = 18.2$. This is followed by a slight decline at $U^* = 20.5$ and return to the previous level of y_{RMS}^* at $U^* = 22.7$. Past $U^* = 22.7$, we observe that y_{RMS}^* maintains a linear trend in its variation with respect to U^* . As $U^* = 18.2$ is well within the lower branch for a system in KVIV, it is quite unlikely for the vibration

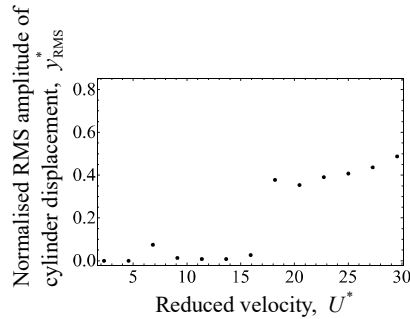


Figure 5.1: Evolution of the normalised root-mean-square amplitude of cylinder displacement y_{RMS}^* , with respect to reduced velocity U^* , in the streamwise vortex-driven vibration regime.

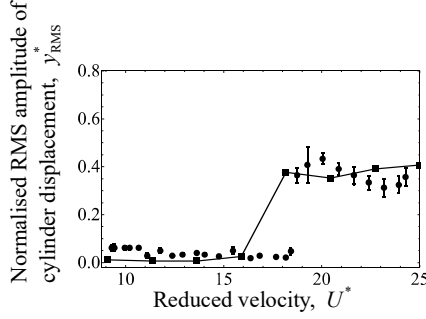


Figure 5.2: Comparison between the evolution of y_{RMS}^* with respect to U^* of a pure cruciform system from our numerical and experimental work. The filled square represents the numerical, while the filled circle represents the experimental results.

within $18.2 \leq U^* \leq 29.5$ to be governed by the shedding of Karman vortices, leading previous investigators to attribute the vibration to the periodic shedding of streamwise vortical structures dominating the spatial region close to the cruciform juncture (Shirakashi *et al.*, 1989; Hemsuwan *et al.*, 2018d,c). Hence, we name this range of U^* the streamwise vortex-induced vibration regime.

The experimental system consisting of the closed loop open flow channel and the pure cruciform oscillator rig in §3.4 is constructed not only for the purpose of validating the results of our pure cruciform numerical investigation, but also to corroborate in general, the sum total of our numerical setup. Admittedly, the best undertaking would be to perform equivalent experiment for each of the 90° , 67.5° , 45° , 22.5° and 0° configurations, but the scale of such an exercise and subsequent discussion of the results in our opinion, deserves its own treatment separate from the current study. The degree of agreement between the results of our numerical and experimental investigation of the pure cruciform establishes the validity of our numerical setup, which we assume to extend to the rest of the cruciforms. We think that this assumption is somewhat founded because all cruciforms are simulated under similar boundary conditions, mesh resolution and solver algorithm.

Our experiments collect time series data of cylinder displacement y , from which the normalised root-mean-square amplitude y_{RMS}^* is computed. Figure 5.2 compares both our numerical and experimental results of y_{RMS}^* . We observe that both results agree in terms of magnitude and trend of the amplitude response. However, the jump to SVIV occurs at a higher $U^* \approx 19$, translating to a delay of about 3 units of U^* . Our numerical

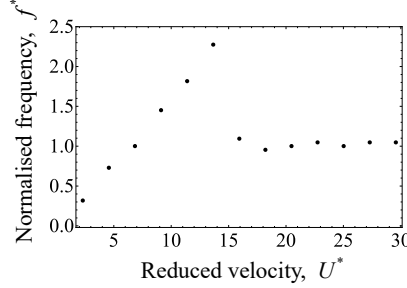


Figure 5.3: Evolution of the normalised cylinder displacement frequency, f^* , with respect to reduced velocity U^* , for the pure cruciform case.

and experimental results are also able to capture the slight dip in y_{RMS}^* following the jump to SVIV, but the occurrence in our experiment is also delayed by about 3 units of U^* . This delay can perhaps be attributed to the fact that the raw y time series were measured in succession from the lowest attainable channel flow velocity 0.3 m/s to its highest 1.1 m/s within one experimental run. In contrast, our simulations always start with the cylinder at rest at its neutral position at $t_0 = 0$ s, with the freestream exactly at set at the desired value 0.1 m/s, 0.2 m/s, . . . , 1.3 m/s. Thus, the delays found in our experimental results may simply be the consequence of “flow memory”, a concept whose analogy can be found in undergraduate experiments to determine the critical Reynolds number transitioning from laminar to turbulent flow in smooth circular pipes. The “flow memory” is in our opinion none other than the manifestation of flow inertia due to fluid viscosity, where the flow has a natural tendency to retain its previous state before being overpowered by the flow momentum. This results in the delay found at the jump to SVIV and the local y_{RMS}^* minimum after the jump.

We show the evolution of the normalised cylinder vibration frequency f^* with respect to U^* in Fig. 5.3. Inspecting Fig. 5.3, we immediately notice two distinct evolutionary pattern for f^* with a sharp boundary at $U^* = 13.6$. Between $2.3 \leq U^* \leq 13.6$, the f^* trend follows closely the shedding frequency of Karman vortices from an isolated, fixed circular cylinder (Blevins, 1990). The Karman vortex shedding frequency is given as an empirical equation in Eq. 5.1.

$$f_{v,\text{Karman}} = 0.198 \left(1 - \frac{19.7}{\text{Re}} \right) DU \quad (5.1)$$

Here, $f_{v,\text{Karman}}$, D and U are the vortex shedding frequency, diameter of the isolated circular cylinder and U the freestream velocity respectively. We can easily see how $f_{v,\text{Karman}}$ is a linear function of U , and this is what gives rise to the linear pattern of f^* within $2.3 \leq U^* \leq 13.6$. Then, within $15.9 \leq U^* \leq 29.5$, f^* drops close to 1, indicating synchronisation between lift and cylinder vibration. We think this synchronisation is what gives rise to the bigger y^* , compared to $2.3 \leq U^* \leq 13.6$.

Inspecting the evolution of root-mean-square amplitude of lift coefficient Cl_{RMS} and the normalised lift coefficient frequency f_{Cl}^* with respect to U^* in Fig. 5.4, provided more evidence supporting the assertion that $U^* = 15.9$ is a boundary between two vibration-driving mechanisms. In fact, the observation at 15.9 in Fig. 5.4a indicates that the SVIV regime is still in its infancy, due to the dip in Cl_{RMS} at that U^* , compared to $U^* = 13.6$. In Fig. 5.4b, we also draw a dashed line illustrating $f_v^* = f_{v,\text{Karman}}/D$, where $f_{v,\text{Karman}}$ is the shedding frequency of Karman vortices from a smooth isolated circular cylinder described in Eq. 5.1.

The trend found in f_{Cl}^* vs. U^* is very similar to that found in Fig. 5.3. We interpret this similarity as an indication of the symmetry of lift produced along the cylinder. Our reasoning stems from the findings of Zhao and Lu (2018), who revealed how lift is distributed along the upstream cylinder of a two-cylinder 90° cruciform. They did this by computing chapteral lift coefficients along the upstream cylinder. This system produces a symmetric distribution of chapteral lift coefficient, with $Z = 0$ being the plane of symmetry. An asymmetrical distribution of the chapteral lift coefficient may produce a trend in y_{RMS}^* and f^* that is dissimilar to those found in Cl_{RMS} and f_{Cl}^* , due to the irregular moment acting on the cylinder.

5.2 Main vibration-driving vortical structure

Recall Figs. 5.1 and 5.3. Out of all thirteen variants of U^* studied in the pure cruciform case, seven within $15.9 \leq U^* \leq 29.5$ sustain high-amplitude vibrations with no foreseeable upper limit within our observation window. For a more complete understanding of the mechanism driving the vibration, we need to know what are the vortical structures dominating the flow are and how they interact with each other.

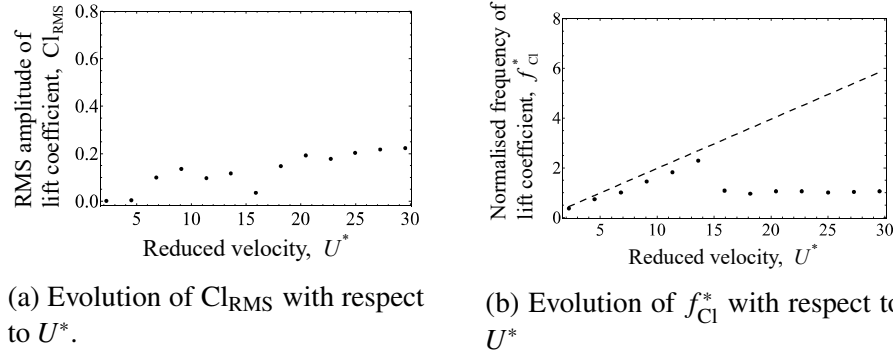


Figure 5.4: Evolution of the lift coefficient root-mean-square amplitude (Cl_{RMS}) and normalised frequency of lift coefficient (f_{Cl}^*), with respect to reduced velocity U^* , for the pure cruciform case. The dashed line in Fig. 5.4b visualises the shedding frequency of Karman vortex computed from Eq. 5.1.

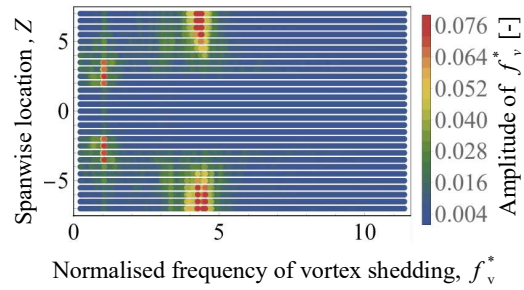


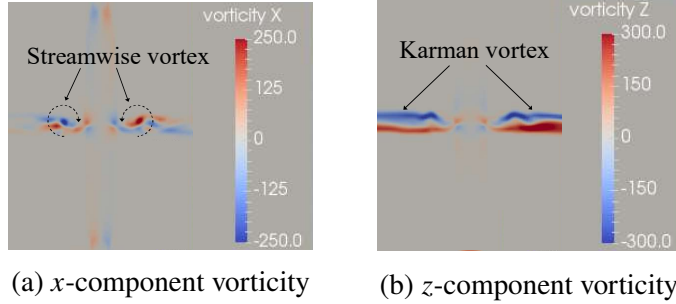
Figure 5.5: Distribution of normalised frequency of vortex shedding, along the span of the cylinder of the pure cruciform at $U^* = 22.7$.

Let us denote coordinates in our simulation domain in the following manner: $(X, Y, Z) = \left(\frac{x}{D}, \frac{y}{D}, \frac{z}{D}\right)$. We sampled the y -component velocity fluctuations on the $(X, Y) = (1.96, 0)$ line, along the span of the cylinder in $0.5D$ increments, i.e. at coordinates $(1.96, 0, 7.5), (1.96, 0, 7.0), \dots, (1.96, 0, -7.5)$. The distance $X = 1.96$ from the origin is equivalent to $1D$ downstream the trailing edge of the strip plate, and we chose this location as it is not too close to the cruciform that the vortical structures have not fully formed, and not too far, obfuscating meaningful observation of the structures.

The shedding of vortical structures leave their footprint on the flow field in the form of velocity fluctuations. Our choice of analysing the fluctuations of the y -component of velocity is made due to the fact that our oscillator is constrained to move only in the transverse direction. Then, we processed the velocity fluctuations with FFT to obtain the Fourier transform of the fluctuation signals at each spanwise location. The combined Fourier transforms are presented using a colour map in Fig. 5.5. In this figure, every point is a result of that FFT giving us a spatial understanding of the vortical structures present in the flow. The abscissa and ordinate denotes f^* and Z coordinates respectively, while the bar legend gives the amplitude of the FFT result.

Through inspection, we immediately notice two frequency bands with high amplitudes namely $f^* \approx 1$ and $f^* \approx 4.5$. The locations of these bands are between $3 \leq Z \leq 4.5$ for the former and $4.5 < Z \leq 7$ for the latter. Aided with this visualisation, we can give meaning to the x and z -components of vorticity visualised in Fig. 5.6. The slices in Fig. 5.6 visualise the distribution of the x (streamwise) and z (Karman) components of vorticity at the $X = 1.96$ plane. The plane is viewed from downstream (viewer standing at $X = 1.96$, looking towards the cruciform), and we present the vorticities in units of s^{-1} . Furthermore, the visualisations are made when the lift coefficient Cl is at a maximum (Cl_{\max}).

Comparing Fig. 5.5 with Fig. 5.6 suggests that the $f^* \approx 1$ band is actually due to the shedding of streamwise vortex of a scale close to $1D$ while the $f^* \approx 4.5$ seems to be due to the shedding of Karman vortices. Contrary to the vortical structure commonly observed in studies of isolated circular cylinders (Deng *et al.*, 2007; Kinaci *et al.*, 2016;



(a) x -component vorticity (b) z -component vorticity

Figure 5.6: Dominant vortical structures at $U^* = 22.7$ observed in the pure cruciform case. The vorticity slices shown are the x and y -component vorticities at $x/D = 1.96D$ ($1D$ downstream the trailing edge of strip plate) plane, viewed orthogonal to that plane from downstream. The vorticities have a unit of s^{-1} .

Duranay and Kinaci, 2020), in the pure cruciform case, two distinct vortical structures take shape in the flow, namely streamwise and Karman vortices. This is consistent with the findings in Koide *et al.* (2017) or Zhao and Lu (2018), where they observed a pair of streamwise vortices on a scale of $\approx 1D$ form in the vicinity of the cruciform juncture, and Karman vortices further away in the spanwise direction. Note that the vibration-driving streamwise vortices forming close to the cruciform juncture exist in pairs: in Fig. 5.6a, we observe one rotate in the clockwise direction when $Z > 0$ and the other in the counter-clockwise direction when $Z < 0$. What results from this counter-rotating vortex pair is a downward thrust, propelling the cylinder upwards, and consistent with the fact that we visualised the vorticity fields when the Cl is at a maximum. We also observe the core of both streamwise vortices lie approximately on the same Y -plane, parallel to the axis of the cylinder.

5.3 Phase lag between Cl and normalised cylinder displacement

In this study, we compute the phase lag $\theta_{y-\text{Cl}}$ by taking the Hilbert transform of both y^* and Cl signals, as Khalak and Williamson (1999) did in their VIV study of isolated circular cylinders. However, since Hilbert transform only produce physically meaningful results when used on monocomponent signals (Huang *et al.*, 1998; Huang and Attoh-Okine, 2005; Huang, 2014), the signals first needs to be decomposed into components that satisfy the aforementioned condition, referred to in the literature as the intrinsic mode function (IMF). To achieve this, we implement the ensemble empirical mode decomposition (EEMD) (Wu and Huang, 2008).

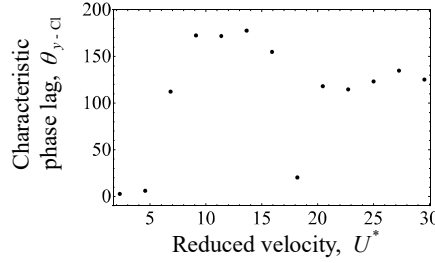


Figure 5.7: Phase lag θ_{y-Cl} ($^{\circ}$) between Cl and y^* when 90° .

$$\theta_{y-Cl} = \frac{1}{T} \int_0^T [\theta_{Cl}(t) - \theta_y(t)] dt. \quad (5.2)$$

Out of C_i IMFs for each of y^* and Cl, we select the ones for computation of instantaneous phase according to the following rule. First, we choose the IMF component of y_{RMS}^* with the largest root-mean-square amplitude to represent the original y^* signal. Then, we choose the component of Cl with the highest correlation to the IMF component of y^* , to represent the Cl signal. The degree of correlation is determined by computing the cross-correlation between the two.

The characteristic phase angle θ_{y-Cl} defined in Eq. 5.2 is what we summarise against U^* in Fig. 5.7. Note that the θ_{y-Cl} pattern between $0 \leq U^* \leq 13.6$ resembles that which is found in isolated cylinder systems undergoing KVIV. We also observe that θ_{y-Cl} starts to drop when $U^* = 15.9$, supporting the view that a fundamental change in vibration-driving mechanism took place at that U^* , culminating in the emergence of the initial branch for SVIV at $U^* = 18.2$.

CHAPTER 6

TEMPORAL EVOLUTION OF THE LIFT COEFFICIENT

6.1 Ensemble empirical mode decomposition and Hilbert transform

To obtain a clearer picture of the temporal characteristics of the lift and cylinder displacement signals, we decided to employ the ensemble empirical mode decomposition (EEMD) method (Huang *et al.*, 1998; Wu and Huang, 2008) on the signals, and compute their instantaneous phase lag, frequency and amplitude using the Hilbert transform.

The Hilbert transform (HT) has been used in the past to study the instantaneous phase and frequencies of KVIV (Khalak and Williamson, 1999). However, the signal must be monochromatic if we are to obtain a physically meaningful result after applying HT. EEMD is a way to pre-process the signal and get components that (1) have zero mean, and (2) have an equal number of extrema and zero crossings, or they differ only by one. Functions that fulfil these criteria are called intrinsic mode functions (IMF), and they guarantee a physically meaningful result to HT (Gumelar *et al.*, 2019; Zhou *et al.*, 2019). Unlike Fourier transform, which is an analytical method of signal decomposition based on circular functions in the complex plane, EEMD is algorithmic, and the processes undertaken can be summarised as follows.

Produce 150 white noise signals of length equal to the original signal and amplitude equal to 0.2 of the standard deviation of the original signal. Then, add to the set of white noises the original signal – creating 150 variations of the original signal. Following that, we apply the empirical mode decomposition (EMD) algorithm on each of the 150 signals. The EMD algorithm is summarised below.

1. Construct the envelope of the signal by connecting all maxima/minima with cubic splines.
2. Find the local mean of the envelope for the span of the data.

3. Find the difference between the local mean and the original data.
4. Repeat steps 1 and 2 on the difference in 3 for ten times (Wu and Huang, 2008).

The steps above produce a set of intrinsic mode functions or IMFs for each of the 150 variations of the original signal. Then, we average the first IMF component from each of the decomposed original signal variations, to obtain the first EEMD IMF, C_1 , of the original signal. We do the same for the second, third, until the i^{th} component for each of the 150 original signal variations, thus obtaining C_2, C_3, \dots, C_i .

To compute the phase lag between the characteristic IMFs of the lift coefficient and normalised cylinder displacement, we select the IMF components with the highest correlation to the y^* signal at that particular U^* , to represent the signals, denoted as C_{y^*,y^*} for the characteristic normalised cylinder displacement, and C_{Cl,y^*} as the characteristic lift coefficient signal. The phase lag, instantaneous frequency and instantaneous amplitude of the signal is subsequently computed by constructing an analytical signal $z(t)$ from C_1, C_2, \dots, C_i by computing the Hilbert transform of the IMF, H_i ,

$$H_i(t) = \frac{1}{\pi} \text{PV} \int_{-\infty}^{\infty} \frac{C_i(\tau)}{t - \tau} d\tau, \quad (6.1)$$

where PV denotes the Cauchy principal value, and then constructing the analytical signal as follows.

$$z(t) = C_i(t) + iH_i(t) \quad (6.2)$$

Note that i in Eq. 6.2 is the complex number.

We refer the reader interested in the details of EEMD and Hilbert transform, also collectively known as the Hilbert-Huang transform (HHT), to the following excellent texts on the subject (Huang and Attoh-Okine, 2005; Huang, 2014).

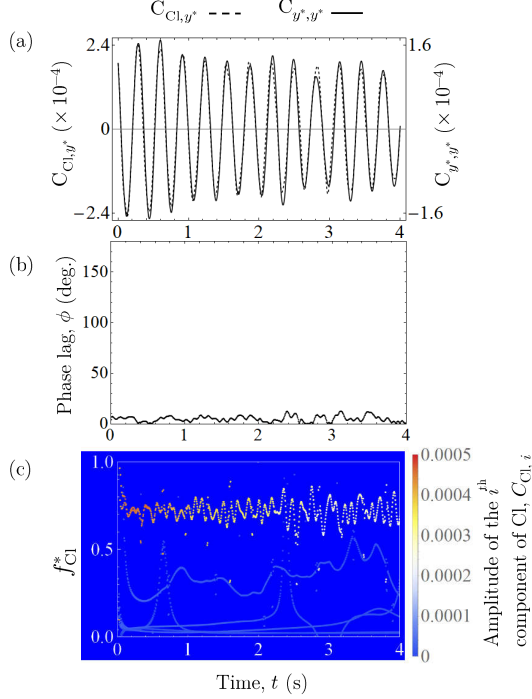


Figure 6.1: Temporal analysis of the lift coefficient and normalised cylinder displacement signal at $U^* = 4.5$. We show C_{Cl,y^*} and C_{Cl,y^*} side by side in Fig. 6.1a, present the temporal evolution of the phase lag ϕ in Fig. 6.1b and show the temporal evolution of the instantaneous frequency of the lift coefficient signal in Fig. 6.1c.

6.2 The KVIV regime (reduced velocity below 13.6)

At reduced velocities $U^* = 2.3$ and 4.5 , the phase lags ϕ (deg.) between Cl and U^* are practically zero throughout the whole observation time. The characteristic IMFs of Cl and y^* at $U^* = 4.5$ exemplifies this trend, as showcased in Fig. 6.1. Here, Fig. 6.1a shows the temporal evolution of C_{y^*,y^*} and C_{Cl,y^*} , which are the characteristic IMFs of y^* and Cl, respectively. Figure 6.1b shows the phase lag between C_{y^*,y^*} and C_{Cl,y^*} , and Fig. 6.1c presents the HHT spectrogram of Cl. The HHT spectrogram visualises the instantaneous frequency and amplitude of the IMF components of Cl. The trend that one notices in Fig. 6.1b is similar to what was observed in Khalak and Williamson (1999), a study that also employs the Hilbert transform to obtain the instantaneous phase, albeit without EEMD. The dominant IMF component (IMF component sustaining the highest amplitude throughout the whole observation time) of the lift coefficient has a normalised frequency $f_{Cl}^* = f_{Cl}/f_n$ (Fig. 6.1c) centred at approximately $f_{Cl}^* = 0.75$.

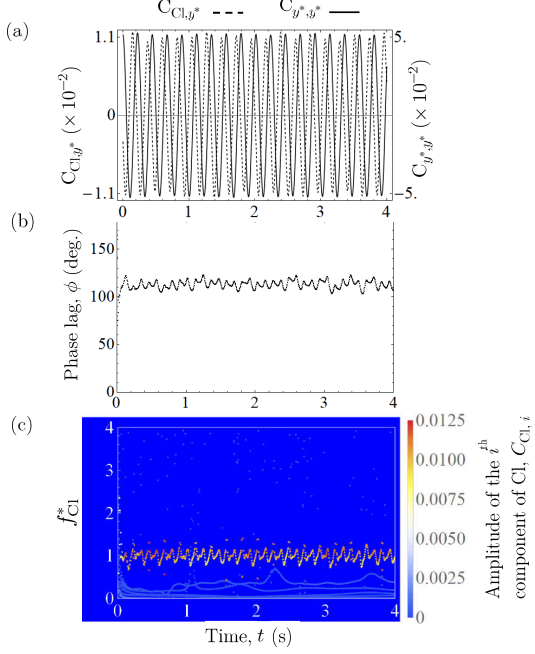


Figure 6.2: Temporal analysis of the lift coefficient and normalised cylinder displacement signal at $U^* = 6.8$. We show C_{Cl,y^*} and C_{y^*,y^*} side by side in Fig. 6.2a, present the temporal evolution of the phase lag ϕ in Fig. 6.2b and show the temporal evolution of the instantaneous frequency of the lift coefficient signal in Fig. 6.2c.

Once we enter the upper branch of KVIV at $U^* = 6.8$, ϕ jumps to approximately 110 deg. This jump in ϕ is characteristic of the transition to the upper branches as also observed by Maruai *et al.* (2018), among others. Both C_{Cl,y^*} and C_{y^*,y^*} signals are visibly very periodic, and the dominant frequency band of Cl, is centred at ≈ 1 , as one can verify in Fig. 6.2c.

As we increase U^* even further up to $U^* = 13.6$, we see a similar trend for all $U^* = 9.1, 11.4, 13.6$ examined: C_{y^*,y^*} and C_{Cl,y^*} are both qualitatively very periodic. Their phase lags are very close to 180 deg., and the dominant Cl frequency bands exhibit a time-averaged value that increases linearly with respect to U^* , in a manner that the Strouhal number of Cl is always ≈ 0.16 on average. We present the representative case of $U^* = 13.6$ in Fig. 6.3. Note how ϕ in this range of U^* varies much less with respect to time, compared to ϕ at $U^* = 6.8$, and the dominant frequency band of Cl is much narrower compared to the dominant frequency band at $U^* = 6.8$, indicating a highly periodic and self-similar oscillation of lift.

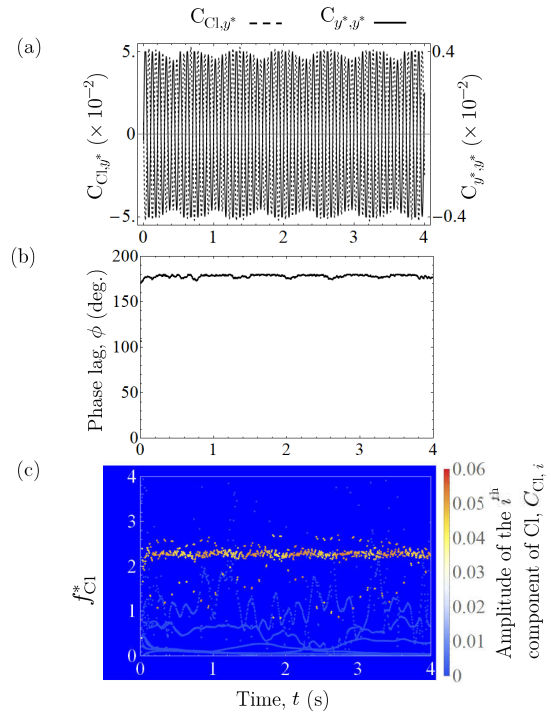


Figure 6.3: Temporal analysis of the lift coefficient and normalised cylinder displacement signal at $U^* = 13.6$. We show C_{Cl,y^*} and C_{y^*,y^*} side by side in Fig. 6.3a, present the temporal evolution of the phase lag ϕ in Fig. 6.3b and show the temporal evolution of the instantaneous frequency of the lift coefficient signal in Fig. 6.3c.

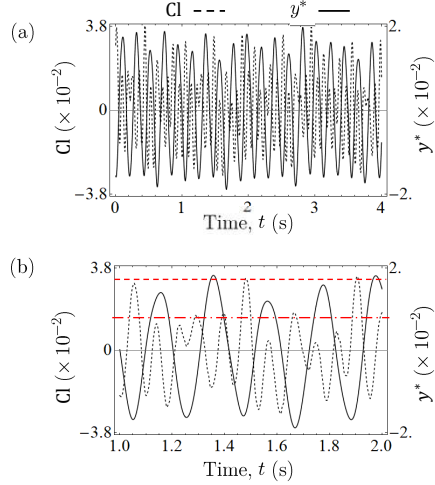


Figure 6.4: Temporal evolution of y^* and Cl at $U^* = 15.9$. Figure 6.4b shows an enlarged view of Fig. 6.4a. We can barely spot semblance of two signals with different amplitudes superimposed in the Cl signal in Fig. 6.4b.

6.3 Transition to SVIV (reduced velocity between 15.9 and 18.2)

Previously in the $U^* \leq 13.6$ range, we observed that the temporal profile of both Cl and y^* are very similar to each other, except that Cl leads y^* by a certain amount. This similarity in profile supports the assertion that the vibration within $U^* \leq 13.6$ is driven exclusively by the shedding of Karman vortices, which brings the onset of the alternating lift. Analogously, one might expect a similar profile between Cl and y^* when streamwise vortices drive the vibration. However, this does not seem to be the case.

Once we reach $U^* = 15.9$, we observe that it has become difficult to argue that the profile of y^* is just a lagged version of the profile of Cl . This is shown in Fig. 6.4a, with the enlarged version in Fig. 6.4b. The profile of Cl looks like the result of several signals in superposition, which one can almost distinguish from the presence of two types of maxima at two different amplitude heights. We put a red dashed line and a red dashed-dot line in Fig. 6.4b as visual cues indicating the two amplitude heights. Decomposing the lift coefficient signal using EEMD reveals partial evidence supporting the compound signal hypothesis.

Once we have decomposed the signal using EEMD, we replot Fig. 6.4a using C_{Cl,y^*} and C_{y^*,y^*} in Fig. 6.5a. One can clearly see that the part of Cl signal responsible for driving the vibration at $U^* = 15.9$ is embedded in the original Cl signal (Fig. 6.5a),

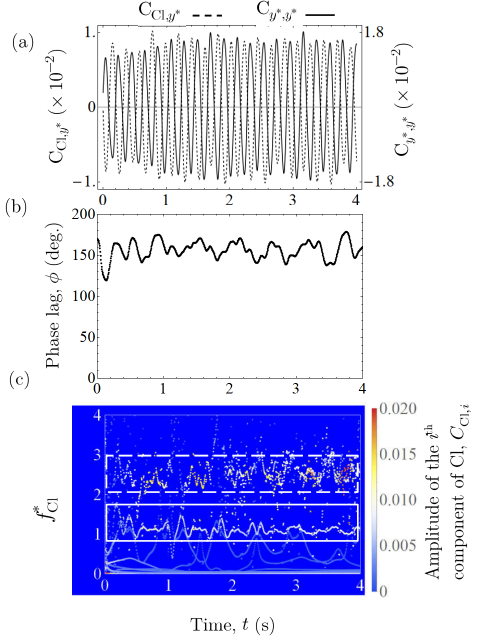


Figure 6.5: Temporal analysis of the lift coefficient and normalised cylinder displacement signal at $U^* = 15.9$. We show C_{Cl,y^*} and C_{y^*,y^*} side by side in Fig. 6.5a, present the temporal evolution of the phase lag ϕ in Fig. 6.5b and show the temporal evolution of the instantaneous frequency of Cl in Fig. 6.5c.

and decomposition via EEMD managed to recover this signal, which leads C_{y^*,y^*} by approximately 150 deg. on average, throughout the whole observation time (Fig. 6.5b). This decline from $\phi \approx 180$ deg. at reduced velocities $9.1 \leq U^* \leq 13.6$, to $\phi \approx 150$ deg. at $U^* = 15.9$ is quite sizeable, suggesting a fundamental change in flow dynamics, particularly in terms of vortical structure. Another notable change is the increased temporal variation in ϕ from its time-averaged value, in contrast to the evolution of ϕ in the range $9.1 \leq U^* \leq 13.6$, which has very little jitter throughout the observation time.

Inspecting the HHT spectrogram in Fig. 6.5c reveals two dominant bands in the frequency domain. The first one, marked with a white continuous rectangular box, is the instantaneous frequency for the IMF component of lift shown in Fig. 6.5a, and its mean frequency lies close to the natural frequency of the system ($f_{Cl}^* \approx 1$). There is; however, a second band of the frequency with nearly similar amplitude around $f_{Cl}^* \approx 3.3$, marked with a white dashed rectangular box. Computing the Strouhal number from this frequency returns a value of $St = 0.20$, which is very close to the Strouhal number for Karman vortices as predicted by Eq. 5.1 at the Reynolds number

equivalent to $U^* = 15.9$, which is $\text{Re} = 7.9 \times 10^3$. We thus attribute this second band of frequency as being the footprint left by the shedding of Karman vortices, and the first band as the result of streamwise vortex shedding. Through visual inspection of Fig. 6.5c, both of these dominant frequency bands are markedly wider and the individual values are more scattered from their time-averaged values than any of their counterparts within $U^* \leq 13.6$.

The knowledge that Karman vortices continue to exist and shed from a cruciform structure during SVIV is not new in the literature. However, this is the first time the lift signal from a cruciform structure undergoing SVIV has been subjected to EEMD, revealing the signature of the two dominant vortical structures regulating the flow around the cruciform. Although the amplitude size of the instantaneous frequency band due to Karman vortex is comparable to the streamwise vortex, the reason why the cylinder resists locking into its frequency is perhaps that its frequency too distant from the natural frequency of the system f_n . The shedding frequency of the streamwise vortex is much closer to f_n and is thus preferred by the cylinder.

We consider the transition to SVIV to be complete at $U^* = 18.2$, when the time-averaged phase lag drops further to ≈ 20 deg. Figure 6.6a and 6.6b documents this observation. The instantaneous phase lag is observed to slip through 360 deg. a little past the two second (2 s) time stamp. By inspecting Fig. 6.6a, we found that a little past 2 s is when distortions in the periodicity of C_{Cl,y^*} occur. The slipping through 360 deg. was also observed by Khalak and Williamson (1999) in their work on KVIV, highlighting the quasi-periodic nature of the signal being analysed. There, the slip appeared in Khalak and Williamson (1999) at the initial branch of KVIV. The overall low value of ϕ (≈ 20 deg. for the whole observation time at $U^* = 18.2$), coupled with the presence of ϕ slippage are suggestive of the possibility for $U^* = 18.2$ being the initial branch of SVIV.

6.4 The stable SVIV regime (reduced velocity greater than 20.5)

As U^* is increased to 20.5, we can see a jump in ϕ from a mean value of approximately 20 deg. to about 120 deg., shown in Fig. 6.7a. The phase slippage discussed previously is also observed, indicating the quasi-periodic nature of the lift

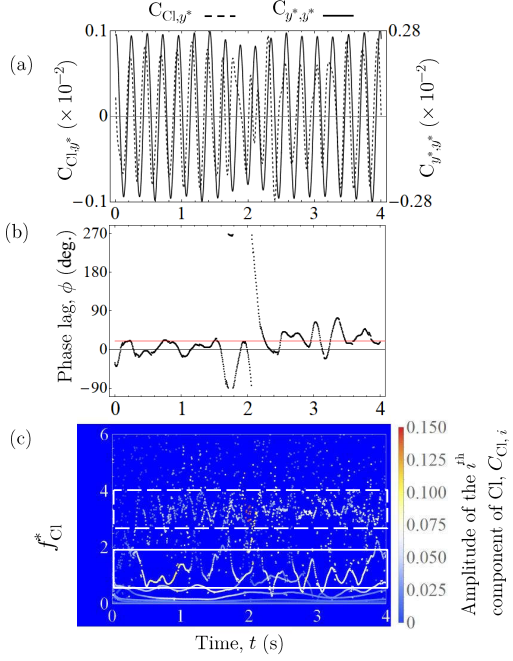


Figure 6.6: Temporal analysis of the lift coefficient and normalised cylinder displacement signal at $U^* = 18.2$. We show C_{Cl,y^*} and C_{y^*,y^*} side by side in Fig. 6.6a, present the temporal evolution of the phase lag ϕ in Fig. 6.6b and show the temporal evolution of the instantaneous frequency of Cl in Fig. 6.6c.

coefficient signal at this U^* . Incidentally, this quasi-periodicity seems to be the norm for the lift signals up to $U^* = 27.3$, as suggested by the phase slippages evident in Figs. 6.7b, c and d. The slippage only stops once U^* reaches 29.5, suggesting a more periodic behaviour of the lift coefficient compared to its counterparts between $20.5 \leq U^* \leq 27.3$. Although the instantaneous phase between $20.5 \leq U^* \leq 27.3$ implies a quasi-periodic nature, their time-averaged values at each U^* are contained in the narrow region $114 < \phi$ (deg.) < 135 , as is the value for ϕ at $U^* = 29.5$. This observation that the time-averaged value of ϕ to only slowly vary with respect to U^* , once U^* increases past 20.5, can be interpreted as the dominant flow structures settling into a stable form that becomes more resilient against external excitations. Based on this feature, we classified $20.5 \leq U^* \leq 29.5$ as the upper branch of SVIV.

The data on the evolution of ϕ allows us to construct a map of the “branches” of vibration modes observed in the range of U^* that we studied. As the branches are mapped against U^* , we need a representative value of ϕ at each U^* . To achieve this, we took the time-averaged values of ϕ , i.e. ϕ_{mean} , and plotted them against U^* in Fig. 6.8. The region A indicates the initial branch of KVIV, where ϕ_{mean} is close to zero.

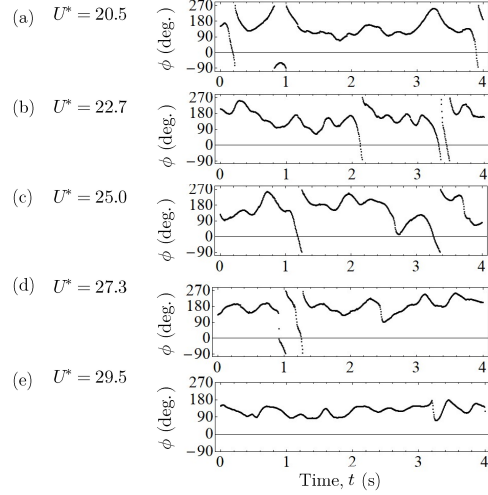


Figure 6.7: The instantaneous phase lag ϕ of C_{Cl,y^*} in the range $20.5 \leq U^* \leq 29.5$. We can observe ϕ slipping through 360 deg. between $20.5 \leq U^* \leq 27.3$, before disappearing at $U^* = 29.5$; an indication of improved stability and resilience of the vortical structure driving the vibration.

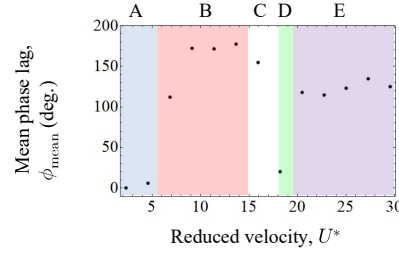


Figure 6.8: Vibration regimes identified during analysis of ϕ . To capture the evolution of ϕ with respect to U^* , a representative value for ϕ at each U^* must be selected. We chose to use the time-averaged ϕ , ϕ_{mean} , as the representative value.

Region B denotes the upper/lower branch of KVIV, where the system experiences a jump from $\phi_{\text{mean}} \approx 0$ to greater than 110 deg. The value of ϕ_{mean} settles very close to 180 deg. towards the end of this upper/lower branch.

Then, ϕ_{mean} experiences a slight drop from about one-sixth the value of ϕ_{mean} in region B, as we enter region C, marking the start of the transition to the SVIV regime. Following this, the system undergoes a more sudden drop to $\phi_{\text{mean}} \approx 20$ deg. at $U^* = 18.2$. This we designate as region D. Finally, in region E, we observe another jump in ϕ_{mean} from $\phi_{\text{mean}} \approx 20$ deg. in region D to approximately 120 deg. when $U^* \geq 20.5$.

CHAPTER 7

ESTIMATION OF HARNESSABLE POWER FROM A PURE CRUCIFORM

7.1 Mathematical model for power estimation

The mathematical model for harnessable power estimation in this study follows that which had been derived in Raghavan *et al.* (2007). In these works, the authors mentioned that work done by the oscillating cylinder $W_{\text{cyl.}}$ during one cycle of oscillation $T_{\text{osc.}}$ is as follows.

$$W_{\text{cyl.}} = \int_0^{T_{\text{osc.}}} (F_L \cdot \dot{y}) dt \quad (7.1)$$

where both the lift F_L and cylinder velocity \dot{y} are both functions of time. Through several manipulations and simplifying assumptions (Sun *et al.*, 2016), the power captured by the system can be written, using our parameters, as the fluid power

$$P_{\text{Fluid,RMS}} = \frac{1}{2} \rho \pi C_{\text{Cl,RMS}} U^2 f_{\text{cyl.}} y_{\text{RMS}}^* D L \sin(\phi), \quad (7.2)$$

or the mechanical power

$$P_{\text{Mech.,RMS}} = 8\pi^3 m_{\text{eff.}} \zeta_{\text{tot.}} (y_{\text{RMS}}^* f_{\text{cyl.}})^2 f_n. \quad (7.3)$$

Here, $P_{\text{Fluid,RMS}}$, $P_{\text{Mech.,RMS}}$, L , $C_{\text{Cl,RMS}}$, $\zeta_{\text{tot.}}$ and $m_{\text{eff.}}$ are the root-mean-square of fluid power, root-mean-square of mechanical power, length of the circular cylinder, characteristic root-mean-square of lift amplitude, total damping coefficient, and the system effective mass respectively. We use C_{Cl,y^*} to represent $C_{\text{Cl,RMS}}$ in Eq. 7.2.

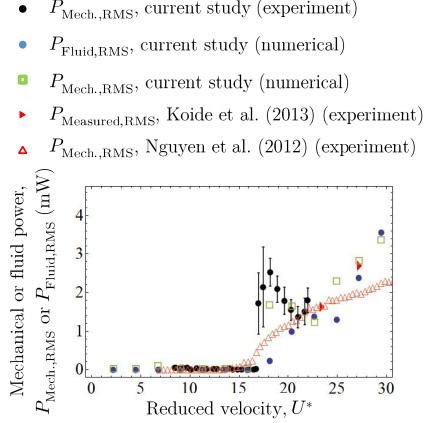


Figure 7.1: Estimated root-mean-square of mechanical power $P_{\text{Mech.,RMS}}$, fluid power $P_{\text{Fluid,RMS}}$, or both, of our experimental and numerical results, compared with results of similar studies in the literature. The fluid power $P_{\text{Fluid,RMS}}$ is calculated only from the results of our numerical study as the others did not measure lift.

We choose to use root-mean-square (parameters with subscript RMS) quantities in Eq. 7.1 instead of the maximum values like the original authors because that may lead to a misunderstanding that the maximum value is sustained throughout the observation window. This obviously is not always the case in our study, especially once the system transits into the SVIV regime. Recall that the time series analysis of $y^*(t)$ and $\text{Cl}(t)$ in Chapter 5 revealed that there is a degree of intermittency in both signals that cannot be overlooked at certain ranges of U^* . Using the root-mean-square value allows us to partially take this into account in the estimation of harnessable power.

Figure 7.1 shows the comparison between power estimated from our experiment and numerical results, with the experimental results of Nguyen *et al.* (2012) and the direct power measurement of Koide *et al.* (2013). Only the value for $P_{\text{Mech.,RMS}}$ is computed from our experimental results due to the absence of lift data. Our numerical results have both lift and cylinder displacement data, and hence, we calculated both $P_{\text{Fluid,RMS}}$ and $P_{\text{Mech.,RMS}}$. We estimated the power from the experimental results of Nguyen *et al.* (2012) by interpolating missing data points in both their amplitude and frequency responses to compute the value of $P_{\text{Mech.,RMS}}$ at a given value of U^* . The direct power measurement by Koide *et al.* (2013) was done by connecting the elastic support of the cylinder to a coil. The coil moves with the cylinder, thus creating a relative piston motion against a fixed magnet and produces an alternating current.

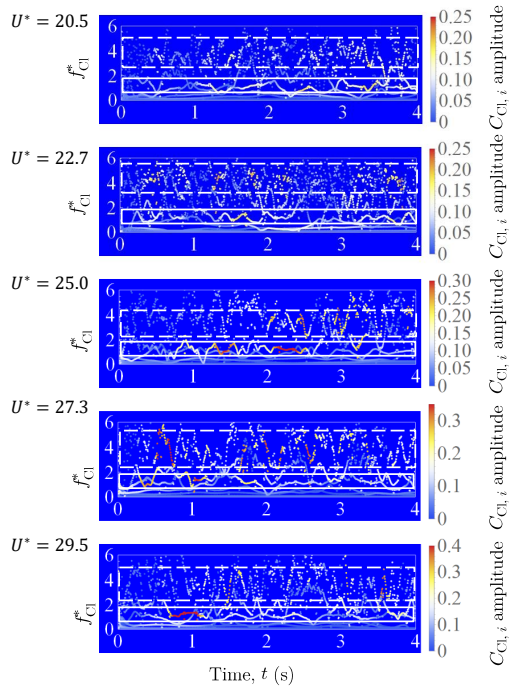


Figure 7.2: The instantaneous frequency of the lift signal between $20.5 \leq U^* \leq 29.5$. The white, solid boxes enclose the IMF component of Cl due to the shedding of the streamwise vortex, while the dashed, white boxes enclose the IMF component due to the shedding of Karman vortex. Through visual inspection, we can see how the degree of dispersion (i.e., height of the box) in the instantaneous frequency of the “Karman component” of lift is about twice that of the “streamwise component” of lift.

The estimated power in the KVIV regime $U^* \leq 15.9$ produces power only in the order of μW , which is relatively insignificant in contrast to the magnitude of power produced in the SVIV regime (mW). In the region $18.2 \leq U^* \leq 22.7$, $P_{\text{Mech,RMS}}$ for our experiment and numerical work exhibits a similar trend where we observed a sudden jump in power output, followed by a gradual decrease. This gradual decrease can be attributed to the increased turbulence level right after the onset of SVIV that imposes a degree of intermittency to the normalised cylinder displacement signal, y^* . For $P_{\text{Fluid,RMS}}$, however, the quantity exhibits a monotonic increase in the range $18.2 \leq U^* \leq 22.7$. We only observe a dip in $P_{\text{Fluid,RMS}}$ at $U^* = 25.0$, suggesting an increase in intermittency of C_{Cl,y^*} at this U^* . In the experimental work of Nguyen *et al.* (2012), $P_{\text{Mech,RMS}}$ only experiences a monotonic increase in the region $18.2 \leq U^* \leq 22.7$. This decidedly different response of the system compared to ours most likely stem from the difference in the actual cruciform used by Nguyen *et al.* (2012). They used two circular cylinders of diameter 10 mm as their cruciform, whereas we used a circular cylinder - strip plate in both our experiments and numerical work. There are no data from the direct power measurement of Koide *et al.* (2013) to compare with within $18.2 \leq U^* \leq 22.7$.

In the range $25.0 \leq U^* \leq 29.5$, we find a reasonably good agreement between the trend found in all data compared: they increase monotonically with respect to U^* . Although the value of our $P_{\text{Fluid,RMS}}$ falls quite notably below the value of $P_{\text{Mech,RMS}}$ at $U^* = 25.0$, other values of $P_{\text{Fluid,RMS}}$, $P_{\text{Mech,RMS}}$ from our numerical results and the direct power measurements by Koide *et al.* (2013) agree well within $27.3 \leq U^* \leq 29.5$. The only set of power data that consistently falls quite a distance below the others is the $P_{\text{Mech,RMS}}$ estimated from the experimental data of Nguyen *et al.* (2012), which again, is most probably due to the difference in the actual geometry of the cruciform used in their investigation.

7.2 Possibility for increasing fluid power

Recall in Fig. 7.1 that although $P_{\text{Fluid,RMS}}$ is computed according to Eq. 7.2, which uses $C_{\text{Cl,RMS}}$ instead of the actual root-mean-square amplitude of lift (Cl_{RMS}), the resulting power estimate does not result in a trend that is totally different from the trend found in the other datasets. Furthermore, except for $P_{\text{Mech,RMS}}$ estimated from

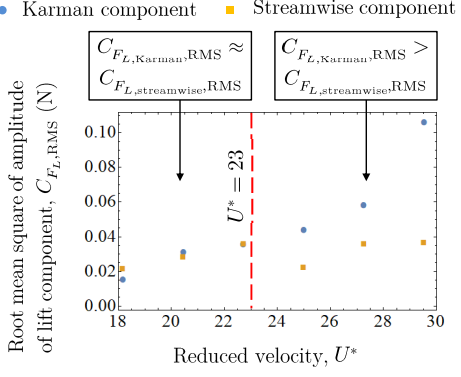


Figure 7.3: Evolution of the root-mean-square amplitude of two dominant lift components due to Karman ($C_{F_L,\text{Karman},\text{RMS}}$) and streamwise ($C_{F_L,\text{streamwise},\text{RMS}}$) vortices with respect to U^* . The region $18.2 \leq U^* \leq 22.7$ exhibits similar magnitude for both the Karman and streamwise components of lift. On the other hand, the magnitude of amplitude for the Karman component while the region $25.0 \leq U^* \leq 29.5$ is almost always twice that of the streamwise component.

the experimental data of Nguyen *et al.* (2012), the values of $P_{\text{Fluid},\text{RMS}}$ are in fairly good agreement with other data that it is compared against at high U^* ($U^* = 27.3$ and 29.5). We see this is an indication that the lift component selected for use in computation of $P_{\text{Fluid},\text{RMS}}$ is an arguably faithful representation of the force driving the motion of the cylinder. This suggests that the motion of the cylinder, once it enters the SVIV regime, is driven only by one component, and not the totality, of the lift force. This component – that has a time-averaged frequency close to the natural frequency of the system, f_n – is the “streamwise component” of lift.

Another significant IMF component of the lift force in the SVIV regime is the component whose mean frequency is close to the Karman frequency of vortex shedding, as explained in §6.3. This Karman component of lift has a similar amplitude size as the streamwise component of lift, as evidenced in Fig. 7.2, and as such is also a dominant component of lift. The Karman components are marked with a dashed, white box, and the streamwise components are marked with a solid, white box, following the convention in Figs. 6.1, 6.2, 6.3, 6.5 and 6.6. However, the Karman component fails to affect the cylinder vibration like the streamwise component most probably due to the large difference between the mean frequency of the Karman component and the natural frequency of the system, f_n . The streamwise component has a mean frequency close to f_n and is hence able to synchronise with the vibration of the cylinder, producing a sizeable amplitude response.

Figure 7.3 shows the root-mean-square amplitude of the Karman and streamwise components of lift in the SVIV regime $U^* \geq 18.2$. Between $18.2 \leq U^* \leq 22.7$, the magnitude of the Karman and streamwise components are nearly equal. However, once we exceed $U^* = 22.7$, Fig. 7.3 shows that the contribution to the root-mean-square amplitude of total lift by the Karman component is on average twice the contribution of the streamwise component. Having such a significant contribution towards the root-mean-square amplitude of total lift implies that there is a significant portion of energy from the free stream being used to energise the Karman vortex structure in the flow. Let us assume a hypothetical situation where we can transfer the contribution by the Karman component to the streamwise component of lift. In other words, consider the situation where we can completely redirect the energy from the Karman to the streamwise vortex. Then, the value for $C_{Cl,RMS}$ in Eq. 7.2 will increase close to a factor of 2 when $18.2 \leq U^* \leq 22.7$, and close to a factor of 3 when $25.0 \leq U^* \leq 29.5$. This increase in $C_{Cl,RMS}$ will lead to the scaling of $P_{Fluid,RMS}$ by the same factor, keeping the other parameters in Eq. 7.2 constant. This exercise demonstrates the room for improvement possible for $P_{Fluid,RMS}$ in future developments of cruciform energy harvesters.

One possible method of improving $P_{Fluid,RMS}$ is by implementing a modified version of the cruciform that is able to enforce the dominance of the vortical structure that is able to lock into f_n - which in Fig. 7.3 is the streamwise vortex - against the vortical structures that do not, i.e., the Karman vortices. We will outline such a method in our future work.

CHAPTER 8

TRANSITION TO KARMAN VORTEX-DRIVEN VIBRATION

8.1 The amplitude and frequency response

As we reduce the cruciform angle to 67.5° and 45° , we find that the SVIV branch observed in the pure cruciform case as $U^* \geq 15.9$ disappear, as one can inspect in Fig. 8.1. For the 45° cruciform, even y_{RMS}^* at the KVIV upper branch ($U^* = 4.5$) is lower than the corresponding values for both the 90° and 67.5° cruciforms.

Another striking departure from the trend observed in the pure cruciform case, can be found in the evolution of f^* in Fig. 8.2. For the 67.5° cruciform in Fig. 8.2a, f^* seems to fluctuate with respect to U^* - suggesting asymmetry in the vortical structures regulating the vibration as discussed previously in §5.1. This fluctuation is however, not as pronounced in Fig. 8.4b, compared to Fig. 8.4a. We think this behaviour is due to the 45° cruciform being less similar to the 90° cruciform, in contrast to 67.5° . In other words, the 45° cruciform is less in transition from the response of the 90° cruciform and the flow around it is more evolved into its new configuration, unlike the 67.5° cruciform.

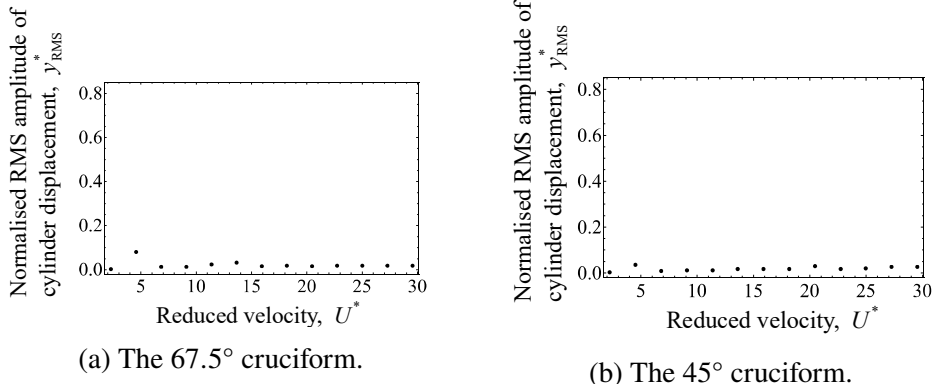


Figure 8.1: Evolution of the normalised root-mean-square amplitude of cylinder displacement y_{RMS}^* , with respect to reduced velocity U^* , for the 67.5° and 45° cruciform.

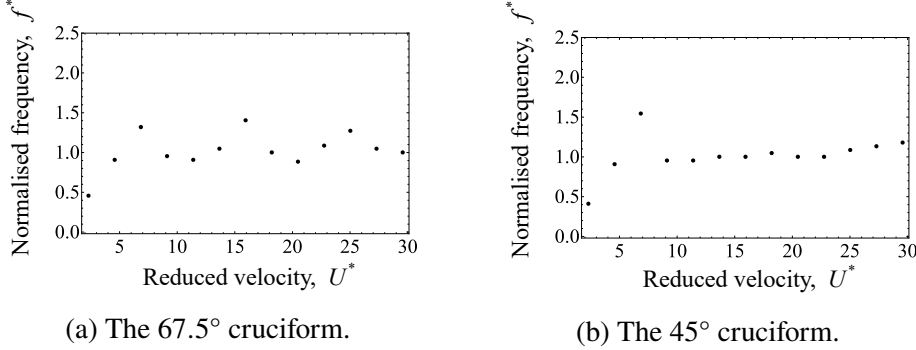


Figure 8.2: Evolution of the normalised cylinder displacement frequency, f^* , with respect to reduced velocity U^* , for the 67.5° and 45° cruciforms.

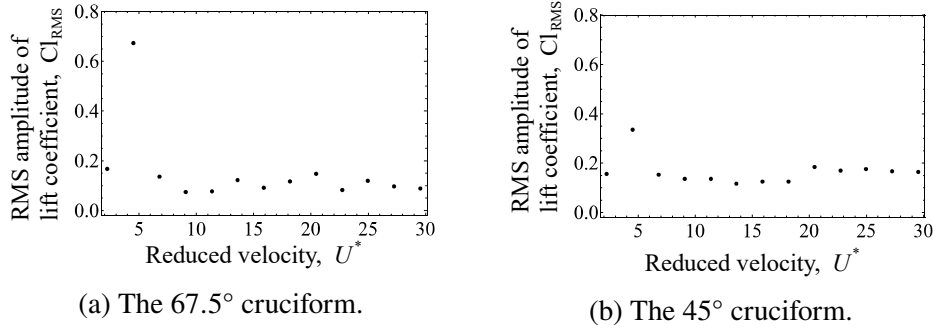


Figure 8.3: Evolution of the normalised Cl root-mean-square amplitude, Cl_{RMS} , with respect to reduced velocity U^* , for the 67.5° and 45° cruciforms.

We summarised the root-mean-square lift coefficients Cl_{RMS} of the 67.5° and 45° cruciforms in Fig. 8.1. Here, we find that their evolution with respect to U^* in Figs. 8.3a and 8.3b approximates their corresponding y_{RMS}^* trend in Figs. 8.1a and 8.1b. As for the variation of f_{Cl}^* with respect to U^* , for both the 67.5° and 45° cruciforms, both exhibit outstanding similarity to $f_{v,Karman}$ of Eq. 5.1. This trait hints that vibrations resulting from the 67.5° and 45° cruciforms are primarily regulated by the shedding of Karman vortices.

The fact that the f_{Cl}^* trends observed in Figs. 8.4a and 8.4b do not lead to similar trends in the evolution of f^* in Figs. 8.2a and 8.2b leads us to believe there is something more fundamental at play in developing the f^* patterns we observed in Figs. 8.2. Hence we examined the vortical structures present in the flow surrounding the 67.5° and 45° cruciforms, and discuss our findings in §8.2.

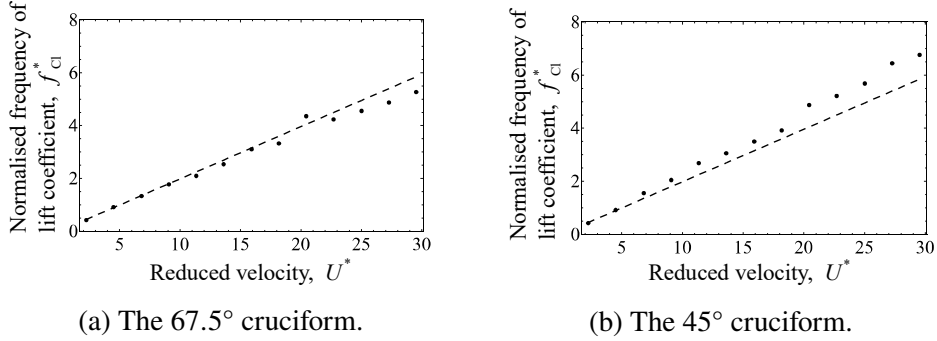


Figure 8.4: Evolution of the normalised Cl lift coefficient frequency, f_{Cl}^* , with respect to reduced velocity U^* , for the 67.5° and 45° cruciforms. The dashed lines outline $f_{v,Karman}$ from Eq. 5.1.

8.2 Main vibration-driving vortical structure

As the first step, we computed the FFT of the y -component of velocity similar to what we did in Fig. 5.5 for both the 67.5° and 45° cruciforms. Our initial assessment of the $f_{v,Karman}^*$ distribution along the cylinder axis in Figs. 8.5a and 8.5b is that there is a strong representation of the Karman shedding frequency in both cases, which at $U^* = 22.7$ is $f_{v,Karman}^* = 4.49$. However, unlike Fig. 5.5, there is no frequency band close to 1 around the cruciform juncture.

Our first guess is that streamwise vortices driving the vibration in the pure cruciform case do not get initiated once the cruciform angle deviates away from 90° . However, x and z -component vorticity visualisations in Fig. 8.6 points out otherwise. These visualisations are produced under the same conditions as Fig. 5.6. Inspecting Figs. 8.6a and 8.6c, we can quite clearly make out the large-scale streamwise vortices close to the cruciform juncture. We thus expect the cylinder vibration and streamwise vortices to synchronise to each other, resulting in an $f^* \approx 1$ across the values of U^* after the lower branch of KVIV which appears at $U^* = 6.8$. In addition, we expect there to be a large amplitude response from the cylinder due to the formation and sustenance of the streamwise vortices close to the cruciform juncture. This was not the case.

We think the reason behind this lies in the distribution of the streamwise vortex cells along the cylinder axis. As we mentioned in §5.2, the streamwise vortex pair in the pure cruciform case lie on a plane parallel to the axis of the cylinder. The shared plane of formation parallel to cylinder axis is what we think as key to the large

amplitude response observed in the pure cruciform case. A formation plane parallel to the cylinder axis ensures the resulting downward thrust to act perpendicular to the cylinder, securing a larger amplitude response. Also, the streamwise vortex cell on each side of the $Z = 0$ plane must be of opposing rotational direction for the production of thrust. We find these two aspects missing in the 67.5° and 45° cruciforms in Fig. 8.6.

What takes place in Figs. 8.6a and 8.6c is, two streamwise vortex cells of opposing poles form on each side of the $Z = 0$ plane. The result of this vortical arrangement is severe diminishing of useful thrust, and by extension, lift acting on the cylinder. This explains why the amplitude of f_v^* at and within the vicinity of 1 is extremely small in comparison to the dominant band close to $f_{v,\text{Karman}}^* = 4.49$, resulting in a low amplitude response for most of the U^* studied, even when $f^* \approx 1$.

We also managed to find the source of asymmetry in the vortical structure distribution around the cruciform, which becomes apparent upon closer comparison of Fig. 8.6b and Fig. 8.6d. The Karman vortices of the 67.5° cruciform are shed at different phases depending on which side of the $Z = 0$ plane we are observing. For the particular case in Fig. 8.6b, Karman vortices are being shed from the top of the cylinder when $Z < 0$, and from the bottom of the cylinder when $Z > 0$. What suggested this interpretation is our observation of a strong expression of $-z$ vorticity when $Z < 0$ from the top of the cylinder, while on the $Z > 0$ half of our domain is a strong expression of $+z$ vorticity from the bottom of the cylinder. We do not see this take place in Fig. 8.6d. On both sides of the $Z = 0$ plane, we note the strong expression of $-z$ vorticity from the top of the cylinder. This asymmetry leads to competing vibration-driving mechanisms resulting in the oscillatory behaviour of f^* seen in Fig. 8.2a.

8.3 Phase lag between Cl and normalised cylinder displacement

Evolution of $\theta_{y-\text{Cl}}$ for the 67.5° and 45° cruciforms share a similar trend in the $2.3 \leq U^* \leq 6.8$ range. For the 67.5° cruciform, past $U^* = 6.8$, there seem to be two distinct VIV branches between $2.3 \leq U^* \leq 13.6$, and between $15.9 \leq U^* \leq 29.5$. In the first branch between $2.3 \leq U^* \leq 13.6$, $\theta_{y-\text{Cl}}$ seems to remain close to 70° , while in the second branch, close to 110° . In some sense, this is fairly similar to the $\theta_{y-\text{Cl}}$ vs.

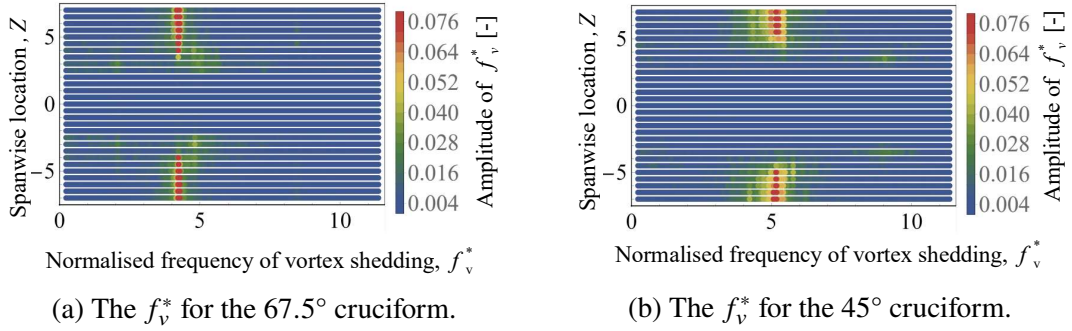


Figure 8.5: Distribution of normalised frequency of vortex shedding, along the span of the cylinder of the 67.5° and 45° cruciforms at $U^* = 22.7$.

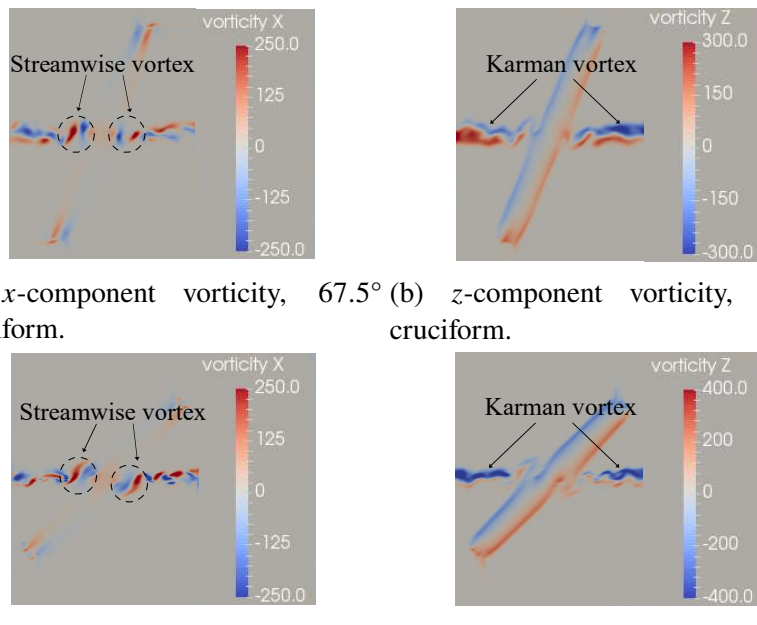
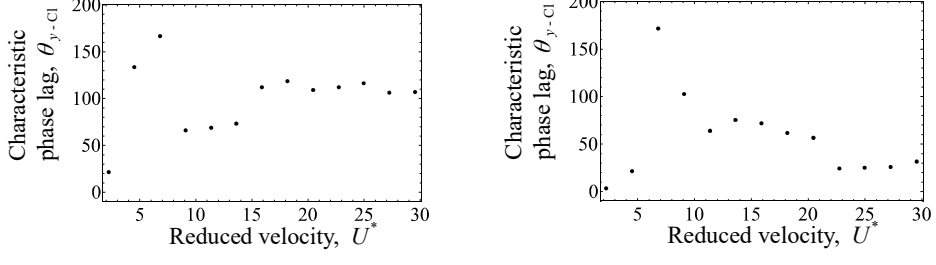


Figure 8.6: Dominant vortical structures at $U^* = 22.7$ observed in the 67.5° and 45° cases. The vorticity slices shown are the x and y -component vorticities (s^{-1}) at the $x/D = 1.96D$ plane, viewed orthogonal to that plane from downstream.



(a) Phase lag for the 67.5° cruciform.

(b) Phase lag for the 45° cruciform.

Figure 8.7: Phase lag $\theta_{y-\text{Cl}}$ ($^\circ$) between Cl and y^* when 67.5° and 45° .

U^* pattern of the pure cruciform case, except for two features. First, the lower branch of KVIV – which in the pure cruciform case exhibits a $\theta_{y-\text{Cl}} \approx 180^\circ$ – does not extend beyond $U^* = 6.8$. Instead, the value for $\theta_{y-\text{Cl}}$ suddenly drops to $\approx 70^\circ$ before jumping back up to $\approx 110^\circ$ starting at $U^* = 15.9$. This value of 110° is curiously close to $\theta_{y-\text{Cl}}$ of the pure cruciform between $20.5 \leq U^* \leq 29.5$, equivalent to the upper branch of SVIV. If we work backwards from $U^* = 20.5$ in the direction of decreasing U^* , and compare Fig. 8.7a and Fig. 5.7, we confront the possibility that the $\theta_{y-\text{Cl}} = 70^\circ$ branch of the 67.5° cruciform is a *variant* of the SVIV initial branch. For the pure cruciform case, this occurs within a narrow window of $15.9 < U^* < 20.5$, with $\theta_{y-\text{Cl}} \approx 20^\circ$.

For the 45° cruciform in Fig. 8.7b, right after lower branch of KVIV at $U^* = 6.8$, $\theta_{y-\text{Cl}}$ transitioned to $\approx 65^\circ$ between $11.4 \leq U^* \leq 20.5$. The proximity between the values 65° and 70° for the 67.5° cruciform suggests the equivalence of the two branches. However, we are inclined to a more cautious conclusion: the two are *variants* of the same branch that is only similar in limited respects as they originate from different angled cruciforms. In this respect, the 45° cruciform is much less similar to the pure cruciform case, as one might expect, simply because 45° is a much larger deviation from 90° compared to 67.5° . This larger deviation is in our opinion what causes $\theta_{y-\text{Cl}}$ in the 45° case to drop further to $\approx 35^\circ$ within $22.7 \leq U^* \leq 29.5$, instead of jumping up to some mean value between $100 \leq \theta_{y-\text{Cl}} (\text{ }^\circ) \leq 130$ similar to what we observe in the 90° and 67.5° cruciforms.

CHAPTER 9

KARMAN VORTEX-DRIVEN VIBRATION

9.1 The amplitude and frequency response

As we decrease the cruciform angle even further to 22.5° , we observe a significant change in the amplitude and frequency response, compared to the transitional stage previously explored in §8. Consider Figs. 9.1a and 9.2a. There is no apparent KVIV upper branch similar to what we have seen in Figs. 8.1a and 8.2a at $U^* = 4.5$. Then, we observe no significant vibration elicited from the oscillator until $U^* = 20.5$. When $U^* = 20.5$, there is a abrupt jump in y_{RMS}^* from $y_{\text{RMS}}^* < 0.02$ to $y_{\text{RMS}}^* \approx 0.3$. The f^* vs. U^* trend demonstrated a bypassing of the KVIV lower branch - which occurred at $U^* = 6.8$ in the transitional stages of §8 - right into $f^* \approx 1$. Past $U^* = 20.5$, the value for y_{RMS}^* continues to increase and saturates at $U^* = 25.0$, and f^* continues to be close to 1 up to $U^* = 29.5$.

The 0° cruciform (Figs. 9.1b, 9.2b) in essence exhibits a very similar trend in its y_{RMS}^* and f^* evolutions with respect to U^* . However, the jump – which for the 22.5° cruciform occurs at $U^* = 20.5$ – occurs at a much lower $U^* = 9.1$. Then, y_{RMS}^* continues to grow until $U^* = 20.5$, reaching a staggering $y_{\text{RMS}}^* \approx 0.8$, a value no other study on energy harvesting using cruciform oscillators has ever achieved. The value of y_{RMS}^* then saturates close to 0.8 up to $U^* = 29.5$. Also similar to the 22.5° cruciform, f^* falls close to 1 at same U^* the y_{RMS}^* jump occurs - hinting at synchronisation between vortex shedding and system natural frequency.

Apart from the amplitude/frequency response of the 22.5° cruciform, the evolution of C_{RMS} against U^* showcases a similar trend to the evolution y_{RMS}^* , as shown in Fig. 9.3a. The corresponding f_{Cl}^* in Fig. 9.4a demonstrates the dominant frequency of Cl taking after Eq. 5.1 between $2.3 \leq U^* \leq 18.2$, before abruptly dropping close to 1 between $20.5 \leq U^* \leq 29.5$. This in part informs us that the flow

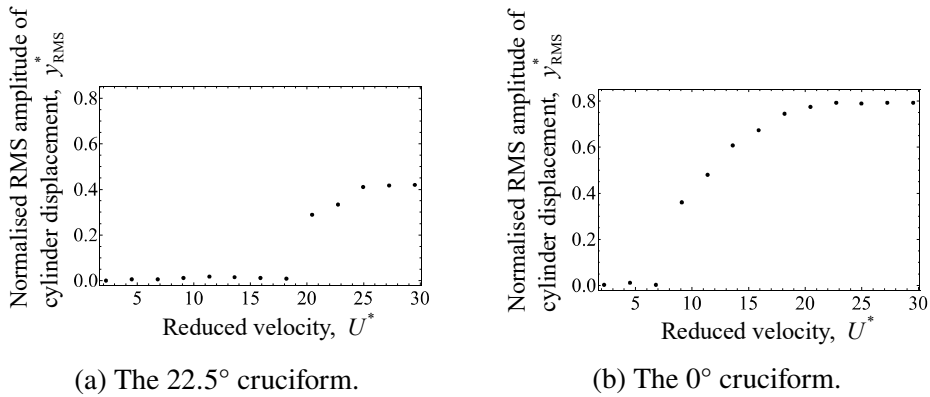


Figure 9.1: Evolution of the normalised root-mean-square amplitude of cylinder displacement y_{RMS}^* , with respect to reduced velocity U^* , for the 22.5° and 0° cruciform.

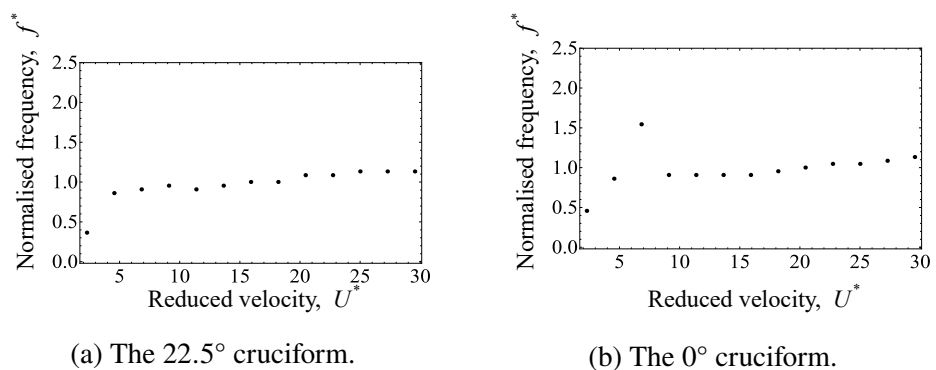


Figure 9.2: Evolution of the normalised cylinder displacement frequency, f^* , with respect to reduced velocity U^* , for the 22.5° and 0° cruciforms.

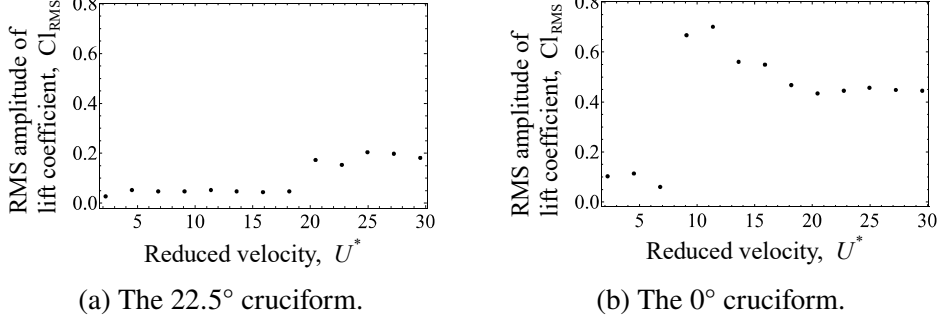


Figure 9.3: Evolution of the normalised Cl root-mean-square amplitude, Cl_{RMS} , with respect to reduced velocity U^* , for the 22.5° and 0° cruciforms.

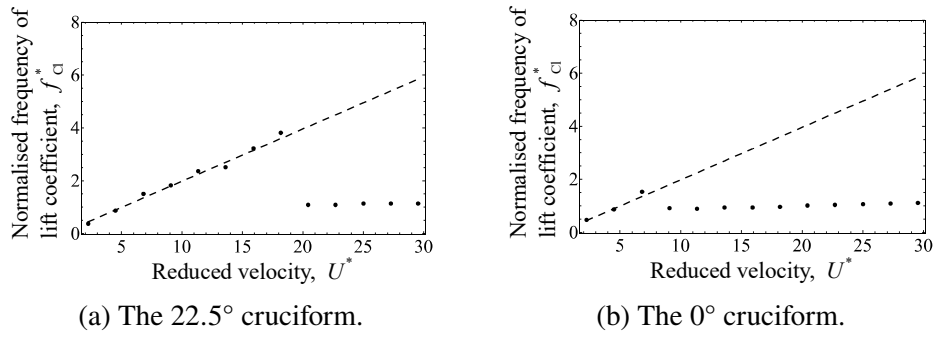


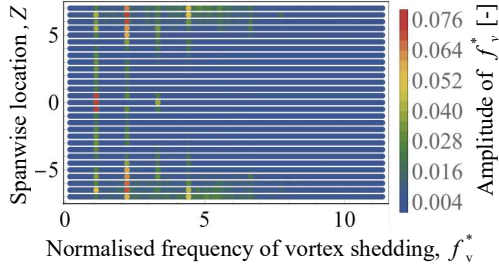
Figure 9.4: Evolution of the normalised Cl frequency, f_{Cl}^* , with respect to reduced velocity U^* , for the 22.5° and 0° cruciforms. The dashed lines outline $f_{v,Karman}$ from Eq. 5.1.

between $2.3 \leq U^* \leq 18.2$ is governed by flow physics that are similar to both 67.5° and 45° within the same U^* range.

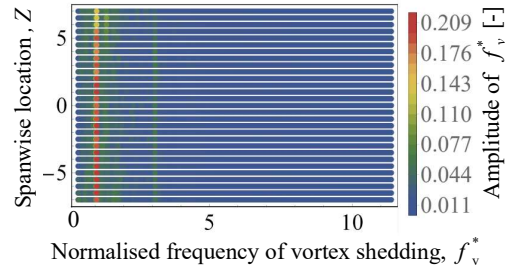
For the 0° cruciform, we see that the jump in Cl_{RMS} occurs at the same U^* as the jump in the corresponding y_{RMS}^* i.e., $U^* = 9.1$. After $U^* = 9.1$, the magnitude of Cl_{RMS} gradually drops to a final value of $Cl_{RMS} \approx 0.45$ at $U^* = 20.5$, and remains there up to $U^* = 29.5$. Similar to the 22.5° cruciform, f_{Cl}^* grows linearly in accordance with, again, Eq. 5.1 until the jump in both Cl_{RMS} and y_{RMS}^* , where f_{Cl}^* drops close to 1 for the rest the U^* we examine in this study.

9.2 Main vibration-driving vortical structure

To understand the cause behind the marked difference between the amplitude/frequency response in both 67.5° and 45° cruciforms, we proceed to deduce the type of vortical structures that form in the flows around the 22.5° and 0° cruciform.



(a) The f_v^* for the 22.5° cruciform.



(b) The f_v^* for the 0° cruciform.

Figure 9.5: Distribution of normalised frequency of vortex shedding, along the span of the cylinder of the 22.5° and 0° cruciforms at $U^* = 22.7$.

We first produce the visualise of f_v^* along the cylinder, in the same manner as Figs. 5.5 and 8.5, in Fig. 9.5a. Inspecting Fig. 9.5a, we immediately notice that several frequency bands exist: $f_v^* \approx 1, 2, 3, 4.5$, the most visible of which is the $f_v^* \approx 1$ band. However, unlike the pure cruciform case in Fig. 5.5 – where the dominant frequency bands are localised to certain regions along the cylinder – the $f_v^* \approx 1$ band of the 22.5° cruciform seems to encompass the length of the cylinder. This also seems to be the case for the 0° cruciform, displaying a dominant f_v^* band at approximately 1 along the length of the cylinder.

We then queried the x and z -component vorticity contours of the 22.5° cruciform for deeper insight, presented in Figs. 9.6a and 9.6b. In doing so, we found that the large scale streamwise vortex pair near the cruciform juncture is absent. Instead, we noticed streamwise vortex cells distributed on both sides of the $Z = 0$ plane, except within the immediate neighbourhood of the cruciform juncture. We note that these streamwise vortex cells are distributed at a slight angle relative to the z -axis, seemingly following the angle of the strip plate, i.e. 22.5° . Visualisation of the z -component vorticity in Fig. 9.6b intimates the nature of the tilted streamwise vortex cells: they are simply three-dimensional Karman vortex structures, akin to those observed in the experiments of Williamson (1996), especially mode B. We inferred this from comparison of the same visual region delimited by dashed rectangles in Figs. 9.6a and 9.6b, showing the overlap between the streamwise vortex cells and the strong Karman vortex component.

For the 0° cruciform in Figs. 9.6c and 9.6d, this overlap between the streamwise vortex cells and the distinct Karman vortex component is even more

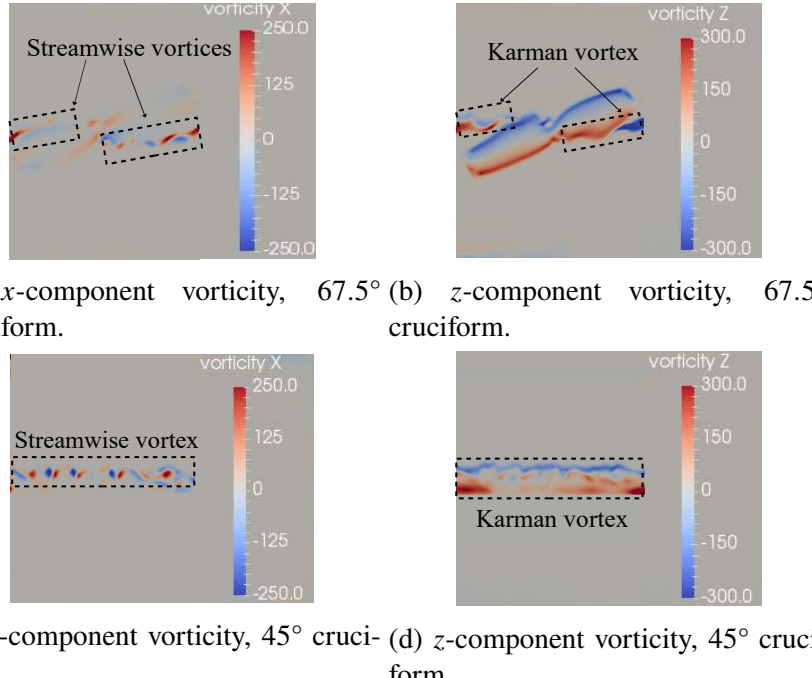


Figure 9.6: Dominant vortical structures at $U^* = 22.7$ observed in the 22.5° and 0° cases. The vorticity slices shown are the x and y -component vorticities (s^{-1}) at the $x/D = 1.96D$ plane, viewed orthogonal to that plane from downstream.

visually pronounced. We interpret this as further evidence to the hypothesis that three-dimensional Karman vortical structures govern the vibration of the cylinder for shallow angled cruciforms, including the 0° cruciform, which perhaps is more aptly named in-tandem configuration. Notice that for the 0° layout, both the streamwise vortex cells and the Karman vortical structure are arranged parallel to the z -axis, or at 0° relative to the cylinder. This observation seems to demonstrate the role of the strip plate in shallow angled cruciforms: it modifies the spatial distribution of the Karman vortical structure that is driving the vibration of the cylinder.

As we have seen in §5 and 8, eliciting a significant vibration amplitude Karman vortex shedding is limited to a narrow U^* range containing the upper branch of KVIV. Beyond that, Karman vortex shedding fails to lock into the natural frequency of the system to produce meaningful vibrations. The fact that shallow angled cruciforms in this §9.2 are able to produce very large vibration amplitudes intimate the crucial role played by the strip plate in forcing the shedding of vortical structures and cylinder vibration to lock into the natural frequency of the system f_n . We think the mechanics of this forced lock-in is as follows.

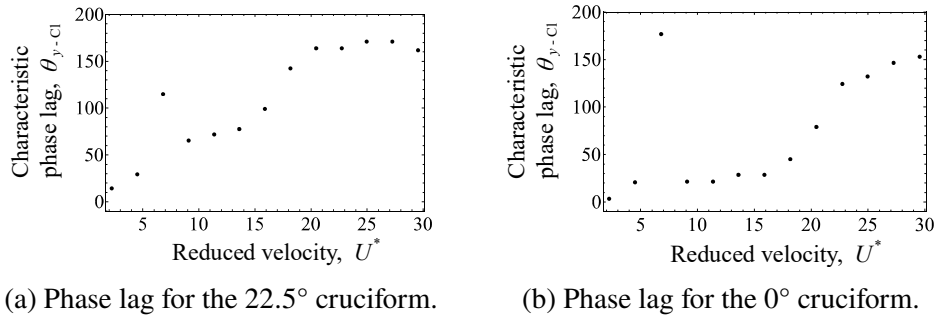
1. Shallow angled cruciforms have a larger overlap area between the cylinder and strip plate. This permits a more perceptible interaction among vortices shed from the cylinder and the strip plate.
2. Upon exceeding a critical U^* , vortical structures shed from both the cylinder and the strip plate becomes sufficiently energised, and they start to behave as one.
3. This vortical synchronisation locks into the natural frequency of the elastic structure in its immediate vicinity - our circular cylinder.

The results also suggest the total cylinder-strip plate area overlap as a factor influencing the exact U^* at which the vortical synchronisation occurs. The U^* at which the synchronisation – and the jump to large y_{RMS}^* amplitude – occurs at a lower value when the overlap area is bigger. Nevertheless, there seems to be a limit to this lowering of U^* , which in this work we determined to be $U^* = 9.1$. Recall that this is the value where the synchronisation begins for the 0° layout; the layout where the totality of the cylinder and strip plate projections onto the $y - z$ plane coincides with each other.

9.3 Phase lag between Cl and normalised cylinder displacement

In Fig. 9.7a, we summarise the evolution of $\theta_{y-\text{Cl}}$ with respect to U^* for the 22.5° cruciform and find $\theta_{y-\text{Cl}} \approx 115^\circ$ at $U^* = 29.5$. The significance of $U^* = 29.5$ for the 22.5° cruciform is that it is where a jump in $\theta_{y-\text{Cl}}$ occurs from $\approx 30^\circ$ to $\approx 115^\circ$. This abrupt jump usually demarcates transition to the KVIV lower branch, as stated in the discussion accompanying Figs. 5.7 and 8.7, with a value that is very close to 180° . The $\theta_{y-\text{Cl}}$ for the 22.5° cruciform however, is about 36% smaller than the expected $\approx 180^\circ$. This may be the cause of absence of the KVIV lower branch in the f^* vs. U^* plot of the 22.5° cruciform (Fig. 9.2a).

The 0° arrangement produces a similar trend to Fig. 9.7a, as one can see in Fig. 9.7b. However, the $\theta_{y-\text{Cl}}$ jump at $U^* = 29.5$ is more pronounced and achieves a value very close to 180° . Following the sudden jump is the sudden drop at $U^* = 9.1$, which brings $\theta_{y-\text{Cl}}$ to approximately 25° . This trend continues up to $U^* = 15.9$, after which we find $\theta_{y-\text{Cl}}$ to monotonically increase up to $U^* = 29.5$.



(a) Phase lag for the 22.5° cruciform.

(b) Phase lag for the 0° cruciform.

Figure 9.7: Phase lag $\theta_{y\text{-Cl}}$ ($^\circ$) between Cl and y^* when 22.5° and 0° .

CHAPTER 10

POWER CHARACTERISTIC IN CRUCIFORM ANGLE - REDUCED VELOCITY PARAMETER SPACE

In this study, we estimate the mechanical power harnessed from the flow for each cruciform through the application of the formula in Eq. 7.3.

To understand how mechanical power $P_{\text{Mech.,RMS}}$ is influenced not only by U^* , but also by the strip plate tilt angle α ($^\circ$), we decided to visualise $P_{\text{Mech.,RMS}}$ as contour plots, where the abscissa and ordinate are U^* and α , respectively, and the colour of the contours denote the magnitude of $P_{\text{Mech.,RMS}}$. As an example, we plotted the values of y_{RMS}^* against U^* and α in Fig. 10.1. The data used to produce Fig. 10.1 are those from Figs. 5.1, 8.1 and 9.1. We then performed linear interpolations on the y_{RMS}^* data along both U^* and α axes to populate the $\alpha-U^*$ parameter space. The result of this two-dimensional interpolation is Fig. 10.1. The snapshot of y_{RMS}^* evolution in the $\alpha-U^*$ parameter space summarises our observations made previously in Figs. 5.1, 8.1 and 9.1.

We then perform the same two-dimensional interpolation on our $P_{\text{Mech.,RMS}}$ results and summarised them in Fig. 10.2. Two regions of significant power generation exist: first, in the $18.2 \leq U^* \leq 29.5$ range as α approaches 90° , and second, starting as low as $U^* = 9.1$ up to $U^* = 29.5$ as α approaches 0° . The estimated power in the region approaching $\alpha = 90^\circ$ agrees well in magnitude with previous experimental works such as Koide *et al.* (2013). Also, even though no power data was measured in pure cruciform oscillator studies of Koide *et al.* (2009); Nguyen *et al.* (2012), their y_{RMS}^* data agrees well in trend and in magnitude with Fig. 10.1, along the 90° line. The $P_{\text{Mech.,RMS}}$ contour of Fig. 10.2 visualises the high power region as α approaches 0° and U^* approaches 29.5. The highest $P_{\text{Mech.,RMS}}$ estimated from our simulation reaches $O(10^1)$ mW, which is one order of magnitude larger than any cruciform energy harvester of this scale have ever recorded in the literature.

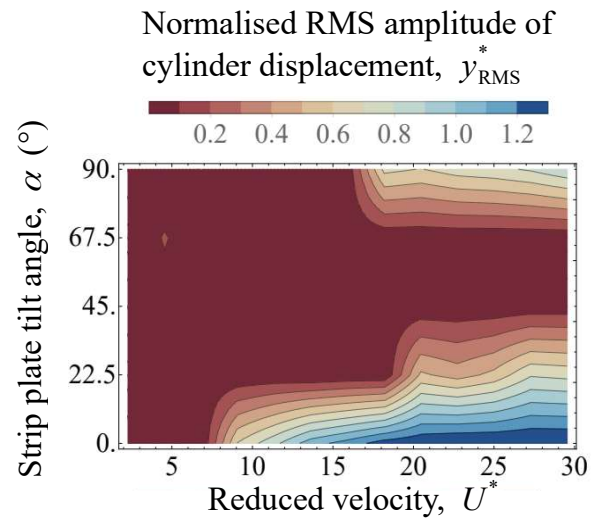


Figure 10.1: Isocontours describing the map of the normalised RMS amplitude of cylinder displacement, y_{RMS}^* in the cruciform angle - reduced velocity ($\alpha-U^*$) parameter space.

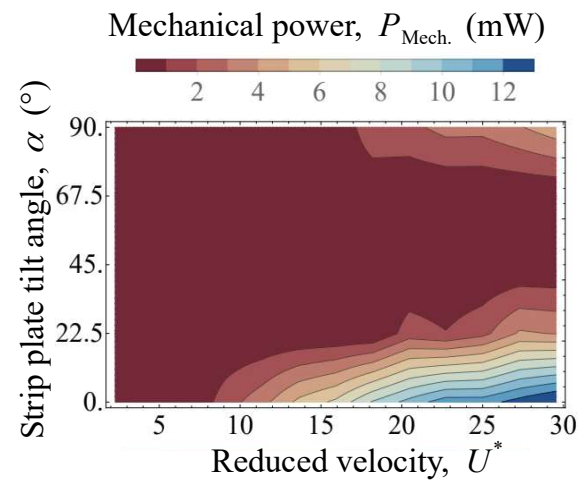


Figure 10.2: Isocontours describing the map of the estimated mechanical power in the cruciform angle - reduced velocity ($\alpha-U^*$) parameter space.

The $P_{\text{Mech.,RMS}}$ contour also elucidated the feasibility of cruciform angle variation as a means to control the range of U^* within which substantive quantity of power can be harnessed. For a given operating range of U^* , one can choose for substantive power generation to take place in the high U^* region ($U^* \geq 18.2$), or across a larger range starting from a minimum of $U^* = 9.1$, by manipulating the cruciform angle. For power generation in the high U^* region, one simply sets the cruciform angle to 90° , and for power generation starting from the lowest possible U^* , one should opt for a shallow-angled cruciform, with increasing magnitude of power generated as $\alpha \rightarrow 0^\circ$.

Our estimation of mechanical power efficiency $\eta_{\text{Mech.}} (\%)$ is based on the definition of efficiency in Sun *et al.* (2018). Our version of $\eta_{\text{Mech.}}$ is shown in Eq. 10.1.

$$\eta_{\text{Mech.}} (\%) = \frac{P_{\text{Mech.,RMS}}}{P_{\text{Fluid}}} = \frac{1}{2} \rho U_\infty^3 (2y_{\text{RMS}} + D) L \quad (10.1)$$

Here, U_∞ and L are the freestream velocity of the flow and the length of the cylinder, respectively. Our variant of efficiency uses y_{RMS} instead of $y_{\text{Max.}}$ like Sun *et al.* (2018), due to our focus on time-averaged quantities instead of possibly one-off values.

Unlike Fig. 10.2, the efficiency contour does not display a trend similar to the contour of y_{RMS}^* in Fig. 10.1. The pure cruciform achieves maximum $\eta_{\text{Mech.}}$ close to $U^* = 18.2$, steep-angled cruciforms (67.5° and 45° cruciforms) attain maximum $\eta_{\text{Mech.}}$ within the vicinity of $(U^*, \alpha) = (4.5, 67.5^\circ)$, and shallow-angled cruciforms (22.5° and 0° layouts) strikes maximum $\eta_{\text{Mech.}}$ in the neighbourhood of $(U^*, \alpha) = (9.1, 0^\circ)$. These high-efficiency regions is consistent with our assertion that different flow dynamics govern the vibration resulting from either the pure, steep-angled or shallow-angled cruciforms.

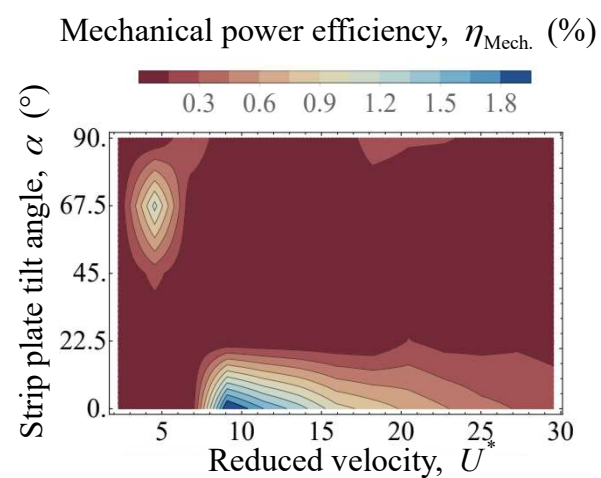


Figure 10.3: Isocontours describing the map of the estimated mechanical power in the cruciform angle - reduced velocity ($\alpha-U^*$) parameter space.

CHAPTER 11

CONCLUSION

In this study, we numerically investigated the temporal evolution of the lift coefficient and cylinder displacement signals of an elastically supported cruciform system in the range $1.1 \times 10^3 < \text{Re} < 14.6 \times 10^3$, or $2.3 < U^* < 29.5$. Our circular cylinder diameter is 10 mm and the natural frequency of the system is 4.4 Hz. Validation of key numerical results was made experimentally in a custom-built open flow channel, using a cruciform system whose parameters were tuned as close as possible to the quantities used in the numerical study. Decomposing the lift coefficient signal in the SVIV regime ($15.9 \leq U^* \leq 29.5$) using EEMD allows us to see that the complexity of the lift coefficient signal as being caused by the superpositioning of two dominant components of lift. One due to the shedding of Karman and the other due to the shedding of streamwise vortices. The former has a frequency close to the vortex shedding frequency of Karman vortex from a smooth, isolated circular cylinder, while the latter has a mean frequency close to f_n . Application of the Hilbert-Huang transform on the dominant component of cylinder displacement – and the component of lift most correlated to it – allows for the computation of the instantaneous phase lag between lift and cylinder displacement. The time-averaged phase lag revealed five “branches” of vibration, among which is the initial branch of SVIV at $U^* = 18.2$, which has never been identified before in the literature. We also computed the instantaneous frequency of the lift coefficient, thus revealing the loss of periodicity and self-similarity in the lift coefficient signal as the system enters the SVIV regime. Estimation of power from our results show that the root-mean-square mechanical and fluid power computed from our experimental and numerical work agree to varying degrees depending on U^* with data from similar studies in the literature. Finally, we estimated that the root-mean-square fluid power can potentially be increased close to a factor of 2 within $18.2 \leq U^* \leq 22.7$ and close to a factor of 3 when $25.0 \leq U^* \leq 29.5$. We base this estimation on the premise of redirecting the contribution to the root-mean-square amplitude of total lift from Karman vortex shedding, towards the streamwise component of lift alone.

In this study, we numerically investigated the temporal evolution of the lift coefficient and cylinder displacement signals of an elastically supported cruciform system in the range $1.1 \times 10^3 < \text{Re} < 14.6 \times 10^3$, or $2.3 < U^* < 29.5$, for cruciform angles $\alpha = 90^\circ, 67.5^\circ, 45^\circ, 22.5^\circ$ and 0° . We chose the 90° cruciform as the representative case to validate our numerical setup through a GCI study and comparison with experimental measurements in a custom-built closed loop open flow channel. After successful validation of the 90° cruciform, we impose the same conditions on all cruciforms studied, which includes mesh resolution, boundary conditions and solver settings. Here are the main conclusions from this work.

- (a) The large amplitude vibrations of the pure cruciform (90°) are governed by streamwise vortex pairs that are localised within the vicinity of the cruciform juncture when $U^* \geq 18.2$, producing power in the order of $O(10^0)$ mW. The highest efficiency is attained in the neighbourhood of $U^* = 18.2$.
- (b) The small amplitude vibrations of the steep-angled cruciforms (67.5° and 45°) are due to asymmetrical distribution of vortical structures relative to the $Z = 0$ plane, producing sub-mW power. The highest efficiency is attained in the neighbourhood of $(U^*, \alpha) = (4.5, 67.5^\circ)$.
- (c) The large amplitude vibrations of the shallow-angled cruciforms (22.5° and 0°) are due to the shedding of three-dimensional Karman vortices resulting from synchronisation of vortices shed from the cylinder and the strip plate, which end up locking into the natural frequency of the cylinder. The power produced by these cruciforms can reach an order of $O(10^1)$ mW. The highest efficiency is attained in the neighbourhood of $(U^*, \alpha) = (9.1, 0^\circ)$.

In the future, we will consider improving the resolution of the contour plots by investigating smaller increments of the cruciform angle to shed light on the sensitivity of each vibration-driving mechanism with respect to the cruciform layout.

REFERENCES

- Arul, M., Kareem, A. and Kwon, D. K. (2020). Identification of Vortex-Induced Vibration of Tall Building Pinnacle Using Cluster Analysis for Fatigue Evaluation: Application to Burj Khalifa. *Journal of Structural Engineering*. ISSN 0733-9445. doi:10.1061/(asce)st.1943-541x.0002799.
- Barrero-Gil, A., Alonso, G. and Sanz-Andres, A. (2010). Energy harvesting from transverse galloping. *Journal of Sound and Vibration*. 329(14), 2873–2883. ISSN 0022460X. doi:10.1016/j.jsv.2010.01.028. Retrievable at <http://www.sciencedirect.com/science/article/pii/S0022460X10000891> <http://dx.doi.org/10.1016/j.jsv.2010.01.028>.
- Bearman, P. (2011). Circular cylinder wakes and vortex-induced vibrations. *Journal of Fluids and Structures*. 27(5-6), 648–658. ISSN 08899746. doi:10.1016/j.jfluidstructs.2011.03.021. Retrievable at <http://www.sciencedirect.com/science/article/pii/S0889974611000600>.
- Bernitsas, M. and Raghavan, K. (2008). Reduction/suppression of VIV of circular cylinders through roughness distribution at $8 \times 10^3 < Re < 1.5 \times 10^5$. In *Proceedings of the International Conference on Offshore Mechanics and Arctic Engineering - OMAE*, vol. 5.
- Bernitsas, M. M., Ben-Simon, Y., Raghavan, K. and Garcia, E. M. H. (2009). The VIVACE Converter: Model Tests at High Damping and Reynolds Number Around 10^5 . *Journal of Offshore Mechanics and Arctic Engineering*. 131(1). ISSN 08927219. doi:10.1115/1.2979796. Retrievable at <http://offshoremechanics.asmedigitalcollection.asme.org/article.aspx?articleid=1472649>.
- Bernitsas, M. M., Raghavan, K., Ben-Simon, Y. and Garcia, E. M. H. (2008). VIVACE (Vortex Induced Vibration Aquatic Clean Energy): A New Concept in Generation of Clean and Renewable Energy From Fluid Flow. *Journal of Offshore Mechanics and Arctic Engineering*. 130(4), 041101. ISSN 08927219. doi:10.1115/1.2957913. Retrievable at <http://www.scopus.com/record/display.url?eid=2-s2.0-56749179917&origin=resultslist&sort=plf-f&src=s&st1=A+new+concept+in+generation+of+clean+and+renewable+>

energy+from+fluid+flow{&}sid=620865A71FAF26768C42655E1E8BC194.
aXczxbyuHHiXgaIW6Ho7g:230{&}sot=b{&}sdt=b{&}h.

Blevins, R. D. (1990). Flow-induced vibration.

Bukka, S. R., Magee, A. R. and Jaiman, R. K. (2020). Stability analysis of passive suppression for vortex-induced vibration. *Journal of Fluid Mechanics*. ISSN 14697645. doi:10.1017/jfm.2019.1026.

Chen, Z. Q., Liu, M., Hua, X. and Mou, T. (2012). Flutter, Galloping, and Vortex-Induced Vibrations of H-Section Hangers. *Journal of Bridge Engineering*. 17(3), 500–508. ISSN 10840702. doi:10.1061/(ASCE)BE.1943-5592.0000268.

Deng, J., Ren, A.-L. and Shao, X.-M. (2007). The flow between a stationary cylinder and a downstream elastic cylinder in cruciform arrangement. *Journal of Fluids and Structures*. 23(5), 715–731. ISSN 0889-9746. doi:10.1016/J.JFLUIDSTRUCTS.2006.11.005. Retrievable at <https://www.sciencedirect.com/science/article/pii/S0889974606001472>.

Department of Irrigation and Drainage Malaysia (2016). *Pelan Strategik Jabatan Pengairan dan Saliran Malaysia 2016-2020*. Retrievable at <http://water.selangor.gov.my/index.php/en/maklumat-jabatan/fungsi-jabatan/pengurusan-pantai/2-uncategorised/243-strategi-dan-formulasi-tindakan-pelan-strategik-jps-2016-2020>.

Derakhshandeh, J. F., Arjomandi, M., Dally, B. and Cazzolato, B. (2014). The effect of arrangement of two circular cylinders on the maximum efficiency of Vortex-Induced Vibration power using a Scale-Adaptive Simulation model. *Journal of Fluids and Structures*. 49, 654–666. doi:10.1016/j.jfluidstructs.2014.06.005. Retrievable at <https://www.scopus.com/inward/record.uri?eid=2-s2.0-84905271504&doi=10.1016%2Fj.jfluidstructs.2014.06.005&partnerID=40&md5=2e075f7a296ab8a6f4d1e1d23bbcc05b>.

Desai, A., Mittal, S. and Mittal, S. (2020). Experimental investigation of vortex shedding past a circular cylinder in the high subcritical regime. *Physics of Fluids*. 32(1), 014105. ISSN 10897666. doi:10.1063/1.5124168. Retrievable at <http://aip.scitation.org/doi/10.1063/1.5124168>.

- Ding, L., Zhang, L., Kim, E. S. and Bernitsas, M. M. (2015a). URANS vs. experiments of flow induced motions of multiple circular cylinders with passive turbulence control. *Journal of Fluids and Structures*. 54, 612–628. ISSN 10958622. doi: 10.1016/j.jfluidstructs.2015.01.003.
- Ding, L., Zhang, L., Wu, C., Mao, X. and Jiang, D. (2015b). Flow induced motion and energy harvesting of bluff bodies with different cross sections. *Energy Conversion and Management*. ISSN 01968904. doi:10.1016/j.enconman.2014.12.039.
- Ding, W., Sun, H., Xu, W. and Bernitsas, M. M. (2017). Two tandem cylinders with turbulence stimulation in FIV power conversion: CFD with experimental verification of interaction. In *Proceedings of the International Conference on Offshore Mechanics and Arctic Engineering - OMAE*, vol. 10. doi:10.1115/OMAE2017-62271. Retrievable at <https://www.scopus.com/inward/record.uri?eid=2-s2.0-85032024173&doi=10.1115%2FOMAE2017-62271&partnerID=40&md5=409ba703a93beb879e4a1a62be1909f8>.
- Ding, W., Sun, H., Xu, W. and Bernitsas, M. M. (2019). Numerical investigation on interactive FIO of two-tandem cylinders for hydrokinetic energy harnessing. *Ocean Engineering*. 187, 106215. doi:10.1016/J.OCEANENG.2019.106215. Retrievable at <https://www.sciencedirect.com/science/article/pii/S0029801819304019>.
- Doare, O. and Michelin, S. (2011). Piezoelectric coupling in energy-harvesting fluttering flexible plates: Linear stability analysis and conversion efficiency. *Journal of Fluids and Structures*. 27(8), 1357–1375. ISSN 08899746. doi: 10.1016/j.jfluidstructs.2011.04.008.
- Duranay, A. and Kinaci, O. K. (2020). Enhancing two-dimensional computational approach for vortex-induced vibrations by scaling lift force. *Ocean Engineering*. 217, 107620. ISSN 00298018. doi:10.1016/j.oceaneng.2020.107620.
- Durhasan, T., Pinar, E., Ozkan, G., Akilli, H. and Sahin, B. (2019). The effect of shroud on vortex shedding mechanism of cylinder. *Applied Ocean Research*. 84, 51–61. ISSN 01411187. doi:10.1016/j.apor.2019.01.007. Retrievable at <https://linkinghub.elsevier.com/retrieve/pii/S0141118718305467>.
- Feng, C. C. (1963). The measurement of vortex idunced effects in flow past stationary and oscillating circular and D-section cylinders. (October), 100.

- Gao, G., Zhu, L., Li, J. and Han, W. (2020). Application of a new empirical model of nonlinear self-excited force to torsional vortex-induced vibration and nonlinear flutter of bluff bridge sections. *Journal of Wind Engineering and Industrial Aerodynamics*. ISSN 01676105. doi:10.1016/j.jweia.2020.104313.
- Garcia, E. M. and Bernitsas, M. M. (2018). Effect of damping on variable added mass and lift of circular cylinders in vortex-induced vibrations. *Journal of Fluids and Structures*. 80, 451–472. ISSN 0889-9746. doi:10.1016/J.JFLUIDSTRUCTS.2018.02.005. Retrievable at <https://www.sciencedirect.com/science/article/pii/S0889974616304546>.
- Gazis, A. and Katsiri, E. (2020). A wireless sensor network for underground passages: Remote sensing and wildlife monitoring. *Engineering Reports*. 2(6). ISSN 2577-8196. doi:10.1002/eng2.12170. Retrievable at <https://onlinelibrary.wiley.com/doi/abs/10.1002/eng2.12170>.
- Gómez-Ortega, O., Manzanares-Bercial, R., Ogueta-Gutiérrez, M., Lopez-Nuñez, E., Franchini, S., Roibás-Millán, E. and Sanz-Andres, A. (2019). Experiments on the transverse aeroelastic instability of a single sphere in a swing configuration under a longitudinal wind. *Journal of Wind Engineering and Industrial Aerodynamics*. ISSN 01676105. doi:10.1016/j.jweia.2019.103979.
- Gumelar, A. B., Purnomo, M. H., Yuniarno, E. M. and Sugiarto, I. (2019). Spectral Analysis of Familiar Human Voice Based On Hilbert-Huang Transform. In *2018 International Conference on Computer Engineering, Network and Intelligent Multimedia, CENIM 2018 - Proceeding*. doi:10.1109/CENIM.2018.8710943.
- Hao, W. and Yang, Q. (2020). Reformative translation model for probability density functions of amplitude processes of crosswind-excited super-tall buildings. *Advances in Structural Engineering*. ISSN 20484011. doi:10.1177/1369433219886086.
- Hemsuwan, W., Sakamoto, K., Nakada, S. and Takahashi, T. (2018a). A longitudinal vortex wind turbine: Numerical study. *Journal of Wind Engineering and Industrial Aerodynamics*. 180, 213–230. ISSN 0167-6105. doi:10.1016/J.JWEIA.2018.07.022. Retrievable at <https://www.sciencedirect.com/science/article/pii/S0167610518301612>.
- Hemsuwan, W., Sakamoto, K., Nakada, S. and Takahashi, T. (2018b). A longitudinal vortex wind turbine: Numerical study. *Journal of Wind Engineering and Industrial*

Aerodynamics. 180, 213–230. ISSN 0167-6105. doi:10.1016/J.JWEIA.2018.07.022. Retrievable at <https://www.sciencedirect.com/science/article/pii/S0167610518301612>.

Hemsuwan, W., Sakamoto, K. and Takahashi, T. (2018c). Lift Force Generation of a Moving Circular Cylinder with a Strip-Plate Set Downstream in Cruciform Arrangement: Flow Field Improving Using Tip Ends. *International Journal of Aeronautical and Space Sciences.* 19(3), 606–617. ISSN 2093-274X. doi:10.1007/s42405-018-0068-5. Retrievable at <http://link.springer.com/10.1007/s42405-018-0068-5>.

Hemsuwan, W., Sakamoto, K. and Takahashi, T. (2018d). Numerical investigation of lift-force generation on a moving circular cylinder in a uniform flow driven by longitudinal vortex. *Journal of Fluids and Structures.* 83, 448–470. ISSN 0889-9746. doi:10.1016/J.JFLUIDSTRUCTS.2018.09.010. Retrievable at <https://www.sciencedirect.com/science/article/pii/S0889974617308885>.

Hu, G. and Kwok, K. C. (2020). Predicting wind pressures around circular cylinders using machine learning techniques. *Journal of Wind Engineering and Industrial Aerodynamics.* 198, 104099. ISSN 01676105. doi:10.1016/j.jweia.2020.104099.

Huang, N. E. (2014). *Hilbert-Huang transform and its applications.* vol. 16. World Scientific.

Huang, N. E. and Attoh-Okine, N. O. (2005). *The Hilbert-Huang transform in engineering.* CRC Press.

Huang, N. E., Shen, Z., Long, S. R., Wu, M. C., Snin, H. H., Zheng, Q., Yen, N. C., Tung, C. C. and Liu, H. H. (1998). The empirical mode decomposition and the Hilbert spectrum for nonlinear and non-stationary time series analysis. *Proceedings of the Royal Society A: Mathematical, Physical and Engineering Sciences.* ISSN 13645021. doi:10.1098/rspa.1998.0193.

Kadir, E. A., Rosa, S. L. and Yulianti, A. (2019). Application of WSNs for Detection Land and Forest Fire in Riau Province Indonesia. In *Proceedings of 2018 International Conference on Electrical Engineering and Computer Science, ICECOS 2018.* ISBN 9781538657201. doi:10.1109/ICECOS.2018.8605197.

Kawabata, Y., Takahashi, T., Haginoya, T. and Shirakashi, M. (2013). Interference Effect of Downstream Strip-Plate on the Crossflow Vibration of a Square Cylinder. *Journal of Fluid Science and Technology*. 8(3), 647–658. ISSN 1880-5558. doi: 10.1299/jfst.8.348.

Kementerian Kewangan Malaysia (2019). *Belanjawan 2020*. Retrievable at <http://www.kabinet.gov.my/bkpp/pdf/belanjawan/2020.pdf>.

Khalak, A. and Williamson, C. (1999). Motions, Forces And Mode Transitions In Vortex-Induced Vibrations At Low Mass-Damping. *Journal of Fluids and Structures*. 13(7-8), 813–851. ISSN 08899746. doi:10.1006/jfls.1999.0236. Retrievable at <http://www.sciencedirect.com/science/article/pii/S0889974699902360>.

Kinaci, O. K., Lakka, S., Sun, H. and Bernitsas, M. M. (2016). Effect of tip-flow on vortex induced vibration of circular cylinders for Re. *Ocean Engineering*. 117, 130–142. ISSN 00298018. doi:10.1016/j.oceaneng.2016.03.055. Retrievable at <http://www.sciencedirect.com/science/article/pii/S002980181630018X>.

Kluger, J., Moon, F. and Rand, R. (2013). Shape optimization of a blunt body Vibro-wind galloping oscillator. *Journal of Fluids and Structures*. 40, 185–200. ISSN 08899746. doi:10.1016/j.jfluidstructs.2013.03.014. Retrievable at <http://www.sciencedirect.com/science/article/pii/S0889974613000868>.

Koide, M., Kato, N., Yamada, S., Kawabata, Y., Takahashi, T. and Shirakashi, M. (2007). Influence Of A Cruciform Arrangement Downstream Strip-Plate On Crossflow Vibration. *Journal of Computational and Applied Mechanics*. 8(2), 135–148.

Koide, M., Ootani, K., Yamada, S., Takahashi, T. and Shirakashi, M. (2006). Vortex Excitation Caused by Longitudinal Vortices Shedding from Cruciform Cylinder System in Water Flow. *JSME International Journal*. 49(4), 1043–1048.

Koide, M., Sekizaki, T., Yamada, S., Takahashi, T. and Shirakashi, M. (2009). A Novel Technique for Hydroelectricity Utilizing Vortex Induced Vibration. In *Proceedings of the ASME Pressure Vessels and Piping Division Conference, PVP2009-77487*.

Koide, M., Sekizaki, T., Yamada, S., Takahashi, T. and Shirakashi, M. (2013). Prospect of Micro Power Generation Utilizing VIV in Small Stream Based on Verification

- Experiments of Power Generation in Water Tunnel. *Journal of Fluid Science and Technology*. 8(3), 294–308. ISSN 1880-5558. doi:10.1299/jfst.8.294.
- Koide, M., Takahashi, T., Shirakashi, M. and Salim, S. A. Z. B. S. (2017). Three-dimensional structure of longitudinal vortices shedding from cruciform two-cylinder systems with different geometries. *Journal of Visualization*, 1–11.
- Krishnendu, P. and Ramakrishnan, B. (2020). Performance analysis of dual sphere wave energy converter integrated with a chambered breakwater system. *Applied Ocean Research*. 101, 102279. ISSN 01411187. doi:10.1016/j.apor.2020.102279.
- Langley Research Centre (2018). *Turbulence Modeling Resource*. Retrievable at <https://turbmodels.larc.nasa.gov/>.
- Larsen, C. M. and Halse, K. H. (1997). Comparison of models for vortex induced vibrations of slender marine structures. *Marine Structures*. 10(6), 413–441. ISSN 09518339. doi:10.1016/S0951-8339(97)00011-7. Retrievable at <http://www.sciencedirect.com/science/article/pii/S0951833997000117>.
- Lee, J. H. and Bernitsas, M. M. (2011). High-damping, high-Reynolds VIV tests for energy harnessing using the VIVACE converter. *Ocean Engineering*. ISSN 00298018. doi:10.1016/j.oceaneng.2011.06.007.
- Lee, J. H., Xiros, N. and Bernitsas, M. M. (2011). Virtual damperspring system for VIV experiments and hydrokinetic energy conversion. *Ocean Engineering*. ISSN 00298018. doi:10.1016/j.oceaneng.2010.12.014.
- Liu, G., Li, H., Qiu, Z., Leng, D., Li, Z. and Li, W. (2020). *A mini review of recent progress on vortex-induced vibrations of marine risers*. doi:10.1016/j.oceaneng.2019.106704.
- Luo, S., Chew, Y. and Ng, Y. (2003). Hysteresis phenomenon in the galloping oscillation of a square cylinder. *Journal of Fluids and Structures*. 18(1), 103–118. ISSN 08899746. doi:10.1016/S0889-9746(03)00084-7. Retrievable at <http://www.sciencedirect.com/science/article/pii/S0889974603000847>.
- Ma, C., Sun, H., Nowakowski, G., Mauer, E. and Bernitsas, M. M. (2016). Nonlinear piecewise restoring force in hydrokinetic power conversion using flow induced motions of single cylinder. *Ocean Engineering*. ISSN 00298018. doi:10.1016/j.oceaneng.2016.10.020.

- Mao, Y. C., Cheng, Y. K. and Qi, H. (2020). Sensor Network Partition Based on the Spatial-Temporal Features for Structure Safety Monitoring. *Jisuanji Xuebao/Chinese Journal of Computers*. ISSN 02544164. doi:10.11897/SP.J.1016.2020.00631.
- Maruai, N. M., Ali, M. S. M., Ismail, M. H. and Zaki, S. A. (2018). Flow-induced vibration of a square cylinder and downstream flat plate associated with micro-scale energy harvester. *Journal of Wind Engineering and Industrial Aerodynamics*. 175, 264–282. doi:10.1016/j.jweia.2018.01.010. Retrievable at <https://www.scopus.com/inward/record.uri?eid=2-s2.0-85042219159&doi=10.1016%2Fj.jweia.2018.01.010&partnerID=40&md5=2f3f62b94bb69ced3368b32e682aefc7>.
- Maruai, N. M., Mat Ali, M. S., Ismail, M. H. and Shaikh Salim, S. A. Z. (2017). Downstream flat plate as the flow-induced vibration enhancer for energy harvesting. *Journal of Vibration and Control*, 107754631770787. ISSN 1077-5463. doi:10.1177/1077546317707877. Retrievable at <http://journals.sagepub.com/doi/10.1177/1077546317707877>.
- Mat Ali, M. S., Doolan, C. J. and Wheatley, V. (2011). Low Reynolds number flow over a square cylinder with a splitter plate. *Physics of Fluids*. 23(3). ISSN 10706631. doi:10.1063/1.3563619.
- Mat Ali, M. S., Doolan, C. J. and Wheatley, V. (2012). Low Reynolds number flow over a square cylinder with a detached flat plate. *International Journal of Heat and Fluid Flow*. 36, 133–141. ISSN 0142727X. doi:10.1016/j.ijheatfluidflow.2012.03.011. Retrievable at <http://dx.doi.org/10.1016/j.ijheatfluidflow.2012.03.011>.
- Meng, S., Chen, Y. and Che, C. (2020). Slug flow's intermittent feature affects VIV responses of flexible marine risers. *Ocean Engineering*. ISSN 00298018. doi:10.1016/j.oceaneng.2019.106883.
- Nakamura, T., Kaneko, S., Fumio, I., Minoru, K., Kunihiko, I., Nishihara, T., Mureithi, N. W. and Mikael A., L. (2013). *Flow-Induced Vibrations: Classifications and Lessons from Practical Experiences*. Butterworth-Heinemann. ISBN 0080983529. Retrievable at <https://books.google.com/books?hl=en&lr=&id=LQusIJlDbswC&pgis=1>.

- Nakamura, Y. and Nakashima, M. (1986). Vortex excitation of prisms with elongated rectangular, H and |- cross-sections. *Journal of Fluid Mechanics*. ISSN 14697645. doi:10.1017/S0022112086002252.
- Nguyen, T., Koide, M., Yamada, S., Takahashi, T. and Shirakashi, M. (2012). Influence of mass and damping ratios on VIVs of a cylinder with a downstream counterpart in cruciform arrangement. *Journal of Fluids and Structures*. 28, 40–55. ISSN 08899746. doi:10.1016/j.jfluidstructs.2011.10.006.
- Ni, F. T., Zhang, J. and Noori, M. N. (2020). Deep learning for data anomaly detection and data compression of a long-span suspension bridge. *Computer-Aided Civil and Infrastructure Engineering*. ISSN 14678667. doi:10.1111/mice.12528.
- Ogink, R. and Metrikine, A. (2010). A wake oscillator with frequency dependent coupling for the modeling of vortex-induced vibration. *Journal of Sound and Vibration*. 329(26), 5452–5473. ISSN 0022460X. doi:10.1016/j.jsv.2010.07.008. Retrievable at <http://www.sciencedirect.com/science/article/pii/S0022460X10004621>.
- Pathak, A. (2020). An artificial bee colony inspired clustering solution to prolong lifetime of wireless sensor networks. *Iranian Journal of Electrical and Electronic Engineering*. ISSN 23833890. doi:10.22068/IJEEE.16.4.425.
- Raghavan, K. (2007). *Energy Extraction from a Steady Flow Using Vortex Induced Vibration*. Doctoral dissertation. The University of Michigan. Retrievable at <http://deepblue.lib.umich.edu/handle/2027.42/55687>.
- Raghavan, U., Albert, R. and Kumara, S. (2007). Near linear time algorithm to detect community structures in large-scale networks. *Phys. Rev E*. 76, 036106.
- Raissi, M., Wang, Z., Triantafyllou, M. S. and Karniadakis, G. E. (2019). Deep learning of vortex-induced vibrations. *Journal of Fluid Mechanics*. 861, 119–137. ISSN 14697645. doi:10.1017/jfm.2018.872. Retrievable at <https://core.ac.uk/core/journals/journal-of-fluid-mechanics/article/deep-learning-of-vortexinduced-vibrations/B7D9B152C42B7F1E895C1661F5A85881>.
- Ren, F., Wang, C. and Tang, H. (2019). Active control of vortex-induced vibration of a circular cylinder using machine learning. *Physics of Fluids*. 31(9), 093601. ISSN

10897666. doi:10.1063/1.5115258. Retrievable at <http://aip.scitation.org/doi/10.1063/1.5115258>.

Richardson, L. F. and Gaunt, J. A. (1927). The deferred approach to the limit. *Philosophical Transactions of the Royal Society A*. ISSN 1364-5021. doi: <https://doi.org/10.1098/rsta.1927.0008>.

Sadeghi Eshkevari, S., Pakzad, S. N., Takáč, M. and Matarazzo, T. J. (2020). Modal Identification of Bridges Using Mobile Sensors with Sparse Vibration Data. *Journal of Engineering Mechanics*. ISSN 0733-9399. doi:10.1061/(asce)em.1943-7889.0001733.

Shiraishi, N., Matsumoto, M., Shirato, H. and Ishizaki, H. (1988). On aerodynamic stability effects for bluff rectangular cylinders by their corner-cut. *Journal of Wind Engineering and Industrial Aerodynamics*. 28(1-3), 371–380. ISSN 01676105. doi: 10.1016/0167-6105(88)90133-X. Retrievable at <http://www.sciencedirect.com/science/article/pii/016761058890133X>.

Shirakashi, M., Mizuguchi, K. and Bae, H. M. (1989). Flow-induced excitation of an elastically-supported cylinder caused by another located downstream in cruciform arrangement. *Journal of Fluids and Structures*. 3(6), 595–607. ISSN 10958622. doi:10.1016/S0889-9746(89)90150-3.

Spalart, P. and Allmaras, S. (1992). A one-equation turbulence model for aerodynamic flows. In *30th Aerospace Sciences Meeting and Exhibit*. ISBN 0034-1223. ISSN 00341223. doi:10.2514/6.1992-439. Retrievable at <http://arc.aiaa.org/doi/10.2514/6.1992-439>.

Stern, F., Wilson, R. V., Coleman, H. W. and Paterson, E. G. (2001). Comprehensive approach to verification and validation of CFD simulations part 1: methodology and procedures. *Journal of fluids engineering*. 123(4), 793–802.

Sun, H., Kim, E. S., Nowakowski, G., Mauer, E. and Bernitsas, M. M. (2016). Effect of mass-ratio, damping, and stiffness on optimal hydrokinetic energy conversion of a single, rough cylinder in flow induced motions. *Renewable Energy*. 99, 936–959. ISSN 09601481. doi:10.1016/j.renene.2016.07.024. Retrievable at <http://www.sciencedirect.com/science/article/pii/S0960148116306206>.

- Sun, H., Ma, C. and Bernitsas, M. M. (2018). Hydrokinetic power conversion using Flow Induced Vibrations with nonlinear (adaptive piecewise-linear) springs. *Energy*. 143, 1085–1106. ISSN 03605442. doi:10.1016/j.energy.2017.10.140. Retrievable at <https://linkinghub.elsevier.com/retrieve/pii/S0360544217318455>.
- Sun, H., Ma, C., Kim, E. S., Nowakowski, G., Mauer, E. and Bernitsas, M. M. (2019). Flow-induced vibration of tandem circular cylinders with selective roughness: Effect of spacing, damping and stiffness. *European Journal of Mechanics, B/Fluids*. 74, 219–241. ISSN 09977546. doi:10.1016/j.euromechflu.2018.10.024.
- Unit Pemodenan Tadbiran dan Perancangan Pengurusan Malaysia (2016). *Pelan Strategik ICT Sektor Awam 2016-2020*. Retrievable at <https://www.mampu.gov.my/ms/penerbitan-mampu/send/2-buku/680-pelan-strategik-ict-sektor-awam-2016-2020-versi-bm-2>.
- Wang, S., Wen, F., Shi, X. and Zhou, X. (2019). Stability analysis of asymmetric wakes. *Physics of Fluids*. ISSN 10897666. doi:10.1063/1.5098111.
- Wen, C., Wang, J., Zhang, Y., Xu, T., Zhang, X. and Ning, Y. (2020). Vehicle Trajectory Clustering and Anomaly Detection at Freeway Off-Ramp Based on Driving Behavior Similarity. In *CICTP 2020*. Aug. Reston, VA: American Society of Civil Engineers. ISBN 9780784482933, 4220–4232. doi:10.1061/9780784482933.362. Retrievable at <http://ascelibrary.org/doi/10.1061/9780784482933.362>.
- Williamson, C. H. K. (1996). Three-dimensional wake transition. *Journal of Fluid Mechanics*. 328(-1), 345. ISSN 0022-1120. doi:10.1017/S0022112096008750.
- Wu, W., Bernitsas, M. M. and Maki, K. (2011). RANS Simulation vs. Experiments of Flow Induced Motion of Circular Cylinder With Passive Turbulence Control at $35,000 < \text{Re} < 130,000$. In *Volume 7: CFD and VIV; Offshore Geotechnics*. Jan. ASME. ISBN 978-0-7918-4439-7, 733–744. doi:10.1115/OMAE2011-50311. Retrievable at <http://proceedings.asmedigitalcollection.asme.org/proceeding.aspx?articleid=1625495>.
- Wu, W., Sun, H., Lv, B. and Bernitsas, M. M. (2018). Modelling of a hydrokinetic energy converter for flow-induced vibration based on experimental data. *Ocean Engineering*. 155, 392–410. doi:10.1016/j.oceaneng.2018.02.030. Retrievable at <https://www.scopus.com/inward/record.uri?eid=2-s2.0-85043200000&partnerID=MNR&md5=3f3a2a2a2a2a2a2a2a2a2a2a2a2a2a2a>

2-s2.0-85042874481{&}doi=10.1016%2Fj.oceaneng.2018.02.

030{&}partnerID=40{&}md5=7bd22494378724dd2a876aa95e327a1c.

Wu, Z. and Huang, N. E. (2008). Ensemble Empirical Mode Decomposition: A Noise-Assisted Data Analysis Method. *Advances in Adaptive Data Analysis*. ISSN 1793-5369. doi:10.1142/s1793536909000047.

Xia, Y., Michelin, S. and Doaré, O. (2015a). Fluid-solid-electric lock-in of energy-harvesting piezoelectric flags. *Physical Review Applied*. 3(1), 14009. ISSN 23317019. doi:10.1103/PhysRevApplied.3.014009.

Xia, Y., Michelin, S. S., Doaré, O. and Doare, O. (2015b). Resonance-induced enhancement of the energy harvesting performance of piezoelectric flags. *Applied Physics Letters*. 107(26), 1–5. ISSN 00036951. doi:10.1063/1.4939117.

Xu, W., Ji, C., Sun, H., Ding, W. and Bernitsas, M. M. (2017). Flow-induced vibration (FIV) and hydrokinetic power conversion of two staggered, low mass-ratio cylinders, with passive turbulence control in the TrSL3 flow regime ($2.5 \times 10^4 < Re < 1.2 \times 10^5$). In *Proceedings of the International Conference on Offshore Mechanics and Arctic Engineering - OMAE*, vol. 10. doi:10.1115/OMAE2017-62693. Retrievable at <https://www.scopus.com/inward/record.uri?eid=2-s2.0-85032014937&doi=10.1115%2FOMAE2017-62693&partnerID=40&md5=53697e5a091f39f503803929f1b46bf5>.

Xu, W., Ji, C., Sun, H., Ding, W. and Bernitsas, M. M. (2019). Flow-induced vibration of two elastically mounted tandem cylinders in cross-flow at subcritical Reynolds numbers. *Ocean Engineering*. 173, 375–387. ISSN 0029-8018. doi:10.1016/J.OCEANENG.2019.01.016. Retrievable at <https://www.sciencedirect.com/science/article/pii/S0029801819300174>.

Yokoi, Y. (2016). Flow visualization of the vortex shedding from an in-line oscillating circular cylinder with splitter plate. In *AIP Conference Proceedings*, vol. 1745. Jun. American Institute of Physics Inc. ISBN 9780735414020. ISSN 15517616, 020066. doi:10.1063/1.4953760. Retrievable at <http://aip.scitation.org/doi/abs/10.1063/1.4953760>.

Zdravkovich, M. (1981). Review and classification of various aerodynamic and hydrodynamic means for suppressing vortex shedding. *Journal of Wind Engineering and Industrial Aerodynamics*. 7(2), 145–189. ISSN 01676105. doi:10.

1016/0167-6105(81)90036-2. Retrievable at <http://www.sciencedirect.com/science/article/pii/0167610581900362>.

Zdravkovich, M. (1985). Flow induced oscillations of two interfering circular cylinders. *Journal of Sound and Vibration.* 101(4), 511–521. ISSN 0022-460X. doi: 10.1016/S0022-460X(85)80068-7. Retrievable at <http://www.sciencedirect.com/science/article/pii/S0022460X85800687>.

Zdravkovich, M. M. (1983). Interference between two circular cylinders forming a cross. *Journal of Fluid Mechanics.* 128(-1), 231. ISSN 0022-1120. doi:10.1017/S0022112083000464.

Zdravkovich, M. M. (1997). *Flow around circular cylinders.* ISBN 0198563965. Retrievable at <http://www.scopus.com/inward/record.url?eid=2-s2.0-0030744960&partnerID=tZ0tx3y1>.

Zellweger, F., Coomes, D., Lenoir, J., Depauw, L., Maes, S. L., Wulf, M., Kirby, K. J., Brunet, J., Kopecký, M., Máliš, F., Schmidt, W., Heinrichs, S., den Ouden, J., Jaroszewicz, B., Buyse, G., Spicher, F., Verheyen, K. and De Frenne, P. (2019). Seasonal drivers of understorey temperature buffering in temperate deciduous forests across Europe. *Global Ecology and Biogeography.* ISSN 14668238. doi:10.1111/geb.12991.

Zhang, B., Mao, Z., Song, B., Ding, W. and Tian, W. (2018a). Numerical investigation on effect of damping-ratio and mass-ratio on energy harnessing of a square cylinder in FIM. *Energy.* 144, 218–231. doi:10.1016/j.energy.2017.11.153. Retrievable at <https://www.scopus.com/inward/record.uri?eid=2-s2.0-85037995662&doi=10.1016%2Fj.energy.2017.11.153&partnerID=40&md5=01db7c6b6d4d44e88de7045843c7d423>.

Zhang, D., Sun, H., Wang, W. and Bernitsas, M. M. (2018b). Rigid cylinder with asymmetric roughness in Flow Induced Vibrations. *Ocean Engineering.* 150, 363–376. ISSN 00298018. doi:10.1016/j.oceaneng.2018.01.005. Retrievable at <https://linkinghub.elsevier.com/retrieve/pii/S0029801818300052>.

Zhang, J., Guo, H., Tang, Y. and Li, Y. (2020). Effect of top tension on vortex-induced vibration of deep-sea risers. *Journal of Marine Science and Engineering.* ISSN 20771312. doi:10.3390/jmse8020121.

- Zhao, M. and Lu, L. (2018). Numerical simulation of flow past two circular cylinders in cruciform arrangement. *Journal of Fluid Mechanics*. 848, 1013–1039. ISSN 0022-1120. doi:10.1017/jfm.2018.380. Retrievable at <https://www.cambridge.org/core/product/identifier/S0022112018003804/type/journal{ }article>.
- Zhou, L., Meng, Y. and Abbaspour, K. C. (2019). A new framework for multi-site stochastic rainfall generator based on empirical orthogonal function analysis and Hilbert-Huang transform. *Journal of Hydrology*. ISSN 00221694. doi:10.1016/j.jhydrol.2019.05.047.

LIST OF PUBLICATIONS

Journal with Impact Factor

- (a) Paper 1
- (b) Paper 2

Indexed Journal (SCOPUS)

- (a) Paper 3

Non-Indexed Journal

- (a) Paper 4

Indexed conference proceedings

- (a) Paper 5

Non-Indexed conference proceedings

- (a) Paper 6